Development of a Frictional Mechanical Metamaterial for Repeatable Energy Dissipation

A Thesis Submitted to Auckland University of Technology (AUT) in Fulfilment of the Requirements for the degree of

Doctor of Philosophy

by **Eunhyeuk (Joshua) Jeong**

Department of Mechanical Engineering
School of Engineering, Computer and Mathematical Sciences
Auckland University of Technology (AUT) New Zealand

September 2025

Attestation of Authorship

I hereby declare that this submission is my own work and that, to the best of my knowledge and belief, it contains no material previously published or written by another person nor material which to a substantial extent has been accepted for the qualification of any other degree or diploma of a university or other institution of higher learning.

_____

Eunhyeuk Jeong

September 2025

Acknowledgement

At the first onset, I would like to express sincere gratitude to my supervisors, Professor Maziar Ramezani and Professor Emilio Calius for their devoted guidance, instruction, patience and continuous encouragement during my journey into the PhD study at Auckland University of Technology (AUT). Whenever I ran into an obstacle, their dedication was the driving force behind me to continue the race without giving up until the end. Their devoted teaching has made the biggest difference in my life, and I know that their contribution will serve me well in the rest of my life, and I wish them all the best.

A big thanks to Mr. Mark Masterton, as a technician staff at the Engineering Workshop of AUT, who help me not only perform compression and tensile experiments but also provide technical support.

I would also like to take this opportunity to thank my fellow students – Anthony, Tingzhen, and Ravisrini – who encouraged each other in times of difficulty. I would like to wish Anthony, who graduated first, all the best for his future journey, and I would also like to thank Tingzhen and Ravisrini, who are in the final stages of their studies, and I am sure that they will soon come to fruition.

Special thanks to Ana and Maria, who have been like aunts to me. Their touching kindness will always remain with me for the rest of my life, as they were always concerned about my health and academic progress, encouraging me and praying for me whenever I was struggling with my studies.

I would also like to thank Angel and Leo, who encouraged me in the early days of my PhD studies, even though we are no longer in contact. Hopefully, one day we will meet again and share the joy of having safely completed a long academic journey.

Massive gratitude to my family members – Gloria, Elliott, and Esther – for always being there for me through many difficult times, giving me unflinching love in every way possible although we may be physically apart and distant. You all have made my journey of pursuing academic expertise possible through many prayers and support. And father, who is resting in heaven, I hope you will be proud.

Lastly, thank you God. I am here because of you.

Abstract

Frictional mechanical metamaterials are a class of metamaterials engineered to dissipate energy through internal friction when subjected to external forces. Unlike conventional metamaterials that rely on plastic deformation or viscoelastic materials for energy absorption, frictional mechanical metamaterials can exhibit viscoelastic-like behaviour even when composed of purely elastic materials. This unique property is governed by the internal structure of the unit cell and the contact surface topography, which influence the frictional interactions within the metamaterial. Despite their potential for applications in energy dissipation and impact mitigation, the optimal architectures and scaling laws governing their performance remain underdeveloped. Similarly, the role of frictional metasurfaces—planar structures that leverage artificial surface designs to enhance frictional interactions—has not been systematically explored in the context of energy dissipation.

This research addresses these gaps by developing novel frictional mechanical metamaterials and metasurfaces designed to maximise repeatable energy dissipation per unit volume. A comprehensive approach combining finite element (FE) simulations, theoretical modelling, and experimental validation was employed to investigate the mechanical behaviour of these metamaterials. Through iterative design and analysis, a pinwheel-based internal structure was introduced to optimise the contact area and enhance energy dissipation while maintaining a compact unit cell volume. Additionally, metasurface designs incorporating right-angled isosceles triangles, rectangles, and semi-elliptical patterns were explored to assess their impact on peak force and energy dissipation efficiency.

Experimental validation was conducted using materials with both linear and nonlinear mechanical properties. For TPU 95A, a hyperelastic and viscoelastic polymer, a refined simulation approach was developed to capture its complex mechanical response. Theoretical models were modified to incorporate internal damping elements, ensuring better alignment with experimental results. These studies demonstrated that strategic modifications to internal structure geometry, contact surface topography, and material selection could significantly enhance energy dissipation performance.

The findings of this research contribute to the fundamental understanding of frictional metamaterials and metasurfaces, offering new design principles for optimising their mechanical performance. The proposed architectures have broad applicability in various industries, including high-performance braking systems, aerospace vibration damping, protective gear such as reusable helmets, and earthquake-resistant structural elements. By bridging the gap between theoretical

design, numerical modelling, and experimental validation, this study lays the groundwork for future advancements in frictional mechanical metamaterials and their real-world implementation.

Table of Contents

List of Tables

List of Figures

Glossary

AM	Additive manufacturing
CAD	Computer aided design
CPE	Chlorinated polyethylene
CoF	Coefficient of friction
FDM	Fused deposition modelling
FE	Finite element
FEA	Finite element analysis
RVE	Representative volume element
TPU	Thermoplastic polyurethane

CHAPTER 1: INTRODUCTION

Frictional mechanical metamaterials feature distinctive internal friction elements where energy dissipation occurs via frictional mechanisms. These metamaterials can be tailored to obtain desired properties by adjusting geometrical parameters, offering potential applications in diverse industrial fields, including construction, automobile, and aerospace, among others. For instance, an automobile brake is the most well-known application to induce energy dissipation via friction.

Recent advances in metamaterials have inspired engineers who attempt to develop materials with properties that cannot be found in conventional existing materials. Indeed, a number of papers on energy dissipation and absorption using metamaterials have been found in the published literature. However, most studies were on plastic deformation of sandwich composite structures or lattice structures, or buckling of multi-stable structures, rather than energy dissipation by friction. Despite the superior energy absorption capability of sandwich panel structures, their permanent deformation during a single energy absorption event renders them unsuitable for repeated use. In the case of buckling in multi-stable metamaterials which is also known as snapping-based metamaterials, these structures require mechanical reloading in the opposite direction to turn back to their original form. Research on repeatable energy dissipation experiments utilising frictional mechanical metamaterials is currently in its early stages, with standardised parameters for efficient energy dissipation yet to be established.

To achieve the desired hysteresis behaviour, most traditional industrial products for energy dissipation and absorption rely on the way of plastic deformation or fragmentation. In addition, to control the deformation pattern in an intended way, artificial defects such as origami and kirigami are commonly adopted. Although energy dissipation through plastic deformation or fragmentation is highly effective in absorbing a large amount of energy, a limitation is that such systems are often designed for one-time use due to permanent structural changes, unless they are specifically engineered for reusability.

Metamaterials would be finely tuned, not just by altering their internal structure, but by manipulating the surface geometry, also referred to as metasurfaces. Metasurfaces are essentially two-dimensional metamaterials where surface design plays a key role in determining properties like frictional coefficients. By adjusting the geometry of these metasurfaces, we can control and enhance the material's energy dissipation capabilities, which opens avenues for various industrial applications, including construction, automotive, and aerospace industries. Limited research has been conducted on friction metasurfaces, and no scaling law could be found on energy dissipation changes depending on the size of the unit cell of viscoelastic metamaterials.

This research aims to advance the state of the art in repeatable energy dissipation, develop an

understanding of the mechanics of frictional metamaterials and metasurfaces, and build prototypes to verify the performance of the design. As part of this research, specimens of individual metamaterial unit cells with unique topologies have been fabricated. Mechanical tests have also been performed on these test specimens to measure their energy dissipation performance. In addition, FE (finite element) simulations using CAD models consisting of multiple frictional metamaterial unit cells, as well as single unit cell models, have been performed to extrapolate the energy dissipation performance of the metamaterial system. In this study, two main filament materials were used to fabricate the metamaterials: CPE HG100, which is somewhat stiff and has elastic properties, and TPU 95A, which is soft and exhibits both hyperelastic and viscoelastic properties. The theoretical model was initially developed based on CPE HG100, and then factors were added to incorporate hyperelastic and viscoelastic properties as TPU 95A was used.

The objective of this research is to demonstrate both high energy dissipation capability and repeatability, without fracture for multi times usage, through the development and comparison of theoretical, FE simulation, and experimental models. Although the primary focus is on developing the specific structure to maximise energy dissipation, this study also broadens the knowledge of mechanical properties for frictional mechanical metamaterials and expands the scope of design applications in industries that require energy dissipation such as automobiles, biomedical, sports equipment, and earthquake protection systems of constructions.

1.1 Motivation

The pursuit of innovation in structural engineering has led researchers to explore unconventional avenues for addressing challenges in various industries. One such avenue is the development of frictional mechanical metamaterials, which aim to generate energy dissipation through controlled friction mechanisms.

The idea of reducing the friction energy to achieve the efficiency of work in industry fields, such as vehicle tyre and ski blades, had already become familiar to application developers, whereas there are also other situations in which it is necessary to maximise energy dissipation through friction such as brake systems of automobile and aircraft. Here, we felt the need to study the structures for maximum energy dissipation.

Beyond just manufacturing and experimenting, we aspire to uncover both FE simulation and theoretical models for the designed frictional mechanical metamaterials made of hyper- and viscoelastic materials as well as elastic constituent materials. This deeper understanding will not only contribute to the optimisation of metamaterials but also advance the broader field of metamaterial research. As the field progresses, the potential impact of frictional metamaterials on industries and our understanding of metamaterials will increase, opening new doors for

innovation and problem solving. We wish our research will lay the groundwork for that positive influence.

1.2 Research gaps and research questions

From the preliminary literature review, three research gaps have been identified as below.

First, while mechanical metamaterials have received attention for their counterintuitive properties, much of the research has focused on the buckling of multi-stable structures, lattice structures, and plastic deformations. Research on repeatable energy dissipation experiments using frictional mechanical metamaterials is just underway by a small number of researchers, and standardised parameters for efficient energy dissipation have not yet been established.

Second, the shape and roughness of the contact surface is one of the important factors affecting energy dissipation. The literature shows that previous researchers have not attempted to increase energy dissipation by introducing frictional metasurfaces into frictional metamaterials.

Third, for soft materials, the load-displacement plots exhibit nonlinear behaviour, which is different from the linear behaviour of elastic materials, and appropriate simulation models and theoretical models to represent them are not well introduced for developing mechanical metamaterials. Therefore, there is a need to develop reliable FE simulation models and theoretical models for metamaterials fabricated using non-linear soft materials characterised by inherent damping.

These research gaps lead to the following three research questions:

RQ1. What internal structure in a unit cell of frictional mechanical metamaterials maximises energy dissipation per unit volume without fracture under repetitive external forces?

RQ2. How does the metasurface design affect the maximum friction force and energy dissipation per unit volume?

RQ3. What methods should be applied to develop FE simulation models to represent the properties of metamaterials using nonlinear soft materials? What factors should be employed in the theoretical model to represent the internal damping?

1.3 Thesis outline

Chapter 1 presents the introduction of the thesis along with motivation, research gaps and questions, and thesis outline.

Chapter 2 describes an overview of the literature on the various types of metamaterials intended for energy dissipation and absorption especially via friction mechanisms. This chapter begins with

a history of metamaterials, followed by a summary of the types of metamaterials, previously proposed frictional metamaterials, types of friction, frictional metasurfaces, the additive manufacturing techniques, and the methods used to obtain energy absorption and dissipation.

Chapter 3 illustrates the design of 3D metamaterials and the fabrication of unit cells that are being presented in this study. An overview of the finite element method and the compression experimental methodology are also presented. These metamaterial's geometries are based on the combination of hexagonal or re-entrant outline frames with internal structures such as cantilever beams to induce energy dissipation by friction when external force is applied to the unit cell model. The finalised CAD and fabricated models are investigated in subsequent chapters with theoretical, simulation and experimental models to demonstrate their sliding friction performance.

Chapter 4 explores the whole procedure of studying a linear frictional mechanical metamaterial made of CPE HG100, including comparing among with the theoretical, experimental, and finite element model's results.

Chapter 5 investigates the properties of a nonlinear frictional mechanical metamaterial made of TPU 95A, a type of hyperelastic and viscoelastic material. Unlike typical elastic materials, this kind of material responds nonlinearly to a stress-strain curve which leads to complicated interpretation. ANSYS Workbench, a commercial simulation software, provides a variety of hyperelastic models. In this study, Mooney-Rivlin's 3rd order is used to perform the curve fitting.

Chapter 6 describes the study of the performance of frictional mechanical metamaterials with metasurfaces of various patterns, a step up from previous frictional metamaterials with only flat contact surfaces. Isosceles triangular, rectangular, and semi-elliptical patterns were applied to the contact surfaces of the modified unit cell metamaterial and analysed by comparing simulation and experimental results.

Chapter 7, as the last chapter, presents the conclusions of the thesis and provides contribution, limitations and future works like further research as well as investigations.

CHAPTER 2: LITERATURE REVIEW

The chapter begins by introducing the history and types of metamaterials, and more specifically describes metamaterials created for the purpose of energy dissipation and absorption. As this is a newer area of research, only recently have few frictional metamaterials been reported, and those will be discussed in more depth. We will also present constituent materials, a general method of additive manufacturing for fabricating metamaterials.

2.1 History of metamaterials

The word ‘metamaterial’ is the combination of ‘meta’ which means ‘beyond’ from Greek and ‘materia’ from Latin meaning ‘matter’ or ‘material’. Metamaterials are novel materials that have a counterintuitive property that is not found in monolithic materials in nature [1]. The concept of metamaterials was first introduced by Russian theorist Veselago in 1968, suggesting the theoretical possibility of materials exhibiting both negative permeability and negative permittivity. The commonly recognised term for this innovative material is Left-Handed Materials (LHM) or negative-index material, familiar to many inventors and individuals alike [2, 3]. In 1999, John B Pendry sought practical methods to create LHM that diverged from the traditional right-hand rule. LHM establishes a relationship between the wave propagation vector and the pointing vector, representing the flow of wave propagation energy [4]. In 2001, Smith unveiled a novel LHM exhibiting concurrent negative permeability and permittivity. His work included conducting microwave experiments to validate its distinctive properties [5]. Subsequently, Lucent Technologies spearheaded advancements in metamaterials in 2002, particularly for resonant antenna production. By 2005, these materials were being leveraged for their unique electromagnetic properties. In 2017, software developments enabled the commercial availability of metamaterial-based satellite antennas [1]. Figure 2.1 describes a schematic flowchart showing the major historical evolution of metamaterials.

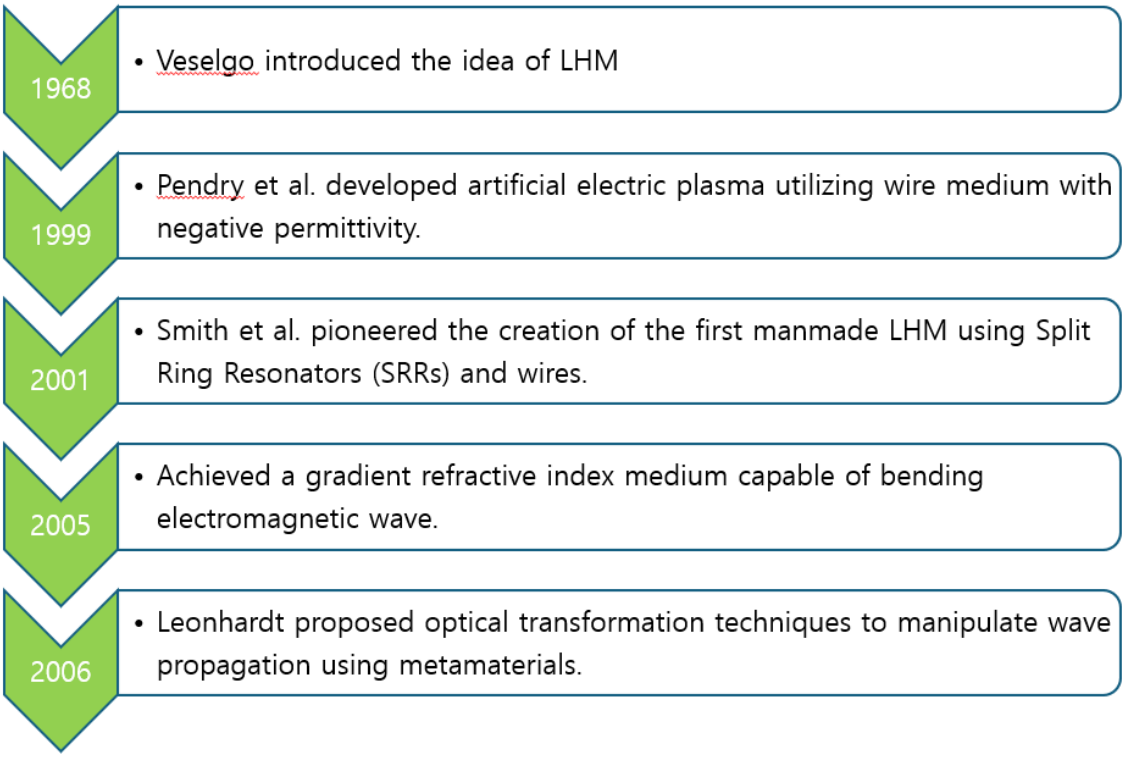

Figure 2.1. The development of metamaterials throughout chronicle [3, 6-9].

2.2 Types of metamaterials

Metamaterials have attracted great interest in different fields over the past few decades due to their unique features, which can be applied in the field of application development including electromagnetic cloak [10, 11], acoustic absorption [12, 13], Millimetre-Wave waveguide [14], and elasto-mechanical unfeelability cloak [15]. They are a smart or novel class of man-made invented materials that can embody mechanical, thermal, electromagnetic, and acoustic properties that do not occur naturally, such as negative stiffness [16-19], and negative refractive index [20-22]. Some of these materials exhibit zero or negative values of Poisson's ratios [23-27], which are rarely found in nature. In addition, metamaterials also offer great design flexibility owing to their tailored properties and the possibility of tuning them in response to external stimuli [28, 29]. These attractive properties have enabled metamaterials to inspire the development of new devices and concepts and to be utilised in a variety of new applications. Metamaterials have therefore found wide applications in the medical field [30], automotive [31, 32], aerospace [33], and in a wide range of devices such as biosensors [34, 35], noise controllers [36, 37], underwater sonar systems [38, 39], energy harvesters [40, 41], seismic structures [42, 43], tuneable filters [44], and even antennas to control the propagation of electromagnetic waves [45].

There may be some variation in how researchers classify metamaterials. However, in general, according to the functionalities of metamaterials, currently developed metamaterials can be roughly classified into four categories – Electromagnetic, Acoustic, Thermal, and Mechanical metamaterials [46, 47]. Figure 2.2 explicitly illustrates the types of metamaterials with respective characteristics.

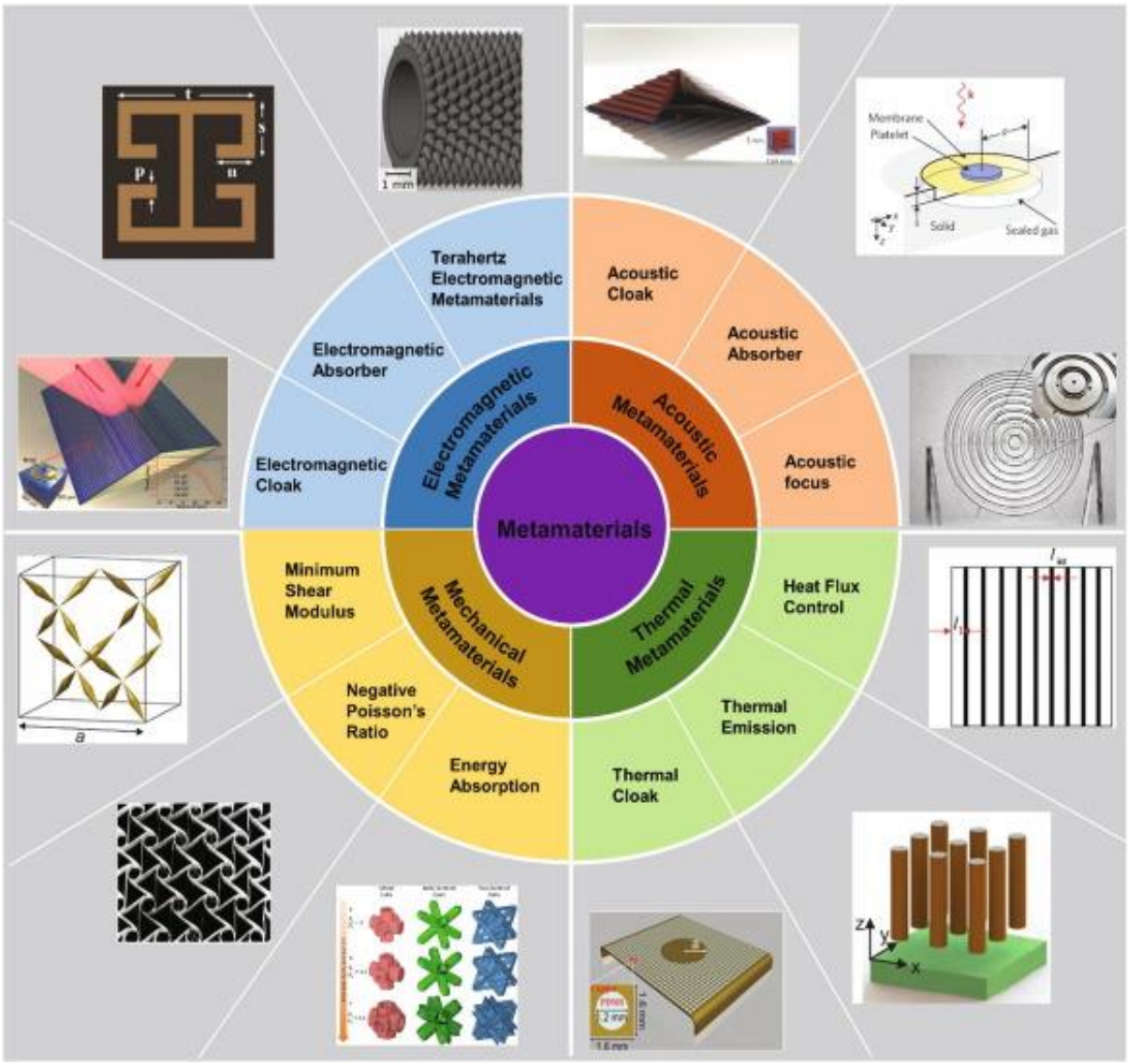

Figure 2.2. The categorisation of metamaterials according to their functional properties [46].

2.2.1 Mechanical Metamaterials

Mechanical metamaterials are a fascinating class of engineered materials that defy conventional mechanical properties and exhibit unique and tailored responses to external forces. These materials derive their exceptional mechanical characteristics from carefully designed architectures rather than the intrinsic properties of the materials of which they are composed.

Mechanical metamaterials have gained significant attention in recent years due to their potential for revolutionising various engineering applications, ranging from lightweight structures [48] to impact-resistant materials [49]. One key characteristic of mechanical metamaterials is their ability to achieve a negative Poisson's ratio, a property known as auxetic behaviour [50]. In conventional materials, when you stretch them in one direction, they contract in the perpendicular direction, resulting in a positive Poisson's ratio. However, auxetic materials expand in both directions when stretched and contract when compressed [51]. This unique behaviour can be advantageous in applications such as impact protection, where materials with a negative Poisson's ratio can absorb and dissipate energy more effectively [52]. Another aspect of mechanical metamaterials involves exploiting geometric arrangements to achieve unprecedented mechanical properties. This includes the use of lattice structures [53], architected materials [54], and origami or kirigami-inspired designs [55-57]. For example, the creation of truss-like structures can impart materials with high stiffness and strength while maintaining a lightweight composition. These lattice structures are designed with carefully engineered unit cells that optimise the material's performance in specific directions [58].

One prominent example of mechanical metamaterials is the creation of so-called buckliball structures [59], which are lattice-based materials inspired by the buckyball molecule in Figure 2.3a. These structures exhibit exceptional resilience and impact resistance due to their unique geometric arrangement. The buckliball design has potential applications in creating lightweight, impact-resistant materials for use in sports equipment, aerospace components, and protective gear [60]. Additionally, mechanical metamaterials can be designed to possess tunable mechanical properties [61], allowing for adaptability in different environments or applications. By incorporating smart materials that respond to external stimuli, such as heat [62, 63], pressure [64], magnetic fields [65, 66], or light fields [67, 68], these materials can change their mechanical behaviour on demand. This tunability opens opportunities for the development of reconfigurable structures and adaptive materials that can be tailored to specific tasks. Figure 2.3b describes examples of elastic metamaterials responding to external stimuli [69]. In the realm of seismic engineering, mechanical metamaterials have the potential to mitigate the impact of earthquakes [70, 71]. Researchers are exploring the development of metamaterials that can control and redirect seismic waves, protecting structures from damage. The ability to engineer materials with specific wave propagation characteristics offers a promising avenue for enhancing earthquake resilience in buildings and infrastructure.

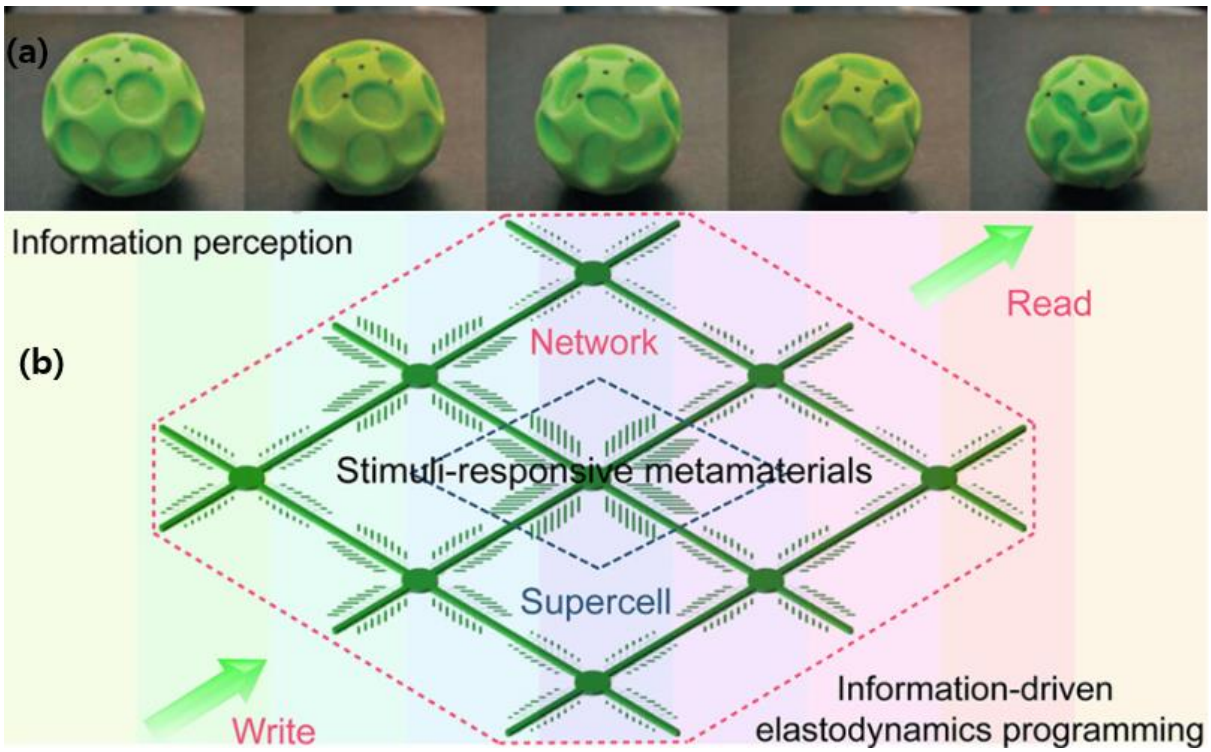

Figure 2.3. (a) Buckliball, composed of silicone-based rubber [72]. (b) Adaptive metamaterial notch filters with an intrinsic awareness of stimulation information [69].

Typical mechanical metamaterials exhibit close correlations with four key elastic properties: Young's modulus (E), shear modulus (G), bulk modulus (K), and Poisson's ratio (ν). Among them, Young's modulus, shear modulus, and bulk modulus assess the material's stiffness, rigidity, and compressibility, respectively. Poisson's ratio, an elastic constant for isotropic materials, serves as a fundamental measure for comparing the structural behaviour of any real material, regardless of homogeneity, under elastic strain. It quantifies how much a material contracts laterally when stretched longitudinally.

Figure 2.4a illustrates the 3 different types of deformation to express E, G, and K. Each constant is closely related and can be expressed by the following Equation 2.1 to 2.4. These equations apply to the finite element analysis software so that when the material properties are partially entered, the remaining properties that are not input can be automatically calculated.

$$E = 2G(1 + v) \tag{2.1}$$

$$E = 3K(1 - 2v) \tag{2.2}$$

$$G = \frac{E}{2(1+v)} \tag{2.3}$$

$$K = \frac{E}{3(1-2v)} \tag{2.4}$$

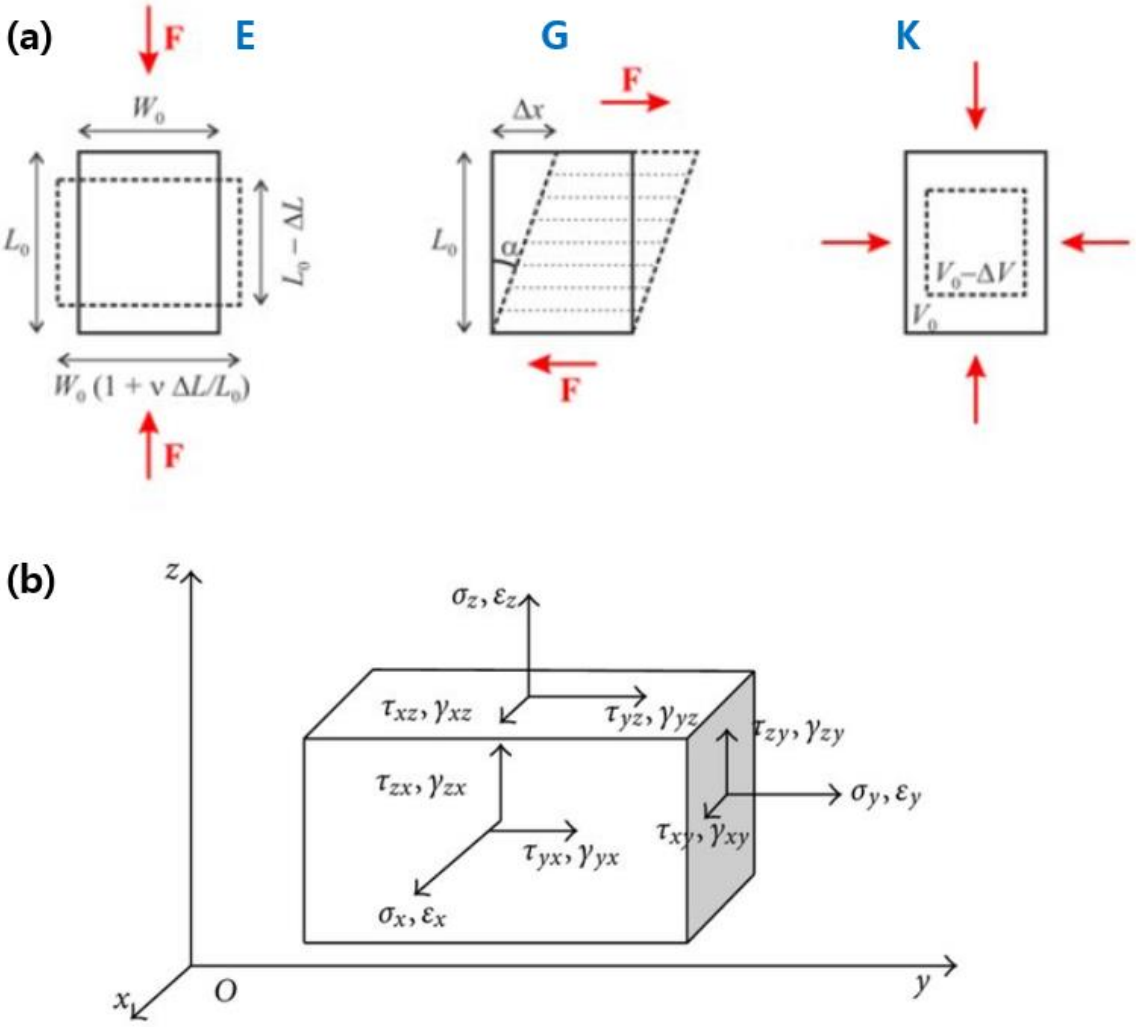

Figure 2.4. (a) Experimental setups for measuring the Young's modulus E (left), the shear modulus G (right), and the bulk modulus K (right) [73]. (b) Scheme of three-dimensional stress and strain components on the elemental elastic body [74].

Figure 2.4b illustrates an elastic block with sides aligned with the coordinated axes. To describe stress on each pair of parallel sides of a cubic element, one symbol represents the normal stress component σ, while two symbols denote shearing stress components τ. From Hooke's law, the linear correlation between stress components and strain components during slight deformations

would be established like Equation 2.5.

$$\varepsilon_x = \frac{\sigma_x}{E} \tag{2.5}$$

Here, E represents Young's modulus, also known as the modulus of elasticity. Put simply, E is defined as the ratio of uniaxial stress (σ) under external tensile or compressive conditions to strain (Ɛ), measured along the corresponding axis.

Materials exhibit significant differences in volume changes when subjected to mechanical loads that cause distortion. Poisson's ratio offers a means to compare how materials respond to elastic strain by placing their performance within specific numerical ranges. Consequently, when extending an element in a specific axis direction, corresponding lateral strain components typically go with this deformation. When combining the strain components generated by the three stresses, the connection between elongation and stress is determined by Young's modulus and Poisson's ratio (Equation 2.6, 2.7, and 2.8).

$$\varepsilon_x = \frac{1}{E}(\sigma_x - v(\sigma_y + \sigma_z) \tag{2.6}$$

$$\varepsilon_y = \frac{1}{E}(\sigma_y - v(\sigma_z + \sigma_x)) \tag{2.7}$$

$$\varepsilon_z = \frac{1}{E}(\sigma_z - v(\sigma_x + \sigma_y)) \tag{2.8}$$

Here, v represents Poisson's ratio and is defined as the negative ratio of transverse strain to axial strain in a material body that is elastically stretched (Equation 2.9). When subjected to axial stretching, most solids tend to contract laterally, indicated by negative values for ε_y and ε_z, in contrast to the positive ε_x. The Poisson's ratio of most substances that exist in nature is positive, with conventional materials such as polymers and metals ranging from 0.25 to 0.35. For brittle materials like glasses, the Poisson's ratio approaches zero, indicating minimum lateral deformation under axial loading [75].

$$v = -\frac{d\varepsilon trans}{d\varepsilon axial} = -\frac{d\varepsilon y}{d\varepsilon x} = -\frac{d\varepsilon z}{d\varepsilon x} \tag{2.9}$$

Mechanical metamaterials can be categorised into subcategories based on their properties. Xianglong Yu *et al* subdivided mechanical metamaterials into four sub-items according to Young's

modulus, shear modulus, bulk modulus and Poisson's ratio [76].

Young's modulus E describes the relative stiffness of a material that is defined as a slope of the elastic line of a stress-strain graph, shear modulus G is a measure of the ability of a material to resist transverse deformations and is also known as the slope of the elastic line in the shear stress - shear strain diagram. Bulk modulus K is the measure of the decrease in volume with an increase in pressure, and Poisson's ratio ν which is the ratio of lateral strain to the longitudinal strain, became the criteria for classifying mechanical metamaterials.

They classified mechanical metamaterials in detail as shown in Figure 2.5 based on the four elastic constants. For example, the first group of metamaterials in Figure 2.5 are relative to Young's modulus E. Micro/nanolattices and origami metamaterials have a property of strong lightweight (E/density, ρ). Pattern transformation metamaterials show a tuneable stiffness E. The two metamaterials in the second group, pentamode metamaterials ($G<<K$) and negative compressibility ($-4G/3 < K < 0$), are classified based on the relationship between the shear modulus G and bulk modulus K. The last group of mechanical metamaterials, auxetic metamaterials are classified as known to have a negative Poisson ratio (ν).

Their extensive overview of mechanical metamaterials is well organised and clear, but no mention of frictional mechanical metamaterials was found. Very little research has been conducted on friction mechanical metamaterials, which was a very challenging research gap during the literature review. Only very recently have some studies of frictional mechanical metamaterials that generate energy dissipation has been reported. Some published examples are presented in Section 2.3.

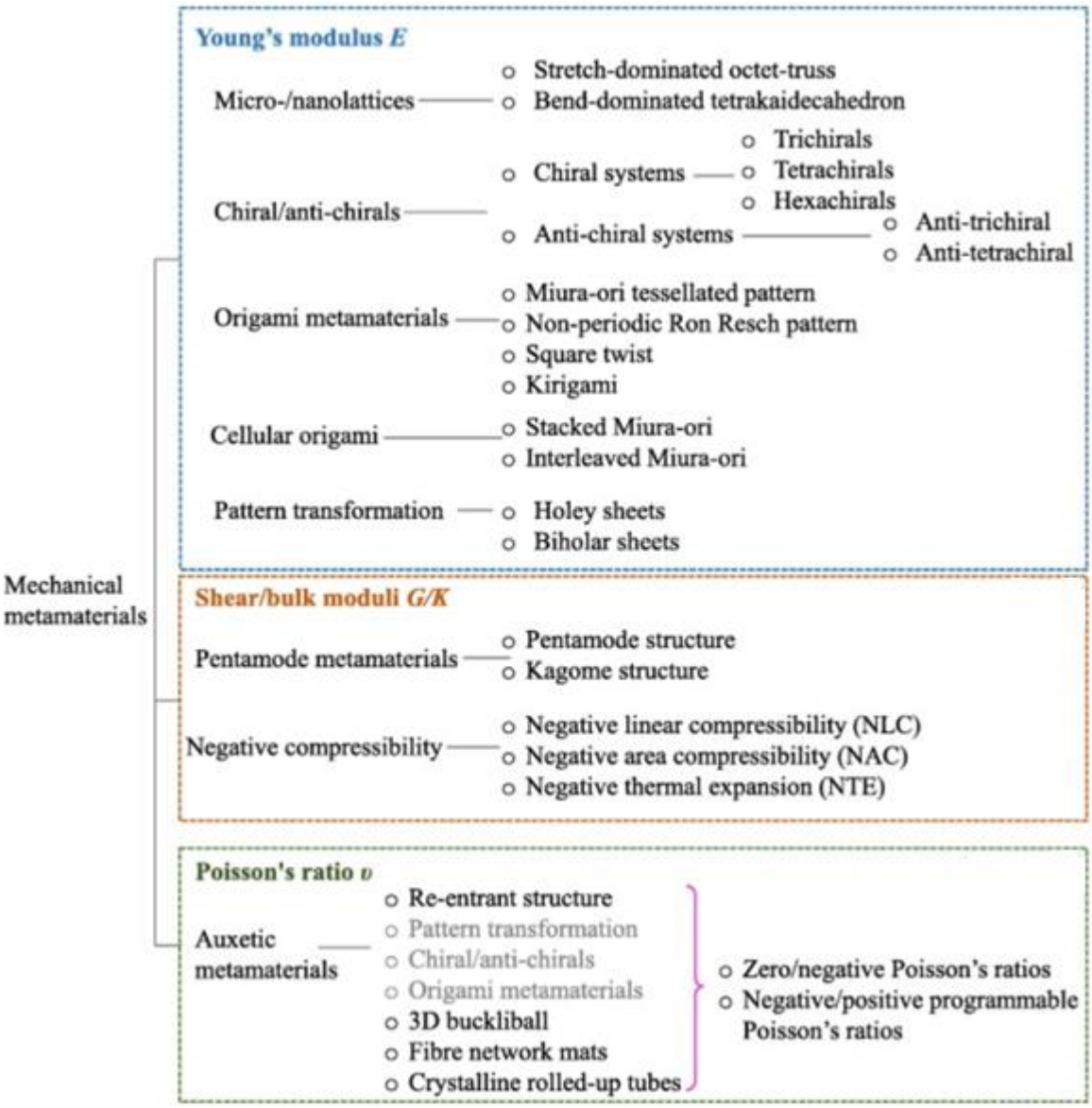

Figure 2.5. Classification of mechanical metamaterials [76].

2.2.1.1 Auxetic metamaterials

Auxetic metamaterials are a fascinating subset of mechanical metamaterials characterised by their unique behaviour of expanding in lateral directions when stretched longitudinally [26, 77]. This counter-intuitive property arises from their intricate internal structure, which often includes re-entrant geometries or specially designed unit cells.

Recent studies have explored methods to tune the auxetic behaviour of metamaterials by adjusting parameters such as geometry, material properties, and loading conditions. By carefully controlling these factors, researchers have demonstrated the ability to create auxetic metamaterials with programmable mechanical properties, opening up new possibilities for applications in areas such as impact protection, soft robotics, and biomedical devices.

Figure 2.6 schematically illustrates the difference in indentation resistance between auxetic and non-auxetic structures. In contrast to conventional structures like hexagonal honeycombs, when subjected to localised impact on the auxetic structures, the material beneath the impact zone of auxetic structures flows inwardly towards the point of impact. Consequently, this inward flow increases the local density of the material, thereby enhancing its resistance to indentation. This stands in stark contrast to the outward flow observed in conventional structures, which tends to decrease indentation resistance by reducing material density [78-82].

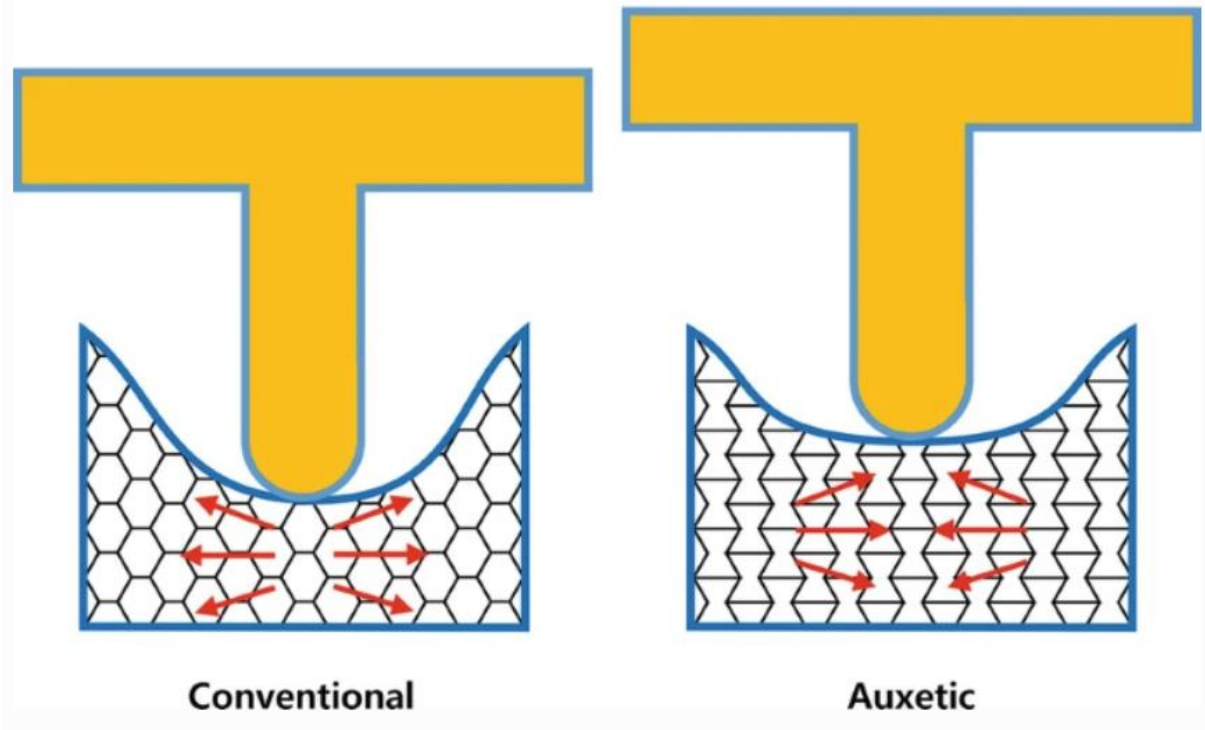

Figure 2.6. Variations in deformation response and indentation resistance between conventional non-auxetic and auxetic structures [83].

Common auxetic structures encompass re-entrant structures, semi-rigid designs, and chiral structures. In particular, the re-entrant structure in Figure 2.7a was of great interest during the unit cell design process, and in fact, it was adopted as one of the central structural frames for presented frictional metamaterials in the later chapters.

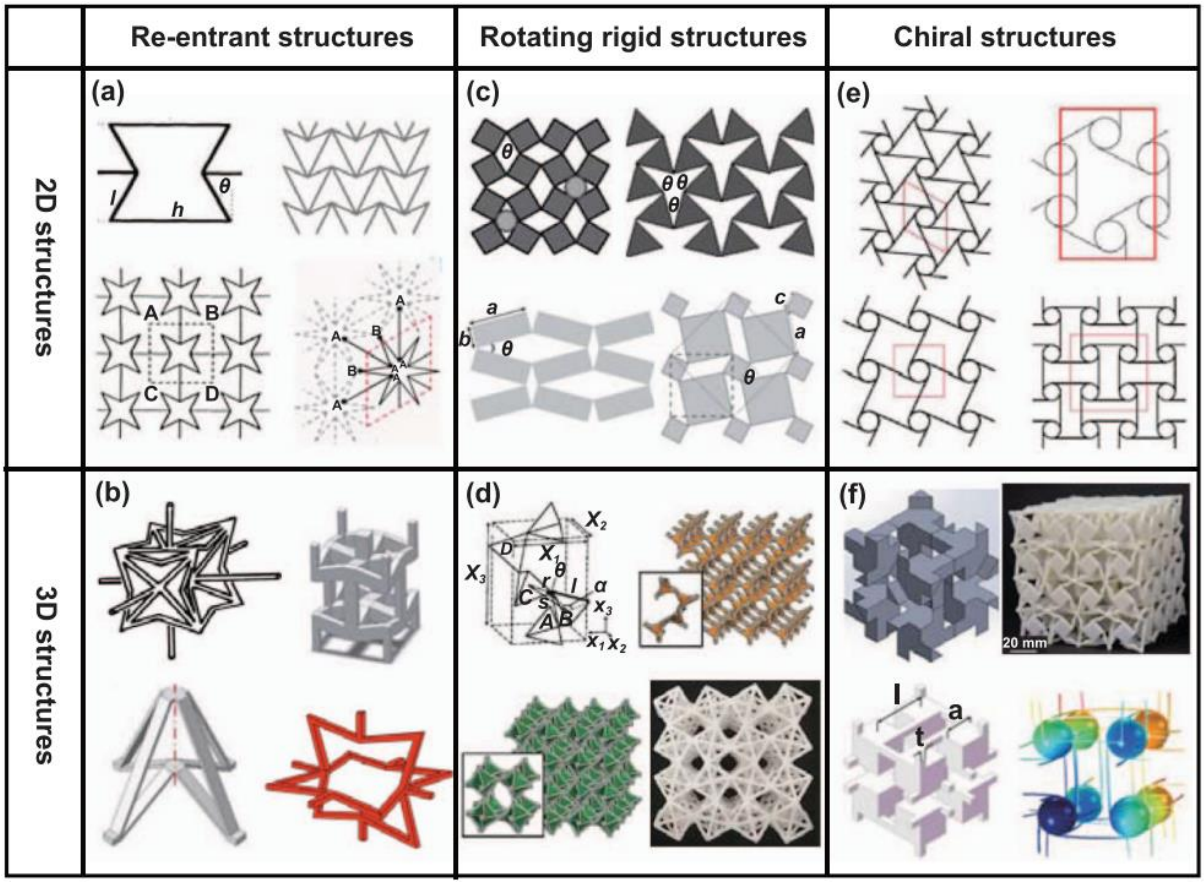

Figure 2.7. Presented classical 2D and 3D auxetic structures from the previous researchers [84].

2.3 Frictional mechanical metamaterials for energy dissipation

Geometries of mechanical metamaterials for energy absorption and dissipation have been designed by various researchers through their intuition or inspiration from nature. Traditional mechanical metamaterials have been developed with the aim of generating significant amounts of energy absorption through plastic deformation, which has the disadvantage of being a one-off use. To develop reusable metamaterials, designs with bistable mechanical behaviour have been proposed. Bi-stable materials are well known for the characteristic of two or more stable mechanical configurations and each stable state corresponds to a different arrangement of the material's internal structure.

Research papers dealing with frictional mechanical metamaterials have been scarce, and in fact, only a few studies can be found in the literature regarding mechanical metamaterials that intentionally generate energy dissipation by friction. The limited research papers were continuously reviewed for clues on how to develop frictional mechanical metamaterials. Although there is no single definition of frictional mechanical metamaterials in universal use, frictional mechanical metamaterials were used to mean metamaterials that dissipate repeated external load

and unload energy inputs by inner structures sliding over each other [85].

2.3.1 Coulombic friction

A novel metamaterial with unit cells for energy dissipation by sliding coulombic friction was proposed by Garland *et al* [85]. They created a friction unit cell with extra structures inserted inside that slide past one another when the cell is being loaded and unloaded, causing frictional dissipation, as well as a honeycomb-shaped open unit cell with no internal features to illustrate the idea of frictional metamaterials (Figure 2.8). Then, using three distinct additive manufacturing techniques on two distinct length scales, they fabricated all two types of the aforementioned unit cell kinds from three different materials. Program load sequences were subjected to macroscopic compression experiments. To demonstrate that frictional metamaterials can function in extreme thermal circumstances, they periodically loaded and unloaded the metal unit cell under two distinct temperature settings.

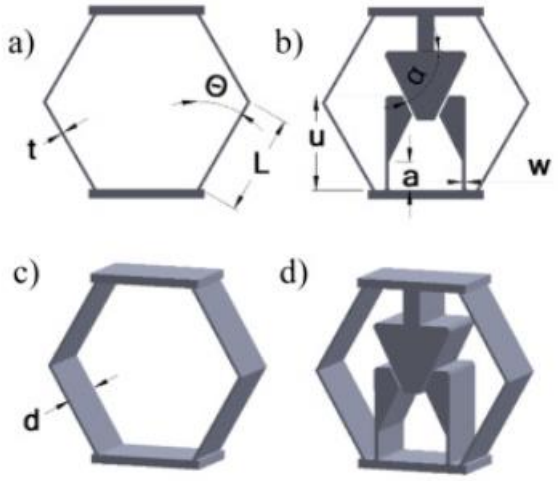

Figure 2.8. Conceptual models proposed by Sandia Lab. (a) 2D open unit cell without Coulombic friction elements. (b) 2D frictional unit cell with Coulombic friction elements (two cantilever beams and a central arrow shape structure). (c) Isometric view of the open unit cell. (d) Isometric view of the frictional unit cell [85].

By modelling, fabrication, and experiments of friction metamaterials, they were able to show the superior energy dissipation ability of suggested frictional cells compared to open cells. Their research also demonstrated that the energy dissipation in each unit cell is influenced by variations in materials, sizes, and even additive manufacturing techniques. Notwithstanding the aforementioned scholarly accomplishments, the majority of their research was devoted to illustrating the general characteristics of frictional metamaterials; they did not provide any particular details regarding structure optimisation to maximise the energy dissipation property. They assumed that the unit cell is in the assembled metamaterials and is therefore constrained by

the next unit cell while creating a linear analytical model for an open and a friction unit cell. This resulted in an underestimation of the hexagonal unit cell's stiffness. As a result, there was a discrepancy between the force-displacement curves of FEA and the experiment result. Other possible candidate materials should be examined in the future, as indicated by the fact that just three materials were employed in their tests. Furthermore, no numerical or visual results have been provided to examine the optimal additive manufacturing technique. The fact that the entire unit cell must be rebuilt when the contact surface wears out is another drawback of the model they introduced.

McCrary *et al* created a novel bidirectional mechanical metamaterial for energy dissipation through the sliding phenomenon when planar loading is applied on the surface [86]. Four spirals make up the suggested model, each with four straight walls separating the inner tip of the spiral from its border wall (Figure 2.9). Their energy dissipation conceptual design adhered to the typical parameterisation procedure, which has the benefit of being able to tailor to the desired material properties. They specified the parameters, which are elements of the unit cell like wall thickness and width, this work aided in the research of comparing changes in the properties of metamaterials as dimensions were changed. Compression cyclic tests demonstrated the reversibility and repeatability of the metamaterial prototype. The energy loss in the tests was 8.3 % lower to 12.5 % higher than in their simulations, indicating a strong correlation and trust in the computational framework's conclusions. However, their FE models neglect the influence of surface wear on the part's energy loss, therefore an advanced computational framework could be required. Furthermore, the effects of surface wear and other tribological features on the physical test performance have not received much attention.

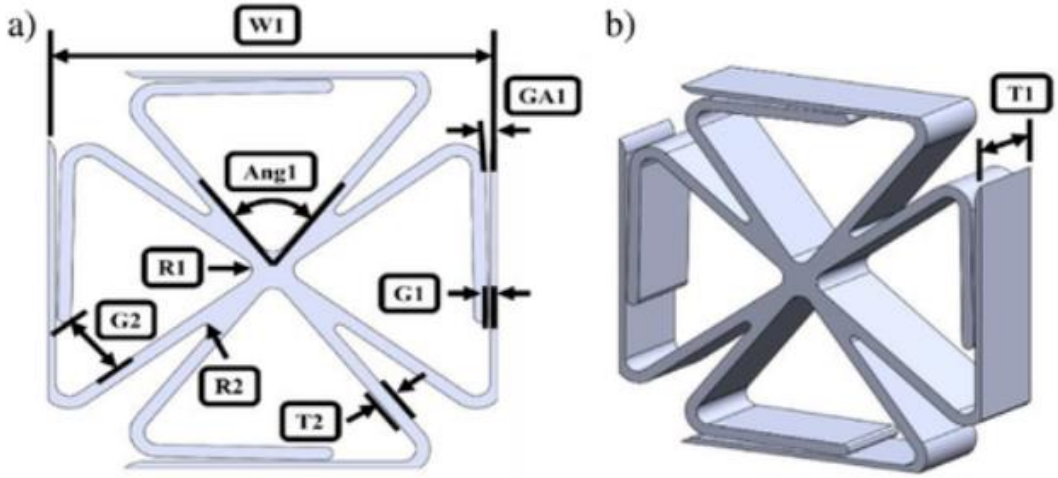

Figure 2.9. A conceptual design of frictional metamaterial to bi-directional energy dissipation (a) 2D view with parameters (b) 3D view of the model [86].

Lv *et al* proposed an I-shaped structure with an orthogonal beam designed inside to induce energy dissipation through a combination of Coulomb friction contact and vibration. Their quasi-static loading-unloading tests were conducted and validated by using FE simulations [87].

The energy dissipated by the proposed structure can be divided into two factors, vibration and friction, and the energy dissipated by each of the two components was expressed quantitatively using theoretical formulae. They also demonstrated that the deformation of their proposed model occurs within the elastic range by showing that the structure fully recovers after removing the external load (Figure 2.10). They also emphasised that the energy consumption efficiency of their model can be tuned by modifying its geometrical parameters. The structure's ability to absorb energy can be improved by enlarging the protrusion size and vertical length of the plugs, extending the thickness of the cantilever beams, and modifying the relative lengths of the cantilever beams. The cyclic compression experiments they ran show that their suggested model has the advantage of good reusability.

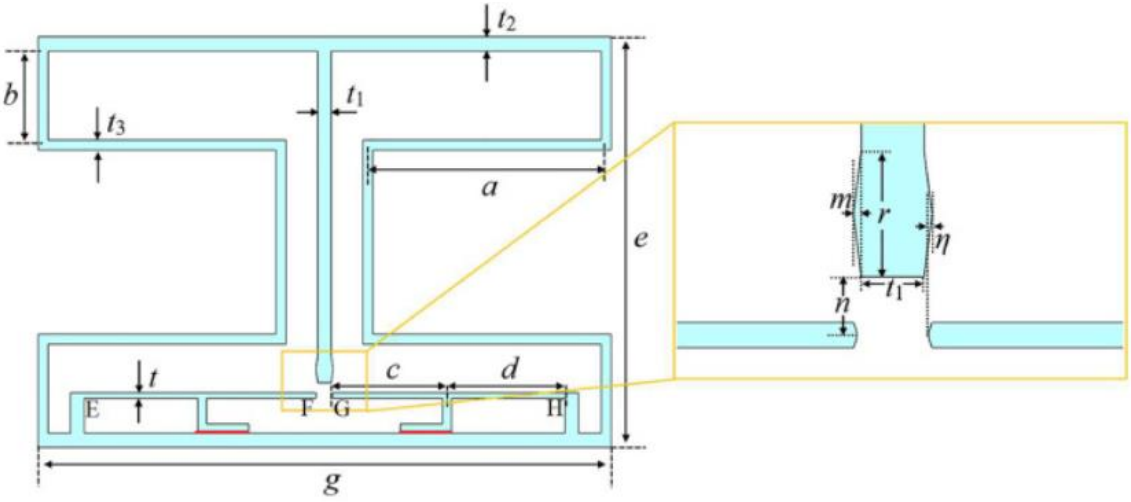

Figure 2.10. A proposed I-shaped geometry with major geometric dimensions [87].

2.3.2 Interference fit

According to Jinyou *et al.*, many existing designs struggle to possess both high and repeatable energy-absorbing capabilities, and common energy-absorbing materials display an inverse relationship between energy-absorbing capability and reusability (Figure 2.11) [88]. They suggested a brand-new architecture consisting of reinforced elastomer and stiff rods that can absorb energy by sliding past one another. The tendon-bone interaction found in the human body had inspired this novel structure. Soft elastomer and stiff frame, which consists of a porous rigid frame intertwined, are the two components of reinforced elastomer. Each of the seven hexagonal columns that make up the architectural geometry is composed of several hexagonal cells. Each

column has four straight, column-shaped holes with a radius of 0.9 mm, and when steel rods with a radius of 1mm are driven into the holes by subjected external force, pressure is generated owing to the difference in diameter between the holes in the reinforced elastomer and the steel rods. They demonstrated that the intertwined structure with a smooth edge performs best in terms of energy absorption ability and reusability by conducting compression experiments using three different types of cells at a constant load speed of 500 mm/min.

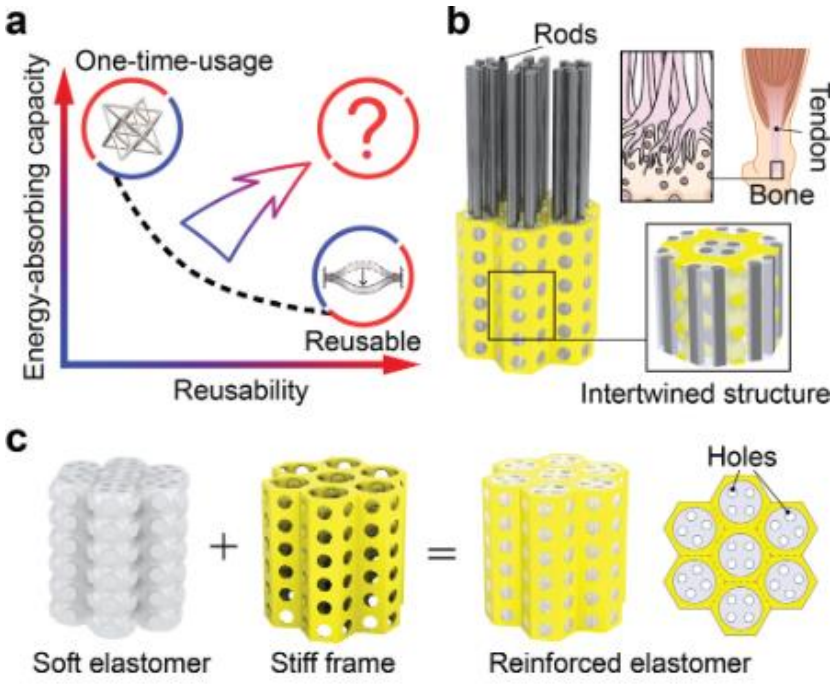

Figure 2.11. (a) Inverse relationship between energy-absorbing capacity and reusability in conventional energy-absorbing materials. (b) The structure of the proposed novel material and tendon bone interface. (c) The reinforced elastomer consisted of a soft elastomer and a stiff frame [88].

They also investigated how compression speed influences variations in energy absorption capabilities. The plateau yield force Fp varies with compression speed v, indicating that either coefficient friction μ or normal force N, or both, are impacted by v. More quantitative studies have revealed that both are the result of the synergistic effects of elastomers' two symbolic features, the rate-dependent coefficient of friction and the nonlinear hyper-elastic characteristic in large deformation. A tribometer was used to calculate the frictional coefficient between silicone elastomer and steel rods. Experiment results display that raising v from 57 to 471 mm/min leads to a 30% increase in the coefficient of friction, while around 60% increase in plateau force. This indicates that both μ and N increased with increasing v. They explained that this conclusion was caused by the elastomer's nonlinearity and geometric properties, which were confirmed using a FE model. Jinyou *et al*. proposed a revolutionary design structure that addressed two essential

requirements: high energy absorption efficiency and reusable. In fact, their innovative energy-absorbing structure performs better than existing energy-absorbing materials in terms of both high absorption capacity (10kJ/kg each cycle) and exceptional reusability (more than 200 cycles). However, it took roughly 10 minutes for the compressed rods to return to their initial position automatically for reuse, indicating a considerable length of time and discontinuity between cycles. Additionally, their energy-absorbing design is an integrated structure that employs three distinct materials, which raises the system's complexity and cost.

2.3.3 Granular mechanical metamaterial

Three conceptual designs of multi-stable granular metamaterials that can dissipate energy through friction were developed by Kangjia Fu *et al*. (Figure 2.12) [89]. The first metamaterial unit cell comprises three rigid cylinders with an elastic band that wraps around cylinders. Seven spheres with elastic strings make up the second unit cell, and seven spheres with elastic membranes make up the third. When an external force is applied, the stretchy elements of the three concepts – the band, string, and membrane – can produce frictional energy dissipation between the rough surfaces of cylinders or spheres. The load-displacement curve exhibits hysteresis as a result of the input energy being partially released by friction between the spherical and cylindrical bodies with rough surfaces and partially trapped as elastic energy in the elastic components.

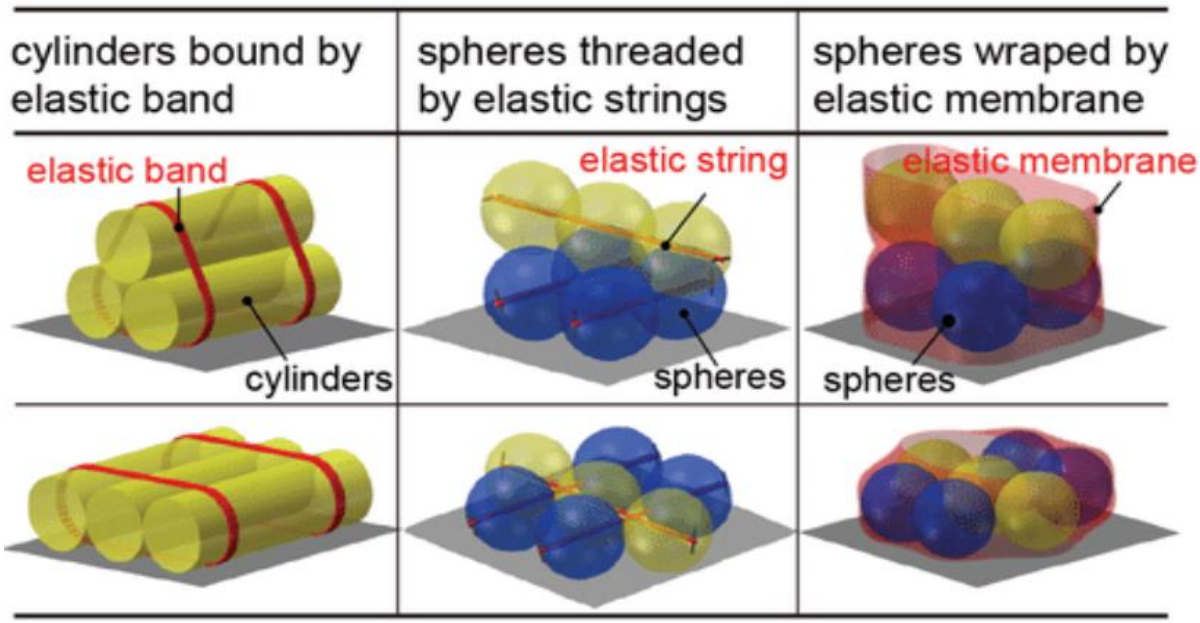

Figure 2.12. Three suggested concepts of multi-stable granular metamaterial unit cells by Kangjia Fu *et al* [89].

2.4 Types of Friction

Despite significant advances in the study of sliding friction and related phenomena after more

than a century, our fundamental knowledge of friction's origin remains incomplete, and a wealth of nontrivial physics remains unknown. Since this study sets friction as a major factor in generating energy dissipation, a general understanding of the friction phenomenon and the parameters that affect friction is needed prior to the design of the study process. These contents are mentioned in the following sub-sections.

2.4.1 Static friction

Static friction has traditionally been associated with adhesion and the breaking of bonds between atoms on opposing surfaces [90]. The tendency of unlike surfaces or particles to stick to one another is known as adhesion. Although surfaces may adhere, adherence is not equal to adhesion because molecular bonding is not required [90]. If material is cast between two surfaces and solidifies after penetrating and filling uneven spaces in the two surfaces, a network of interlocking "fingers" is formed, and there may be a strong mechanical union but no adhesion [91].

Figure 2.13 depicts the debate over two distinctly contradictory static friction mechanisms. At the above, the adhesive force maintains the surface together at the end of the unevenness and resists shearing movement. The bottom figure shows the situation where repulsive forces impede relative movement. This contradiction has reminded us of the fact that at least some of the fundamental physics of friction is still difficult to grasp.

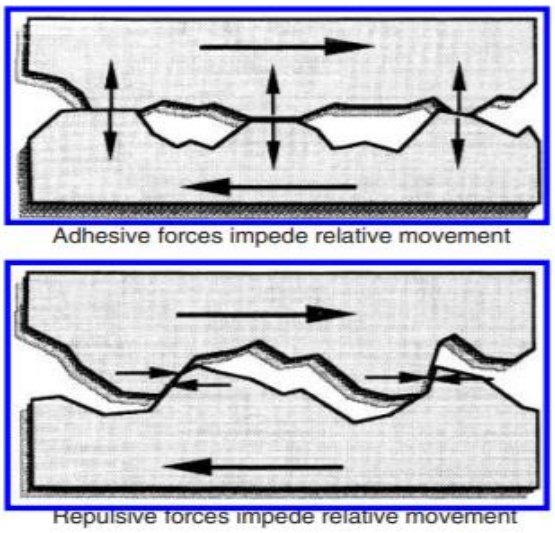

Figure 2.13. Proposal for two contradictory static friction mechanisms [90].

Thanks to the development of atomic force microscopy technology in the late 20th century, researchers were able to study and map the adhesion and lateral forces between surfaces at a molecular scale. The static friction force Fs has relied on the contact area A and the shear strength of the weaker material τ_m. Therefore, this relationship can be expressed by the following

Equation 2.10:

$$F_s = \mu_s * P^* = \tau_m A \tag{2.10}$$

μ_s is the static friction coefficient and P* indicates the normal force, which is equal to the total of the applied load and the adhesive force at the interface.

2.4.2 Sliding friction

In 1493, Leonardo da Vinci, a pioneer in tribology, developed the classic laws of sliding friction [92]. However, the laws detailed in his notebooks were never published and remained undiscovered. In 1699, Guillaume Amontons rediscovered these laws and they became known as Amonton's three laws of dry friction (Friction force is proportional to the normal load. Friction force is independent of the apparent contact area. Kinetic friction is independent of sliding speed. [93]. The third Amonton's law is also known as the Coulomb's law.

Figure 2.14 shows two objects in a sliding motion. The normal force, which can be denoted as N, is the perpendicular force pushing the upper block to the lower block's surface [90]. The block moves at a constant speed of v and encounters a friction force of F_k. Therefore, the equation of sliding friction (also known as kinetic friction) force is like the Equation 2.11 below:

$$F_k = \mu_k * N \tag{2.11}$$

where μ_k is the coefficient of sliding friction.

A complete understanding of sliding friction is still a difficult problem. This is because the more attention is paid to the details of the friction problem, the higher awareness of the fundamental complexity of the problem and the difficulty of predictive modelling [90]. For example, several early researchers had constructed friction models mainly based on the roughness of the two contact surfaces. Because the surface's topological qualities are unlikely to be the same, only the unique distribution of high points can be contacted at any one time. Thus, the surface area of block A which can be calculated by width times length will be larger than the actual contact area. Numerous attempts have been made to obtain the actual contact area, but the problem of obtaining the actual contact area has still not been solved because of physical limitations and controversial assumptions. The design that secures the maximum friction surface area, which is one of the design requirements of research, is not free from the above research gap.

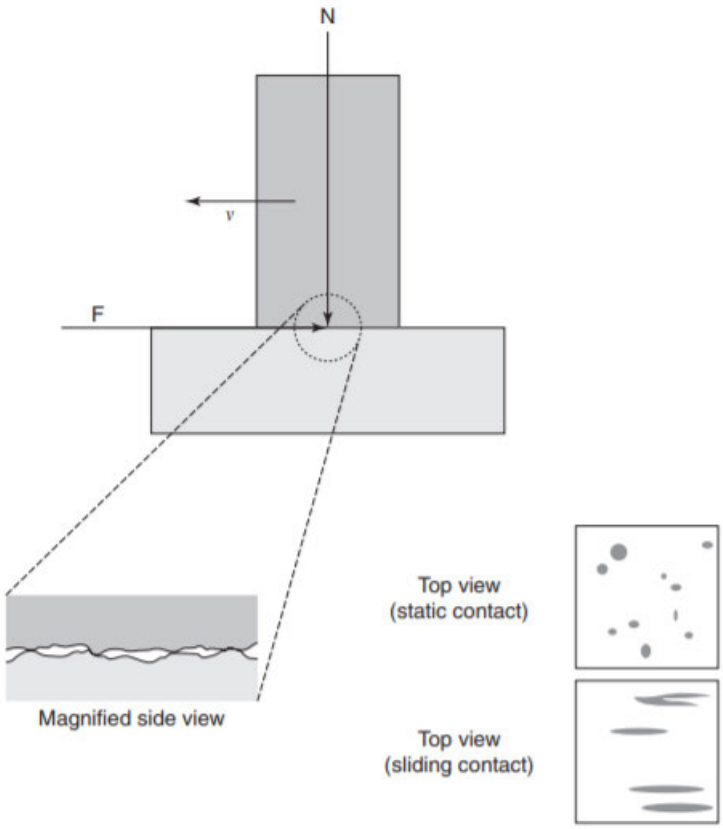

Figure 2.14. A simple model of sliding friction [90].

2.5 Frictional metasurfaces

The major known metasurfaces studies so far have been optical metasurfaces that regulate light properties such as phase, amplitude, and polarisation [94], electromagnetic metasurfaces for electromagnetic waves controlling [95], or acoustic metasurfaces to control sound wave propagation [96]. Although metasurfaces research for friction received little attention, frictional metasurfaces can be applied to shoe soles or gloves that require friction. Babaee *et al* have developed an optimal kirigami design that can control friction on various surfaces by evaluating the performance of dynamic kirigami soles via numerical simulations and friction tests [97]. They created a steel kirigami metasurface (Figure 2.15) that could be attached to the shoe sole, inspired by the cheetah's claws, the oxpecker's claws, and the snake's scales to enhance friction. The uniaxial response of the Kirigami structure was simulated using Abacus, and three participants were asked to walk the force plate in shoes with Kirigami metasurface to obtain walking experimental data. Their experiments showed that shoes with concave spike shape metasurfaces had more than twice the friction coefficient of ordinary commercial shoes and suggested the possibility of maximising energy dissipation through the design of appropriate friction surfaces. One weakness in their experiment was that when they selected the spike shape that made

up the Kirigami metasurface, they set only three-floor conditions (ice, vinyl, and wood) for measuring the coefficient of friction. They might have chosen a more reliable metasurface structure by conducting additional experiments based on floor conditions such as concrete and soil, which are conditions similar to common roads.

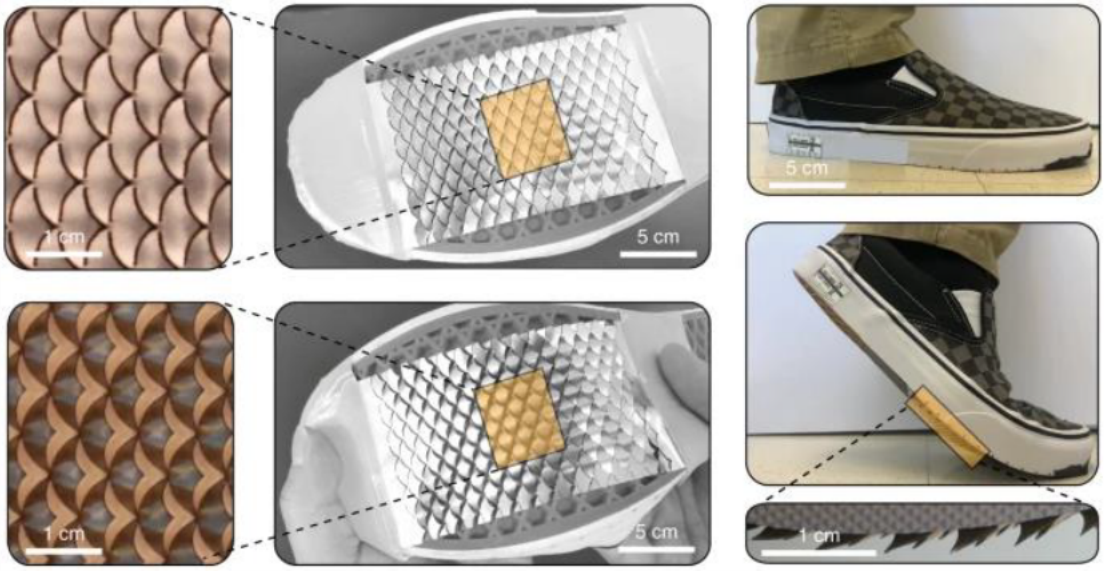

Figure 2.15. Non-slip kirigami metasurface shoe soles inspired by the animal's bodies [97].

2.6 Additive manufacturing (AM) technologies to create intricated structural metamaterials

Traditional manufacturing processes, such as machining and milling, were used to manufacture metamaterials on a bulk scale. Unfortunately, these technologies have some disadvantages in terms of relatively poor precision and complexity. Since its introduction in the late 20th century, 3D printing, also known as additive manufacturing technology has been steadily improving thanks to the ongoing efforts of several commercial companies and researchers and has been subdivided into distinguished manufacturing methods.

The 3D printing process starts by designing the part in computer-aided design (CAD) software, which is then exported to commercial slicer software to convert the file to G-code, where the geometry is sliced, print parameters are specified, and the G-code file is sent to the printer. Before the sliding process, some geometries that are not directly against the printing plate or have significant overhangs use support options to prevent them from printing improperly.

Since only metamaterials fabricated through Fused Deposition Modelling (FDM) method were used for compression experiments in this research, we will only briefly discuss FDM additive manufacturing method that was selected to carry out specimens fabrication.

2.6.1 Fused deposition modelling (FDM)

Fused deposition modelling (FDM), which is sometimes referred to as fused filament fabrication (FFF), is one of the most widely used 3D printing methods. It works on the principle of extruding a thermoplastic filament layer by layer to build a three-dimensional object. This additive manufacturing technology is well known for its simplicity, cost-effectiveness, and versatility. FDM can work with a wide range of thermoplastic materials, enabling users to select based on properties including strength, flexibility, and heat resistance. FDM allows to create fusible or detachable support structures, making it possible to print intricate geometries with ease. In addition, FDM printers are commonly less expensive than other 3D printing technologies, which is why they are readily available to educators, hobbyists, and small businesses.

Figure 2.16 describes the schematic diagram of the FDM machine [98]. A solid spool filament of thermoplastic material like thermoplastic polyurethane (TPU) or Acrylonitrile Butadiene Styrene (ABS), is fed into a heated nozzle. As the nozzle heats the filament to its melting point, the molten material is extruded onto the build platform in a controlled manner. The extruded material solidifies rapidly, layer by layer, to form the desired object. As each layer is completed, the build platform moves down, or the nozzle moves up.

FDM, despite having the advantage of being able to produce models at a relatively low cost, can be limited in its ability to achieve a high level of detail compared to other 3D printing methods. It also has the drawback that due to its layer-by-layer structure, layer lines may become visible on the surface of the printed object and may require post-processing for a smoother finish, making it a less likely choice for projects that require precise modelling.

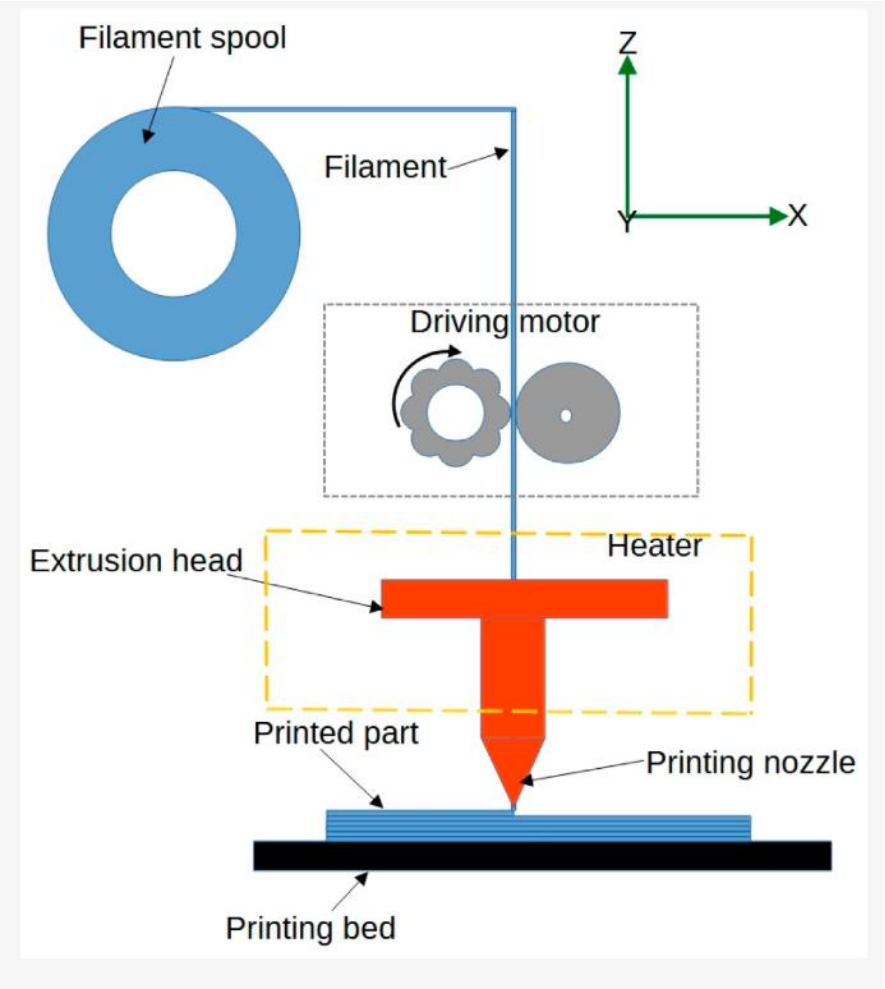

Figure 2.16. FDM printing system [98].

2.7 Basic theory to calculate energy absorption and dissipation

Frictional energy dissipation occurs when two surfaces rub against each other, where work is done against friction, and partially converted into heat at each surface. This heat represents the portion of input energy that is irreversibly dissipated. In contrast, the remaining portion of energy may be stored elastically or plastically within the internal structure of the material. Consequently, the overall energy absorption capacity corresponds to the sum of the dissipated energy and the stored internal energy, and is commonly evaluated as the area beneath the load-displacement curve, with the energy absorption capacity defined as the maximum energy stored and dissipated up to the failure point of the specimen [99]. This means the unloading curve is not required for calculating energy absorption. Figure 2.17 illustrates a simple example of a loading-unloading curve.

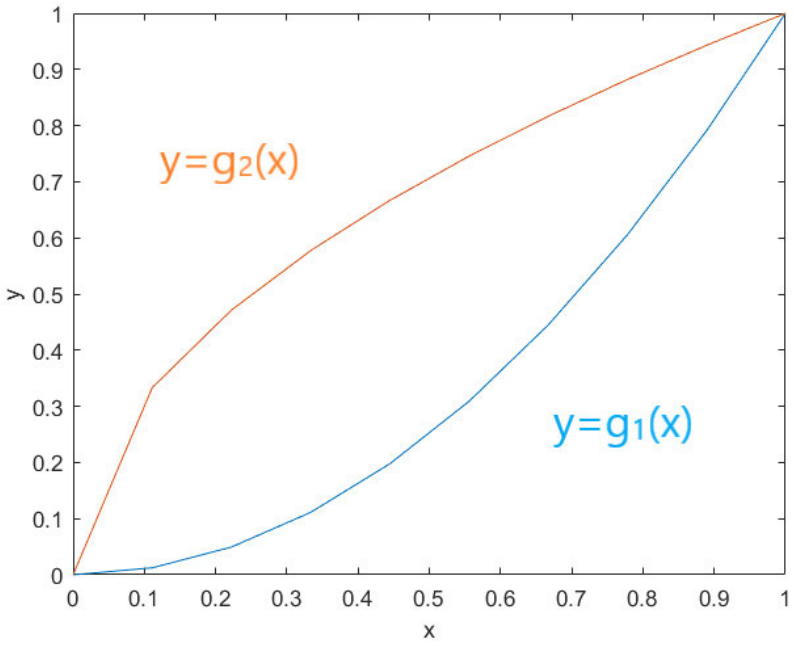

Figure 2.17. A simple example of a loading-unloading curve.

To calculate the dissipated energy, we can use Equation 2.12. The loading curve and unloading curve are denoted as g2(x) and g1(x) respectively. 'f' indicates the failure point.

$$E.D = \int_0^f (g2(x) - g1(x))\, dx \tag{2.12}$$

In the same way, Equation 2.13 for obtaining energy absorption can be set as follows.

$$E.A = \int_0^f g2(x)\, dx \tag{2.13}$$

From the above curve and equations, the following strategies can be proposed to maximise energy dissipation. Initially, find a way to increase the failure displacement point. When the loading curve is extended, it leads to more energy dissipation. However, in this research, we focus on the repeatable energy dissipation which is not allowed in the plastic deformation region. Therefore, instead of the failure point, trying to maximise the yield point is a more suitable aim. The other way is trying to rapidly reduce the gradient of the loading curve g2(x) and sharply increase the gradient of the unloading curve g1(x) to increase the area within the hysteresis loop.

CHAPTER 3: METAMATERIAL DESIGN, ANALYSIS AND TESTING

This chapter introduces the designed and fabricated frictional mechanical metamaterials to dissipate energy through frictional sliding on contacting surfaces located between internal columns. In addition, the description of the compression experiments as well as the finite element modelling used in this study are provided. Featuring unique internal structures, these metamaterials are able to achieve enhanced energy dissipation due to tribological interactions that result in contact and sliding mechanisms when subjected to an external force.

3.1 Metamaterial design

Solidworks 2023, a useful software widely known for its powerful features and user-friendly interface, was used to create the 3D computer-aided design (CAD) models that are essential for FE simulations. The initial step was to create the geometry of each component that comprise the frictional metamaterial. This process involved defining the shape and dimensions to ensure that the model accurately reflects the actual tribological physical properties. After modelling the distinct components, they were assembled to form the overall system. The final process to export the model in a format compatible with FEA software like ANSYS Workbench, which is going to be introduced later, was conducted. Solidworks's ability to integrate with simulation tools allowed to transfer the model seamlessly, maintaining geometric fidelity throughout the process. Prior to exporting the CAD files into ANSYS, they had to be saved in ICGS file format.

3.1.1 Geometries of the unit cell for metamaterials

The selection of the unit cell structure in this thesis was driven by the aim of developing a reusable friction-based mechanical metamaterial with enhanced energy dissipation per unit volume. Conventional frictional metamaterials often suffer from either limited contact area which leads to reduced dissipation, or irreversible deformation, preventing reusability. To address these limitations, a hexagonal frame was selected for their spring-like elastic response, while blade-type upper structures and tapered columns were incorporated to deliberately maximise internal contact surface area within a compact volume. By tailoring geometric parameters such as the angular difference between a pair of contact surfaces, the proposed structure allows tailoring of the contact pressure and frictional stress distribution across the sliding interfaces, as well as their evolution over the loading cycles. This tunability provides a flexible platform that can be adapted to represent a broader class of reusable frictional metamaterials. While this thesis focuses on demonstrating the feasibility of such control in a specific design, a more abstract formulation that generalises these principles could form the basis of future work.

The proposed unit cell in this study is composed of three distinct parts: a hexagonal elastic frame, either classic honeycomb (Figures 3.1g, h, i) or re-entrant (Figures 3.2a, b, c), the upper blade-like structure (Figures 3.1d, e, f) and four tapered pillars or columns (Figures 3.1a, b, c) in the lower one. This blade and column structure forms four pairs of contact surfaces to generate friction with the frame sidewalls acting akin to springs, storing energy through deformation upon loading and releasing it during unloading. It is important to note that this unit cell is intended to operate within the elastic range to ensure reusability. The presented columns design was finalised after a significant design development and optimisation process. Various design concepts and improvements to their performance were investigated to determine the shape of the proposed columns. The blades and columns were designed to maximise the contact surface area within a volume. The cross-sectional area of the four columns progressively reduces from the base to the top, with a cross-sectional shape that combines a quarter circle and a quarter circular spandrel. The blade shape matches the surface profile of the columns, and upon external loading comes into contact and then slides along the column to convert mechanical energy into heat. The detailed dimensions of each part of the unit cell are listed in Table 3.1.

The unit cell was designed to be manufactured in three separate 3D printed parts, and assembled to form a complete unit cell, as discussed in the next section. This approach allowed the gap between contact surfaces to be effectively set to practically zero, thereby achieving energy dissipation as soon as an external force is applied. This design also provides modularity, allowing different part combinations to be mixed and matched together and parts to be replaced when necessary.

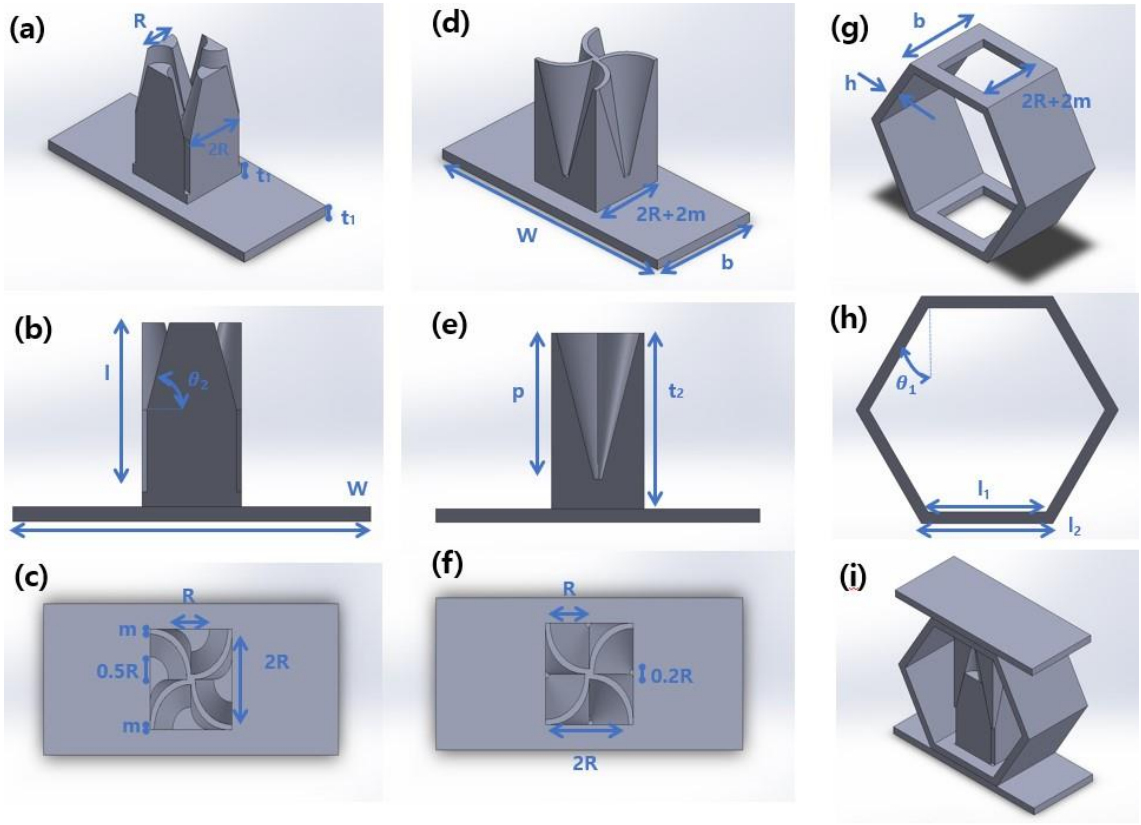

Figure 3.1. Various views (a, b, c) of the four columns part, (d, e, f) of the four-blade part, and (g, h) of the conventional hexagonal frame, and (i) complete unit cell appearance after assembling.

Table 3.1. The main dimensions of the hexagonal unit cell illustrated in Figure 3.1.

Dimensions of the unit cell												
b (mm)	h (mm)	Θ_1 (deg)	l_1 (mm)	l_2 (mm)	R (mm)	Θ_2 (deg)	l (mm)	p (mm)	t_1 (mm)	t_2 (mm)	m (mm)	W (mm)
30	3	30	30	33.46	9	75.58	34	31.5	3	38	1	70

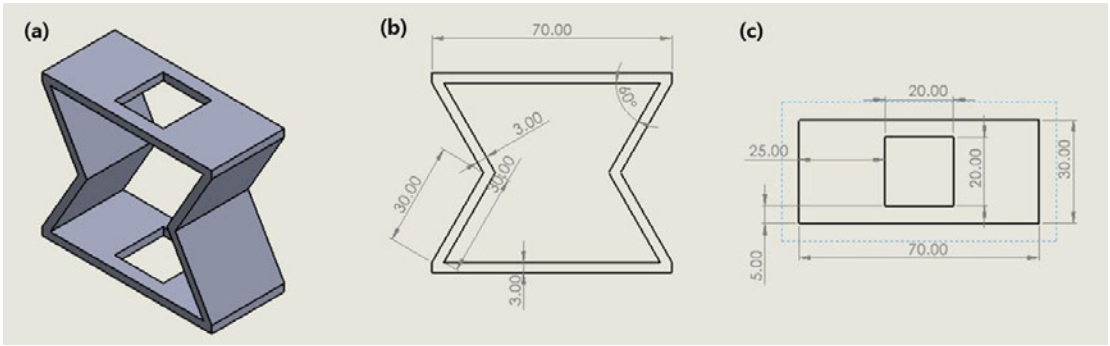

Figure 3.2. (a) Isometric view of the re-entrant hexagonal frame, (b) front view, and (c) top view.

3.2 Finite element methodology

Finite element (FE) simulations of the unit cell under compression were conducted using ANSYS Workbench 2023 R2 in this study. Finite element analysis (FEA) is a numerical technique for analysing the behaviour of structures or components under various boundary conditions like mechanical loading, fluid flow, or thermal changes.

3.2.1 FE simulations with unit cell geometries

Figures 3.3a and 3.3b illustrate the geometry of the conventional hexagon unit cell and re-entrant unit cell, respectively, as used for the FE simulations in Chapters 4 and 5.

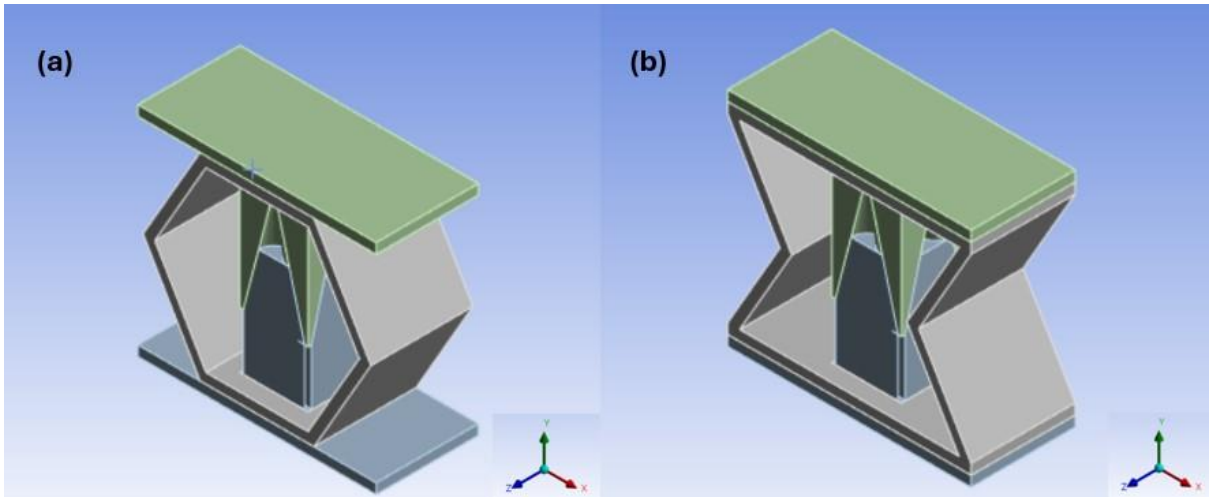

Figure 3.3. Imported geometries of (a) a conventional hexagonal unit cell, and (b) a re-entrant structural unit cell from Solidworks to ANSYS Workbench to run FE simulation. Each model was assembled from three individual bodies.

Quadratic element order is selected to correspond to complex geometries and bending deformations. The solid part and contact area of the model possess SOLID187 and CONTA174 elements, respectively. SOLID187 is defined by 10 nodes having three degrees of freedom at each node. CONTA174 is selected to describe contact and sliding between 3-dimensional target surfaces. As boundary conditions to perform the simulation, the bottom surface of the unit cell had been applied to the fixed support and the top surface had been selected to apply displacement condition.

When assembling the three parts that compose the unit cell, the contacts between the hexagonal frame structure and the other two parts were defined as bonded contacts. This choice reflects the tight fit between the frame and these other two parts that prevented them from separating or sliding against each other. In contrast, the contact surface pairs between the upper part with its blade structure and the bottom part with its four columns were configured as frictional contact.

Symmetric contact behaviour was specified since both sides were made of the same material, curved shapes that both possess the same proportion of angles, obviating the need to distinguish between contact and target surfaces.

The mesh quality on these frictional contact surfaces plays a crucial role in capturing accurate results related to energy dissipation. However, it is essential to strike a balance between accuracy and computational efficiency, as finer meshes come at the cost of increased memory usage and longer solve times. To find this balance, we conducted a mesh convergence study by varying the contact sizing resolution values within ANSYS Workbench (Appendix B).

Given the challenges in achieving a mesh convergence solution, we selected the augmented Lagrange formulation to address contact formation. Additionally, we enabled large deformation and the unsymmetric Newton-Raphson solver option to account for significant displacement and relatively high coefficients of friction.

Two types of materials were considered in the finite element simulations. CPE HG100, which was modelled as a linear elastic material, and TPU 95A, which was modelled as a hyperelastic and viscoelastic material. The detailed characterisation of these materials, including testing procedures and measured properties, is presented in Appendix A and Chapter 5.

3.2.2 Scaling from unit cell to metamaterial

The proposed hexagonal unit cell is intended to be used as a building block from which to construct energy dissipating metamaterials. Therefore, several finite metamaterials were assembled from the unit cells described in Section 3.1.1 to evaluate the influence of the change in boundary conditions and the interactions between unit cells. These metamaterials' energy dissipation performance was analysed through FE simulations that made use of the experimentally verified FE model of the unit cell. Because of the computational cost only a limited number of unit cells were considered, and the investigation focused on the trend in energy dissipation as the number of units increased. The load-displacement cycles and energy dissipation of these metamaterials were compared to that of a single unit cell subjected to the same compression cycle, with a peak effective strain of under 4.67%.

Metamaterials consisting of 8- and 13-unit cells were assembled into structures with the same height, but different widths as shown in Figures 3.4b and 3.4d. In order to achieve the same peak effective strain during the compression cycle, a total vertical compression of 1.5 mm was applied because the maximum height of the assembly is three times that of a single unit cell. To assess the sensitivity of its performance to the height-to-width ratio, an 11-unit cell model with 4 rows was also modelled, as shown in Figure 3.4c. A higher vertical compression of 2 mm was applied to this taller structure to achieve the same effective strain. These three assemblies represent steps in

the transition from single unit cell to metamaterial and provide insight into the relative influence of scale effects on performance. These proposed assembled geometries are just sample arrangements of multiple unit cells to investigate and present the performance and behaviour of the proposed design, and the proof of concept that the proposed frictional metamaterial offers effective energy dissipation. Due to the computational resource constraints, the number of unit cells composing the multi-unit cell structures was minimised in the FE simulation.

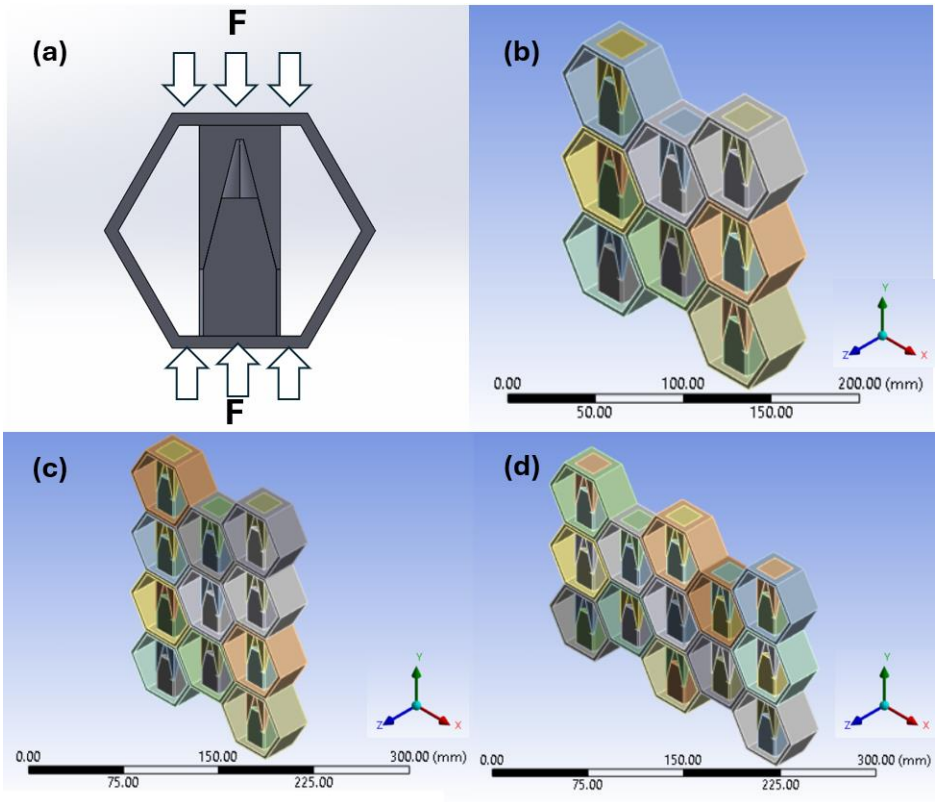

Figure 3.4. (a) Schematic diagram illustrating the external compression applied on a single unit cell, and finite metamaterials with (b) eight unit cells, (c) eleven unit cells and (d) thirteen unit cells. Note that in these simulations the wide loading plate parts at the top and bottom of the unit cell model was not present.

In order to more efficiently study the performance of periodic systems consisting of numerous unit cells a representative volume element (RVE) was defined as shown in Figure 3.5, to which periodic boundary conditions (PBCs) were then applied. Unlike the single-wall-thick hexagonal unit cell used in previous FEA simulations, in this RVE the frame sides are twice as thick as the thickness of a single unit cell hexagonal frame, except for the top and bottom sides. Since we are assuming a single hexagonal frame located in the centre of a structure made up of countless hexagons, the applied displacement boundary conditions are changed such that the top and bottom faces are subjected to half of the total displacement, directed towards the centre of the unit cell on each side, for both RVE and unit cell. This allows horizontal motion to occur as they are no

longer fixed in the test machine. Appropriate constraint equations set up to represent the PBCs are listed in Table S4 in Appendix D.

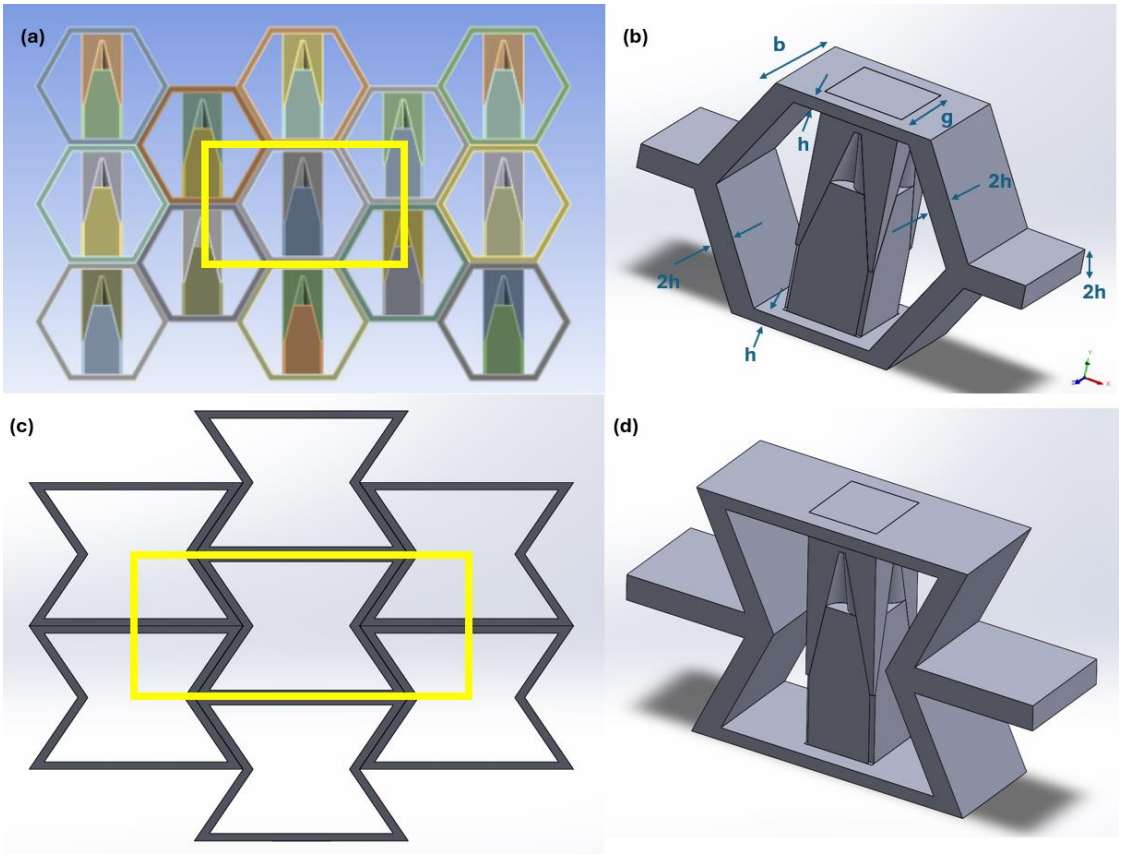

Figure 3.5. (a) RVE in a myriad hexagonal structure with internal structures for sliding (rectangular area in yellow). (b) A CAD model describing the RVE unit cell. The internal structures in the four corners of the yellow rectangle have been removed, as sliding is not expected with only partial bodies. Due to the nature of the RVE located in the middle of the repeating structure, the dimensions of the sides, except for the top and bottom walls of the central hexagonal frame, are twice the thickness of the sides of a single unit cell. (c) A re-entrant RVE (yellow rectangular area) in the centre of the structure formed by the assembly of multiple re-entrant structural frames. Each frame's internal structures for sliding are omitted. (d) A re-entrant RVE cell model assembled with internal bodies.

3.3 Materials and fabrication

While several fabrication methods could in principle be used to manufacture the unit cell test articles such as moulding or casting which may be more cost-effective for volume production, additive manufacturing was selected in this study. The choice was motivated by its ability to rapidly prototype complex geometries, enable internal interfaces that would be difficult to realise using traditional methods, and avoid the additional time and expense of producing dedicated tooling. Moreover, the aim of this work was to investigate the fundamental mechanics of the proposed structures rather than to optimise for mass manufacturability, making 3D printing the

most suitable approach.

3.3.1 Linear elastic test article

All unit cell parts were 3D printed by fused deposition modelling (FDM) using a Caribou MK3S 320 with Filamentum CPE HG100 as the constituent material. CPE, also known as PET (polyethylene terephthalate), stands out as a robust and durable filament that is characterised by robust interlayer adhesion. The CPE filament was selected over more common filaments such as ABS owing to its reduced warping tendency strong interlayer adhesion, and superior dimensional stability. These characteristics are critical for reliably achieving the precisely designed internal contact surfaces of the proposed unit cell. The 3D printer's nozzle temperature was set to 270℃ and the bed temperature to 80℃, in accordance with the filament supplier's recommendations. The infill value was set to 50% to balance manufacturing time, material usage, and mechanical strength of the printed parts.

As shown in Figures 3.1g and 3.2a, the hexagonal frame has rectangular openings in its upper and lower base sides that are required for assembly. This necessitated the addition of support during printing. Scarring from support removal was minimised by selecting the support material style as "Snug", which also conserved filament. Given the nature of the FDM process, the strength of the resulting structures will vary depending on the direction of external loading relative to the orientation of the filaments and layers from which the part is constructed. To enhance the strength of the unit cell's frame under vertical forces, this part was manufactured such that the hexagonal shape was in the printer bed plane and filament ran along the perimeter of the hexagon. Although alternative additive manufacturing techniques such as SLA or SLS are known to exhibit weaker anisotropy, the present study was constrained to FDM fabrication due to limited access to such equipment. Accordingly, the printing direction was carefully selected to minimise fabrication induced performance variability and to ensure that the as printed behaviour represents the intended design response.

Once all three parts had been 3D printed, the unit cells were manually assembled by pushing the upper blade and lower columns through the openings in the frame until they came into contact, resulting in four of each of the test articles illustrated in Figure 3.6.

To characterise the as-printed compression properties of CPE HG100, five cylindrical test specimens were printed in addition to the unit cell test article parts. These cylindrical specimens had a diameter that was equal to their height of 20 mm (Appendix A). To characterise its frictional properties of this material, two kinds of rectangular block specimens were also printed.

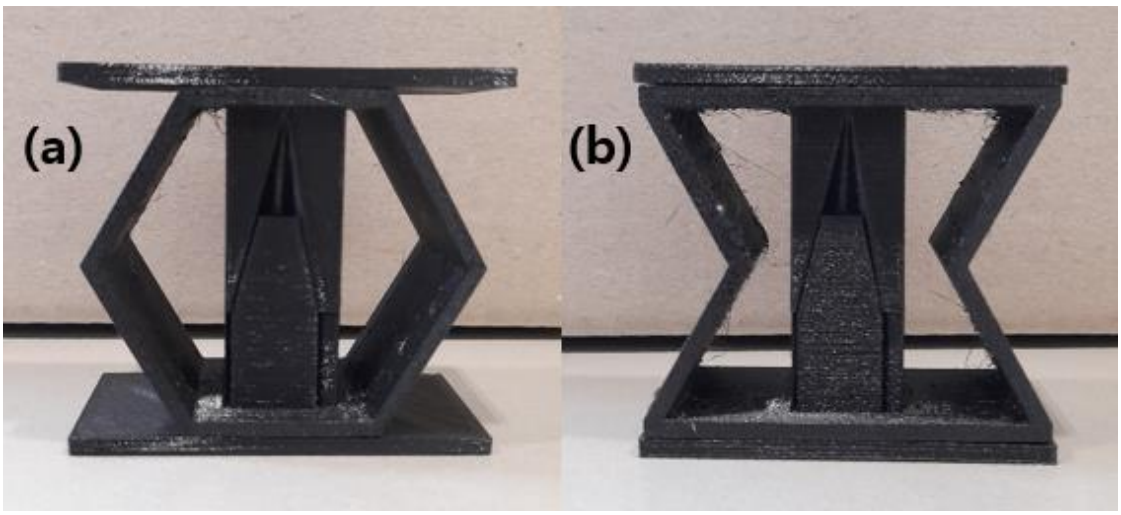

Figure 3.6. Unit cells additively manufactured by FDM with (a) a conventional hexagonal frame and (b) a re-entrant frame.

3.3.2 Hyperelastic test article

Like in Section 3.3.1, fused deposition modelling (FDM) is selected as a 3D printing method in this study through a Caribou MK3S 320 with Filamentum TPU 95A which is the constituent substance of the unit cells and cylinder-shaped specimens. In general, thermoplastic polyurethane elastomer (TPU), and especially TPU 95A grade, is well known for its desirable material properties such as good flexibility, tensile strength, and outstanding abrasion resistance. In addition, it shows off a high toughness and impact resistance as well as durability. These mechanical properties enable this material to be used in a variety of applications, including medical prostheses, conveying pipelines, sporting products, machinery, and automobiles. The nozzle temperature of the 3D printer was set to 230 ℃ and the bed temperature to 50 ℃, as recommended by the filament supplier. The infill value was set to 50 % to achieve a balance of manufacturing time, material usage, and mechanical strength of the printed parts. Figure 3.7 depicts both different structures unit cells created by manually assembling the three individual parts produced by FDM additive manufacturing.

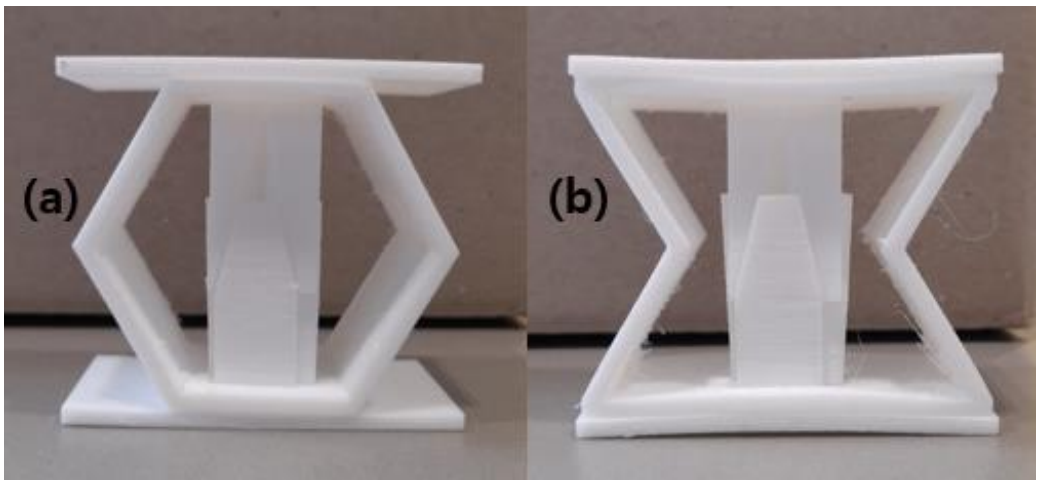

Figure 3.7. TPU 95A unit cell models: (a) conventional hexagon and (b) re-entrant structure fabricated by FDM.

3.4 Compression experiments

3.4.1 Coefficient of friction measurement

The Coefficient of Friction (CoF) between the two 3D-printed CPE HG100 surfaces and between the two TPU 95A surfaces was measured with a linear reciprocating tribometer (DUCOM, model: TR-282) using a pin-on-plate set-up with a 6 mm diameter pin. The tests were conducted under 30 N applied load and 2 Hz sliding frequency for 30 minutes at room temperature (22°C) and under dry contact condition. Winducom software was used for recording the frictional forces and the CoF. The test samples exhibited good wear resistance, and a consistently stable CoF was obtained. The average CoF for CPE HG100 and TPU 95A was recorded as 0.547 and 0.738, respectively.

3.4.2 Compression Test

The fabricated unit cells and cylindrical-shape material characterisation specimens underwent quasi-static compression testing in a Tinius Olsen H10K-S universal testing machine (Serial No.0162) with a Hounsfield 10 KN load cell (Serial No.703053). All compression tests were conducted under displacement control at room temperature, without any heating or cooling, using a compression speed of 3 mm/min.

In Chapter 4 for CPE HG100 models, each unit cell test was repeated at least three times under three distinct displacement conditions: 1 mm, 2 mm, and 3 mm. In Chapter 5 for TPU 95A models, each compression test with unit cell models has been repeated three times under the same 1 mm, 2 mm, and 3 mm displacement conditions. For the cylindrical specimen to measure material properties of TPU 95A, compression tests were performed under displacements of 8 mm, 10 mm,

and 12 mm corresponding to 40%, 50%, and 60% of the specimen height, respectively, considering the expression of nonlinearity in high strain (see Appendix F). In Chapter 6, as a slight variation found in this chapter, each unit cell compression test was repeated three times at each of the three displacement conditions: 1 mm, 2 mm, and 2.5 mm. Owing to the designed metasurface specimens showed permanent deformation at displacements greater than 2.8 mm, requiring a slight adjustment to the maximum displacement value to maintain the elastic deformation category.

Figure 3.8a illustrates an abstract depiction of applying compression to a unit cell model, while Figure 3.8b captures the actual compression experimental setup. The height of the unit cell specimens measured every time before the tests to obtain consistency of results by matching the same pre-experimental height. During the assembly of the individual additively manufactured components into a unit cell, especially those made of TPU 95A, applying excessive pressure can cause adhesion between contact surfaces and also make it difficult to maintain unit cell height constancy prior to compression testing. Therefore, for physical unit cells manufactured with TPU 95A, the total unit cell height of 64.8 mm is targeted for unit cell assembly, which is approximately 1.2 % higher than the total height of the CAD model.

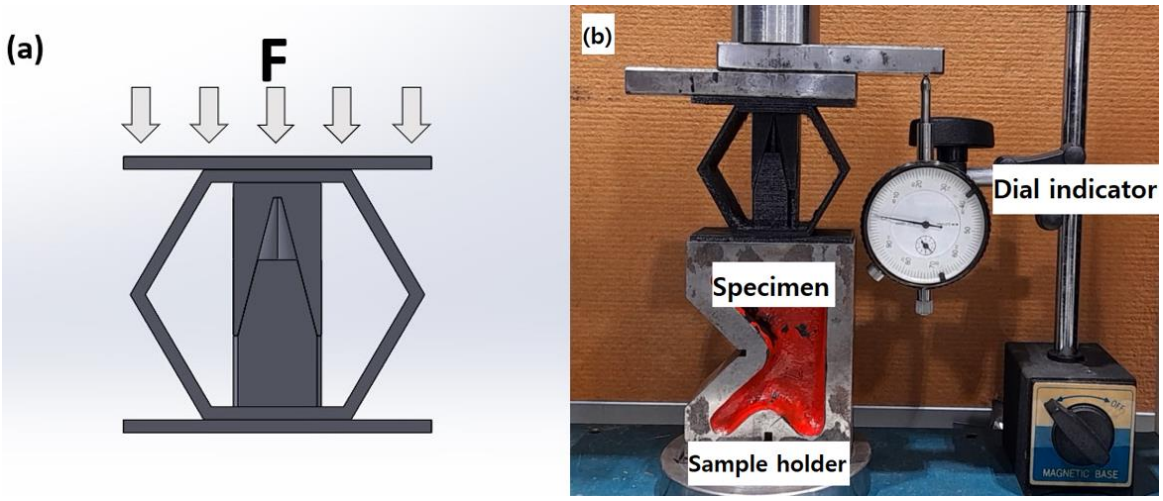

Figure 3.8. (a) Schematic diagram for describing the compressive load applied to the unit cell and (b) image of the uniaxial compression test setup.

3.5 Conclusion

This chapter introduced the geometry of the unit cell specimens that will be covered in later chapters and also showed how the specimens were manufactured. There was also a concise description of the FE simulation, and the compression experimental methodologies used in the chapters that follow. The specimens were fabricated by joining three parts together through an assembly process. The geometries of these parts were saved as Solidworks CAD model files in

STL format and converted to G-code using PrusaSlicer to make them 3D printable. Two filament materials, CPE HG100 and TPU 95A, were employed for specimen fabrication. CPE HG100 was selected for its relatively stiff and elastic properties, which enable the unit cells to withstand repeated compressive loading within the elastic deformation range. On the other hand, TPU 95A was chosen for its soft, hyperelastic, and viscoelastic properties, which allow for the investigation of energy dissipation in compliant structures. The combination of these two materials provides a comprehensive understanding of the mechanical behaviour of friction metamaterials across different stiffness regimes.

CHAPTER 4: ENERGY DISSIPATION IN A LINEAR ELASTIC METAMATERIAL

In this chapter, the geometry of the novel frictional mechanical metamaterial introduced in Chapter 3, consisting of a central hexagon or re-entrant honeycomb frame, a lower section with four tapered columns, and an upper portion with a blade shape, is validated through theory, simulation, and experiment. When subjected to an external uniaxial force, the three-dimensional structure of the metamaterial utilises sliding interactions to dissipate frictional energy. The mechanical properties of the proposed metamaterial, such as load-displacement relationships, hysteresis area, and peak force, can be fine-tuned by adjusting geometric parameters and constituent materials. Extensive analysis was conducted through experimental compression tests, finite element simulations, and theoretical modelling. Comparative assessments of the metamaterial's energy dissipation performance demonstrated a good agreement between experimental and simulation results, with minor variations observed for deeper compression cycles. The proposed metamaterial offers the potential for superior elastic energy absorption and dissipation, making it a promising solution for applications requiring repeated energy dissipation or damping under cyclical loads while maintaining a lightweight profile.

4.1. Introduction

Various geometric designs can produce different levels of energy dissipation and absorption to mitigate external shocks and protect the core components of machines, buildings, and even human beings. Energy dissipation structures, including dampers [62, 100, 101], and anti-seismic buildings [102, 103], are essential, particularly in regions located on tectonic plate boundaries. In industries like aerospace and automotive, the need for effective braking systems and energy dissipation is paramount to ensure the safety of passengers and crucial components during impact events [104-106]. Structures designed for efficient energy absorption and dissipation play a vital role in protecting lives and valuable assets from unforeseen impacts.

To enhance the performance of energy dissipation and absorption, researchers have consistently explored unique geometric structures, drawing inspiration from both human intuition and nature's intricate designs, such as the beetle forewing [107], woodpecker's beak [108], and the mesocarp layer of a pomelo fruit [109]. The pursuit of novel geometry has led to increased structural complexity, making the manufacture of prototype specimens challenging. The advances in 3D printing, since its invention by Chuck Hull in 1983 [110], have been crucial for experimentally validating the performance of the designed frictional metamaterials in this study.

Metamaterials, characterised by unique properties not found in natural monolithic materials [111],

have opened up new avenues in various fields, including negative Poisson's ratio [24, 112], cloaking [113, 114], and high energy absorption [63]. Over the past two decades, engineers have created various metamaterials with applications in acoustics, thermodynamics, electromagnetics, and mechanics, leading to innovations like invisibility cloaks and superior energy absorbers.

Multiple methods for absorbing and dissipating mechanical energy through metamaterials have been explored. Prototypes in the form of lattice struts, for instance, achieve substantial energy absorption by deforming and breaking the internal lattice structure upon external impact [115]. Sandwich panels, with enhanced lattice structures in the centre, aim to exploit the plastic deformation of the lattice [116]. Origami or kirigami patterns applied to metamaterial geometry enable directional fracture, optimising energy absorption [57]. However, these methods often result in irreversible processes and cannot be reused after energy-dissipating operations.

The need for reversibility, i.e. reusability, together with high energy absorption has led to several novel concepts being proposed over the last five years. One approach involves granular metamaterials with reversible hysteresis, combining rigid cylinders with flexible, stretchable elements. This novel metamaterial maintains structural integrity through stretchable elements while dissipating frictional energy during cylinder sliding, akin to bistable metamaterials [89]. Another concept based on frictional energy dissipation employs a honeycomb structure, where each cell contains a frictional mechanism that consists of beams whose tips slide along an inclined surface when the honeycomb cell undergoes in-plane compression [85]. This metamaterial generates a significant hysteresis area and the proposed 2D structure can be expanded into 3D to further improve performance.

Multistable metamaterials that can switch between multiple stable states due to their reversibility dissipate energy when changing states and offer reusability within the range of elastic deformation [117]. One limitation is that they require additional manual intervention to return to their original state. Yet another concept that has been proposed is that of "intertwined structures". This metamaterial consists of three key components: a soft elastomer, a stiff frame, and steel rods, interacting to absorb energy as rods pass into elastomer holes when subjected to external force [88]. More recently, energy-absorbing metamaterials with multilayered chiral topologies have been presented. The energy dissipation occurring at the interface between adjacent discs comprising the metamaterial enables the metamaterial to self-repair, making it reusable [118]. In addition, it has been demonstrated that mechanical metamaterials with negative Poisson's ratios, known as auxetics, provide benefits in impact protection [119] and improved fracture resistance [120]. However, a metamaterial combining the concept of friction with the re-entrant structure topology, which is one of those that exhibit a negative Poisson's ratio, has not yet been investigated.

Here we present a new reusable three-dimensional frictional metamaterial unit cell in which multiple pillars slide along curved surfaces when an external force compresses the unit cell, inducing friction and enhanced energy dissipation density. This proposed concept is different from conventional shock absorbers, which focus on energy absorption at high strain rates. Both auxetic and non-auxetic versions of this unit cell are formulated. A theoretical model and a finite element analysis methodology are developed to analyse the unit cell's load-displacement response and derive its energy dissipation. To demonstrate the supposed new design concept of metamaterials, we validated the conventional hexagonal single unit cell geometry by comparing FE simulation with experiments and then presented several simple arrangements of this unit cell. The conventional and auxetic versions of the unit cell are fabricated by a polymeric additive manufacturing process and demonstrate experimentally that the predicted performance can be achieved under various levels of compression. These designed structures are intended to work at small strain regime to avoid plastic deformation. In addition, there is no consideration of lubrication to maximise energy dissipation through friction. Interestingly, it is found that the experimentally measured performance is somewhat better than predicted and that the auxetic unit cells dissipate only a little more energy. The finite element simulation methodology is then applied to assemblies with different numbers of unit cells, i.e. finite metamaterials. This analysis indicates that only a moderate number of such cells is needed to estimate the performance of larger frictional metamaterial domains.

4.2. Method

The simulation and experimental models were presented in the previous chapter. In this section, the developed theoretical model is discussed in detail.

4.2.1 Theoretical model

For the model proposed in this study the work done not only by sliding friction of internal contact surfaces but also by the elastic deformation of the contact surface support structure and hexagonal frame should be taken into account for calculating total work when the proposed unit cell is compressed as shown in Figure 3.8 [85]. In mechanical systems, the work done by a force is defined as the dot product of the force vector and the displacement vector, which captures the component of the force in the direction of motion [121]. Because the dot product is additive, the total work done by multiple forces can be obtained by summing the contributions from each force along its respective displacement. This additive property allows the total energy in the system to be expressed as the sum of individual contributions, as shown in the following theoretical formulation.

$$W_{novel} = \int \vec{F} \bullet d\vec{r} = \int \left(\vec{F}_{honeycomb} + \vec{F}_{bending} + \vec{F}_{sliding}\right) \bullet d\vec{r} \tag{4.1}$$
$$= \int \vec{F}_{honeycomb} \bullet d\vec{r} + \int \vec{F}_{bending} \bullet d\vec{r} + \int \vec{F}_{sliding} \bullet d\vec{r}$$

Therefore, a simpler representation of the total work of the proposed frictional mechanical metamaterial is:

$$W_{novel} = W_{honeycomb} + W_{bending} + W_{sliding} \tag{4.2}$$

where $W_{honeycomb} = \int \vec{F}_{honeycomb} \bullet d\vec{r}$, $W_{bending} = \int \vec{F}_{bending} \bullet d\vec{r}$, and $W_{sliding} = \int \vec{F}_{sliding} \bullet d\vec{r}$

$W_{honeycomb}$, $W_{bending}$, and $W_{sliding}$ refer to the bending work of the outer walls of the hexagonal central frame, the bending work of the four internal columns, and the frictional work generated by sliding between the internal contact surfaces, respectively. Since the force varies continuously with displacement, each equation is expressed in integral form. $\vec{F}$ denotes the force vector acting on the outer walls, columns, or contact surfaces of the unit cell during deformation, while $d\vec{r}$ is the infinitesimal displacement vector corresponding to the actual deformation path.

Based on the assumption of quasi-static loading, frictional heating and the associated temperature changes in the unit cell are not a consideration and thus thermal energy flow can be neglected. Therefore, the total energy absorbed in the metamaterial unit cell is the sum of the work done in all the elastic deformations and frictional sliding. The following formulations of expressions for each of these work terms in Equation 4.2 are based on simplifying assumptions that may not capture the full complexity of the kinematics of the frame, blades and columns, but they provide a simple approach to estimating the total mechanical energy absorbed by the unit cell during the compression loading phase.

A honeycomb unit cell with a geometry similar to that of the hexagonal frame in the proposed frictional metamaterial unit cell had been studied by Gibson [122]. When the honeycomb cell deformation under load is dominated by sidewall bending, the applied displacement δ can be calculated by Equation 4.3.

$$\delta = \frac{F * L^3 * sin(\theta_1)}{12 * E * I_{honeycomb}} \tag{4.3}$$

where F is the applied external force on the unit cell, E is the Young's Modulus of the constituent material, θ_1 is the angle between the unit cell's sidewall and the longitudinal axis.

(Figure 3.1h) and $I_{honeycomb}$ is the moment of inertia of the frame sidewall's rectangular cross-section.

$$I_{honeycomb} = \frac{b * h^3}{12} \tag{4.4}$$

Here, *b* is the extruded length of the unit cell and *h* is the wall thickness of the unit cell. The side wall length *L* is defined as:

$$L = \frac{l_1 + l_2}{2} \tag{4.5}$$

where l_1 and l_2 are the inner and outer side lengths respectively. The applied force required to obtain a certain displacement can then be calculated by substituting for $I_{honeycomb}$ and *L* and rearranging Equation.4.3

$$F = \frac{E * b * h^3 * \delta}{L^3 * sin^2(\theta_1)} \tag{4.6}$$

Then the work of a cell deformation can be calculated by multiplying the force by deflection as below:

$$W_{honeycomb} = \int_0^{\delta} F \, d\delta' = \frac{E * b * h^3 * \delta^2}{L^3 * sin^2(\theta_1) * 2} \tag{4.7}$$

The four internal vertical columns can be split into two parts – the same cross-section area part from the base to the around intermediate section part and a not uniform cross-section area part from the middle section to the top of the columns. The part directly related to bending is the column part with a uniform cross-sectional area, so the deflection of each of the columns on the base of the unit cell due to bending can be expressed using the following Equation 4.8 adapted from Ref. [123]:

$$\delta_{bending} = \frac{F_{bending} * l^3}{3 * E * I_{column}} \tag{4.8}$$

where $F_{bending}$ is the force applied at the free end of the column and l is the length of the column.

The cross-sectional shape of each column for friction can be divided into two parts, a quarter circle and a quarter circular spandrel (Figure 4.1), each of which has a different equation to calculate the moment of inertia. Therefore, the moment of each part should be calculated

separately, and the use parallel axis theorem to calculate the whole moment of inertia.

The moment of inertia of each part concerning the $X^{`}$ axis can be obtained using the following Equation 4.9 adapted from Ref. [124]:

$$I_{columnX} = \sum(I + Ad^2) = I_1 + A_1 d_{y1}^2 + I_2 + A_2 d_{y2}^2 \quad (4.9)$$

Same way, the moment of inertia of each part with respect to the $Y^{`}$ axis can be expressed as:

$$I_{columnY} = \sum(I + Ad^2) = I_1 + A_1 d_{x1}^2 + I_2 + A_2 d_{x2}^2 \quad (4.10)$$

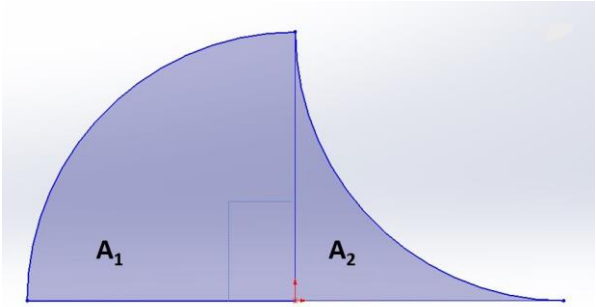

Figure 4.1. Cross-section of each column divided into two areas. A_1 is the quarter circle part and A_2 is the quarter circular spandrel part.

The columns are not directly constrained by explicit boundary conditions but are instead influenced by the overall boundary conditions of the hexagonal unit cell. This approach ensures that the internal interactions and deformations of the columns reflect the realistic loading conditions applied to the entire unit cell.

The maximum moment of inertia I_{column} is selected to maximise the bending force ($F_{bending}$) and then Equation 4.8 can be rearranged and when multiplied by the deflection gives the work of the bending force as:

$$W_{bending} = \int_0^{\delta} F_{bending}\, d\delta' * 4 = \frac{\delta_{bending}^2 * 3 * E * I_{column}}{2 * l^3} * 4 \quad (4.11)$$

The multiplication by 4 at the back reflects the presence of 4 tapered columns inside the unit cell. The amount of work by sliding, also known as frictional energy dissipation, can be calculated by multiplying the normal force on the contact surface by the coefficient of friction (μ) and the sliding distance ($\delta_{sliding}$):

$$W_{sliding} = \mu * N * \delta_{sliding} \tag{4.12}$$

The normal force *N* on the contact surfaces and the sliding distance can be expressed as:

$$N = \frac{F_{bending}}{cos\ (\theta_2)} \tag{4.13}$$

$$\delta_{sliding} = \frac{\delta}{sin\ (\theta_2)} \tag{4.14}$$

Bending displacement can be obtained from the applied displacement δ in Equation. 4.3:

$$\delta_{bending} = \frac{\delta}{tan\ (\theta_2)} \tag{4.15}$$

Substituting Equations 4.11, 4.13, 4.14 and 4.15 into Equation 4.12 we arrive at the work by sliding:

$$W_{sliding} = \frac{\mu * 3 * E * I_{Column} * \delta^2}{l^3 * cos(\theta_2) * sin(\theta_2) * tan\ (\theta_2)} * 4 \tag{4.16}$$

The multiplication by 4 at the back reflects the presence of 4 pairs of contact surfaces from the four columns. The proposed new unit cell consists of a hexagonal frame with four inner columns for sliding friction and bending. Therefore, the total work quantity would be denoted as:

$$W_{novel} = \frac{E * b * h^3 * \delta^2}{L^3 * sin^2(\theta_1) * 2} + \frac{\delta_{bending}^2 * 6 * E * I_{column}}{l^3} + \frac{\mu * 3 * E * I_{column} * \delta^2 * 4}{l^3 * cos(\theta_2) * sin(\theta_2) * tan\ (\theta_2)} \tag{4.17}$$

Equation 4.17 includes all three factors - $W_{honeycomb}$, $W_{bending}$, and $W_{sliding}$ - indicates the energy absorption of the unit cell. The $W_{honeycomb}$ and $W_{bending}$ are related to elastic energy storage, while the $W_{sliding}$, referring to frictional sliding, which contributes directly to energy dissipation. We calculated the energy dissipation of the proposed structure using only $W_{sliding}$, as well as the overall energy absorption capacity by adding all three terms of work presented in Equation 4.17. These theoretical results are compared with the hysteresis loop areas obtained from the experiments and FE models (Figure 4.5, and Table 4.1).

4.3. Results

Figures 4.2(a-c) illustrate the deformed and undeformed forms of the proposed unit cell. Figure

4.2a shows the situation immediately after the end of the unloading step of the unit cell, Figure 4.2b depicts the deformed unit cell in the vertical direction (y-axis) immediately after the end of the loading step, and Figure 4.2c displays the deformed unit cell in the lateral direction (x-axis) immediately after the end of the loading step. To explicitly represent the deforming shape, an x3.2 scale factor has been applied. It is notable in Figure 4.2a that the displacements of the columns inside the unit cell do not return to zero completely at the end of unloading. In the case of Figure 4.2b, the displacement is expressed as a negative value because the direction of the external force from the top of the unit cell downwards is opposite to the y-axis of the coordinate system. For Figure 4.2c, the displacement values are represented as positive for the left side and negative for the right side because the direction of lateral displacement of the left and right sides is opposite to each other. Both Figure 4.2b and Figure 4.2c show the deformation for a displacement of 3 mm from the top of the unit cell to the bottom (in the direction of the negative y-axis), which is somewhat exaggerated due to the auto-scale factor of 2.

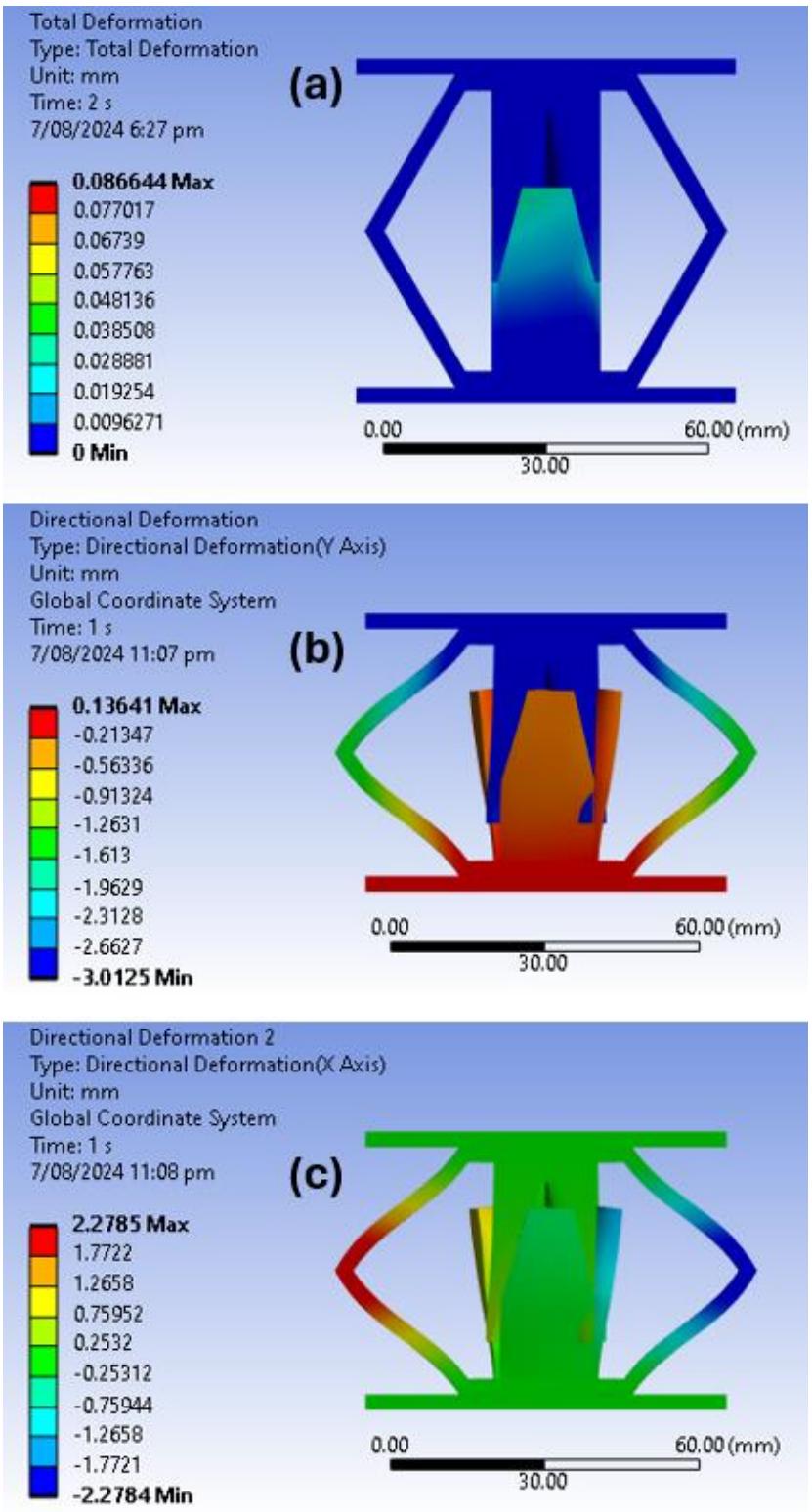

Figure 4.2. Displacement contour plots for the unit cell in three states: (a) total deformation at the end of the unloading step, (b) vertical deformation at the end of the loading step, (c) horizontal deformation at the end of the loading step. These deformations have been scaled up to more clearly show the deformed shape. These profiles are extracted from the FE simulation for an applied compressive displacement of 3 mm (see curve labelled FEA 3 in Figure 4.4c).

The frictional stress contour plot on the contact surfaces of the geometry in the FE simulations is also generated as a typical example to show a stress distribution. One of the contact surfaces located on the four columns is point-symmetric through the centre point of the unit cell and therefore exhibits the same frictional stress distribution for every column. The result indicates that significant stress concentrations are present at the bottom edges of these contact surfaces at the end of the loading step (Figure 4.3).

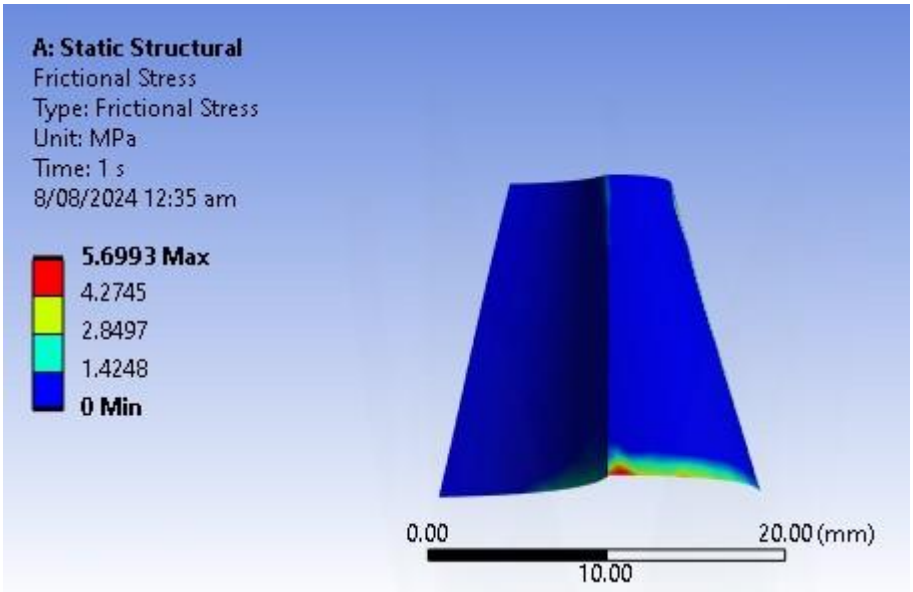

Figure 4.3. Frictional stress distribution on one of the four identical contact surfaces of the unit cell model at the end of the loading step for the same compression condition as shown in Figure 4.2.

The graphs in Figures 4.4(a-c) depict the hysteresis loops obtained from experiments with maximum vertical compression displacements of 1, 2, and 3 mm, respectively, and the FE simulations of these load cycles for the conventional hexagonal unit cell. When the conventional hexagonal frame is replaced with a re-entrant frame, the resulting experimental and simulated hysteresis loops under the same load cycles are plotted in Figures 4.4(d-f). These cycles are expressed in terms of effective stress and strain in Figure 4.4 as the unit cell is intended to be the building block of an architected material. The effective stress and strain are converted from the test and FE force and displacement results by dividing the displacement by the height of the unit cell and the load by the cross-sectional area of the unit cell, respectively. The height of the assembled single unit cell is around 64 mm, and the cross-sectional area could be obtained by dividing the cell's height from the total volume of the unit cell.

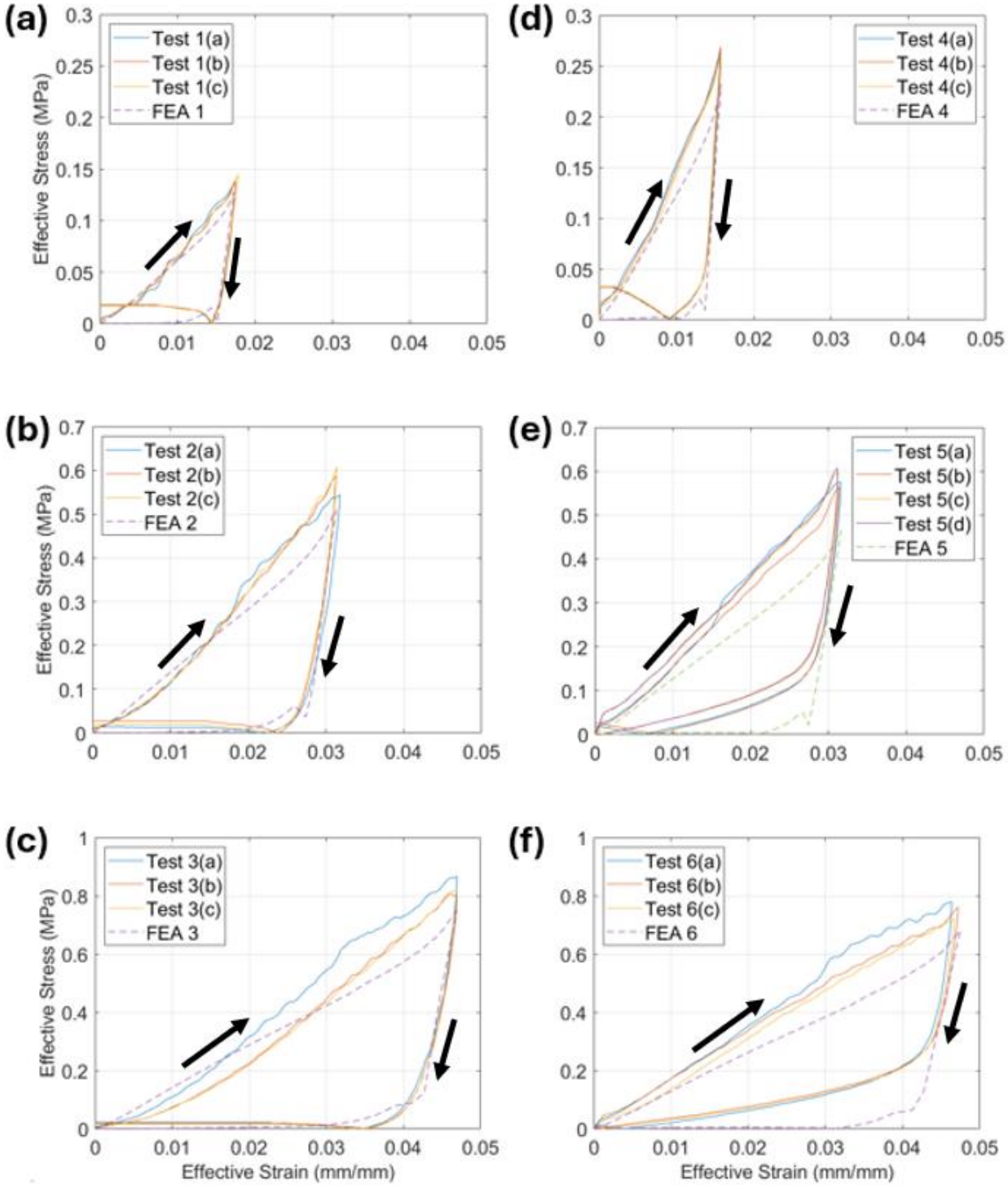

Figure 4.4. Effective stress-strain results from compression tests and FE simulations for (a) 1 mm displacement cycle (1.56% maximum strain), (b) 2 mm displacement cycle (3.1% maximum strain) and (c) 3 mm displacement cycle (4.67% maximum strain) applied to a unit cell with a conventional hexagonal frame; and equivalent results for (d) 1 mm displacement cycle, (e) 2 mm displacement cycle and (f) 3 mm displacement cycle applied to a unit cell with a re-entrant hexagonal frame.

The compression test results in Figure 4.4 exhibit an overall near-linear increase in load with deformation, punctuated by fluctuations that can be attributed to the variability and small-scale unevenness of the as-printed friction surfaces in the FDM-fabricated unit cells. Upon initiation of the unloading step, the force rapidly decreases to a relatively small value. However, as the displacement continues to decrease, in several cases this force experiences a slight rebound, remaining at a similar level until the displacement reaches zero. In others, there is a pronounced inflexion in the curve, with this force gradually returning to zero. The FE simulation with a CoF value of 0.547, the same value as the CoF measured in the experiment, exhibits a qualitatively similar pattern, with a rapid drop in vertical reaction as compression is released, followed by a slight rebound and then stabilisation. No permanent deformation was observed during the compression tests, but sometimes the unit cell had to be manually reset to its original position when the restoring force from the frame became insufficient to overcome the effects of stiction between the 3D printed contact surfaces near the end of the load cycle.

The energy dissipated during each compression cycle is obtained by calculating the difference between the energy accumulated by the structure during loading and that released during the unloading part of the cycle, that is, the area enclosed by the loading and unloading curves in Figure 4.4 and the force-displacement graphs in Figure S3 (Appendix C). The energy dissipation predicted by the theoretical model and the FE simulations is compared to the experimental measurements in Figure 4.5, which includes error bars to illustrate the range of variation in the experimental results.

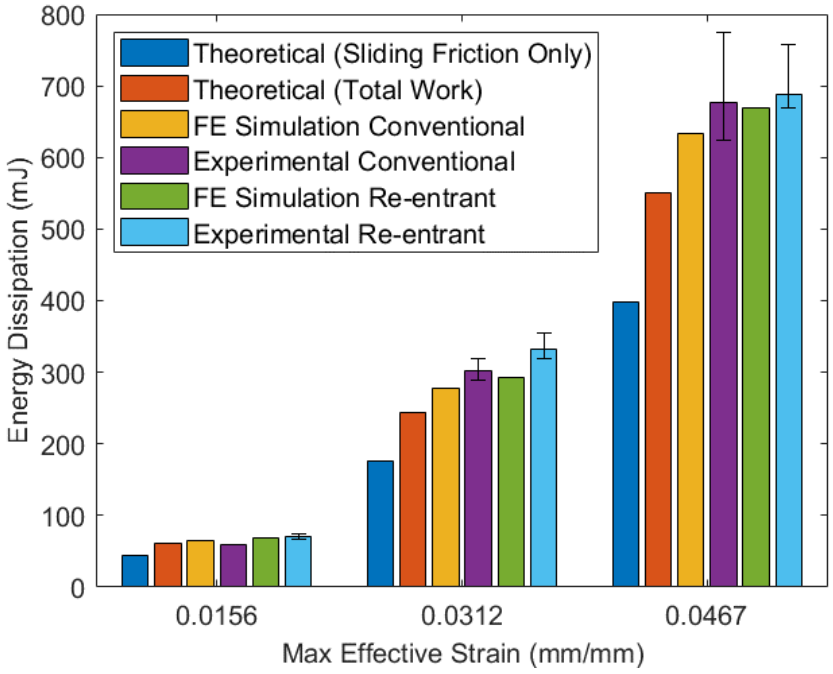

Figure 4.5. The energy dissipation per compression cycle calculated from the theoretical model, FE simulations, and experimental data, with error bars for the experiments; and the total energy absorbed during the loading phase of the cycle as calculated from the theoretical model.

The actual values of the energy dissipation per compression cycle for both conventional and re-entrant unit cells are summarised in Table 4.1.

Table 4.1. Comparison of energy dissipation between theoretical model, FE simulations, and experiments.

Max effective strain (mm/mm)	Theoretical (Sliding friction only)	Theoretical (Total work)	FE simulation (Conventional)	Experimental (Conventional)		FE simulation (Re-entrant)	Experimental (Re-entrant)	
				Min	Max		Min	Max
0.0156	44.23	61.16	64.98	58.99	59.80	68.81	67.32	73.45
0.0312	176.93	244.64	276.86	288.23	319.98	293.03	319.30	354.37
0.0467	398.10	550.44	632.99	624.43	773.65	669.02	627.12	756.71

It is clear that the energy dissipation performance of the experimental unit cells with re-entrant frames (Figure 3.6b) in Section 3.3.1 was better on average than that of those unit cells with conventional hexagonal frames (Figure 3.6a). However, this difference in dissipation tended to decrease as the displacement and consequently the effective strain increased. While for a 1 mm maximum compression, the average energy dissipation from three separate experiments measures

59.5 mJ for the traditional hexagonal model and just over 71 mJ for the re-entrant structure, which represents an improvement of 19%, when the maximum compression is increased to 2 mm, the difference in favour of the re-entrant hexagon frame decreases to approximately 10%. And when the maximum compression reaches 3 mm, the range of energy dissipation values obtained from the experiments is similar for both, so it is not clear whether a difference persists. The FE simulation results mirrored this difference between the unit cells with conventional and re-entrant hexagonal frames, but it clearly persisted as the compression increased.

The equivalent (von Mises) stress distribution over the model geometry in the FE simulations is also investigated, and in the 13-unit cell geometry case, the equivalent stress distribution of the cells located at the edges of the middle layer was smaller than the stress distribution of the cells located at the top or bottom layer (Figure S6 in Appendix E). This is due to the fact that we assumed this 13-unit cell geometry to be in the middle of a structure consisting of a myriad of unit cells and set boundary conditions so that the same displacement occurs on the outer faces located at the same height.

The FE simulation results for a single unit cell and three finite metamaterials constructed from different numbers of the same unit cell are presented in Figure 4.6a. Note that when calculating the effective strain for the multi-unit cell models the maximum height of the structure (the height of the odd columns of multi-unit cell models) is used instead of the average height to get a consistent maximum effective strain value for each simulation. It can be observed that the height of the cycles, i.e. the reaction force to a given compression, varies with the number of unit cells and the height to width ratio of the assembled structure but its overall shape of the load remains relatively consistent as evidenced by their total energy dissipation performance.

The resulting energy dissipation per unit volume during each compression cycle is plotted in Figure 4.6b, which illustrates a clear trend from the single cell through the 8-unit system to the 11-unit and 13-unit cells models. The actual values computed from the simulations are 1.8282×10^{-4} mJ/mm^3, 1.5258×10^{-4} mJ/mm^3, 1.4814×10^{-4} mJ/mm^3 and 1.4837×10^{-4} mJ/mm^3 respectively, representing a 20% decrease from the single unit cell when the number of unit cells exceeded 10.

The results of the simulations of a metamaterial with many unit cells, as represented by an RVE with PBC, are presented in Figure 4.7, along with the corresponding results for a single hexagonal unit cell without PBC, in order to study the influence of PBC. Figures 4.7a and 4.7b are contour plots that visually depict the distribution of stress when compressed by 3mm, consisting of 1.5 mm in the negative y-axis direction on the top face and1.5 mm in the positive y-axis direction on the bottom face, in both models. A scale factor of 3.6 is used to make the deformed geometry more clearly visible. FE simulation results reveal that the equivalent stress distributions of the two oblique sides of each model under the same y-directional uniaxial displacement conditions

are significantly different. In the RVE cell the oblique sides experience higher stress compared to the single hexagonal unit cell without constraint equations, resulting in a difference in deformation with respect to the centre hexagonal frame. The higher stress causes in-plane bending at the lower part of the oblique sides, and out-of-plane bending deformation at the upper part of the oblique walls, as shown in Figure 4.7a. The hysteresis loops of the RVE cell and the single hexagonal unit cell in the FE simulation are plotted in Figure 4.7c, where the paths of the force-displacement curves are substantially divergent due to the varying degree of bending. The peak force value at the end of the loading step is about two times higher for the RVE cell than for the single unit cell, and the energy dissipation is about 40% higher.

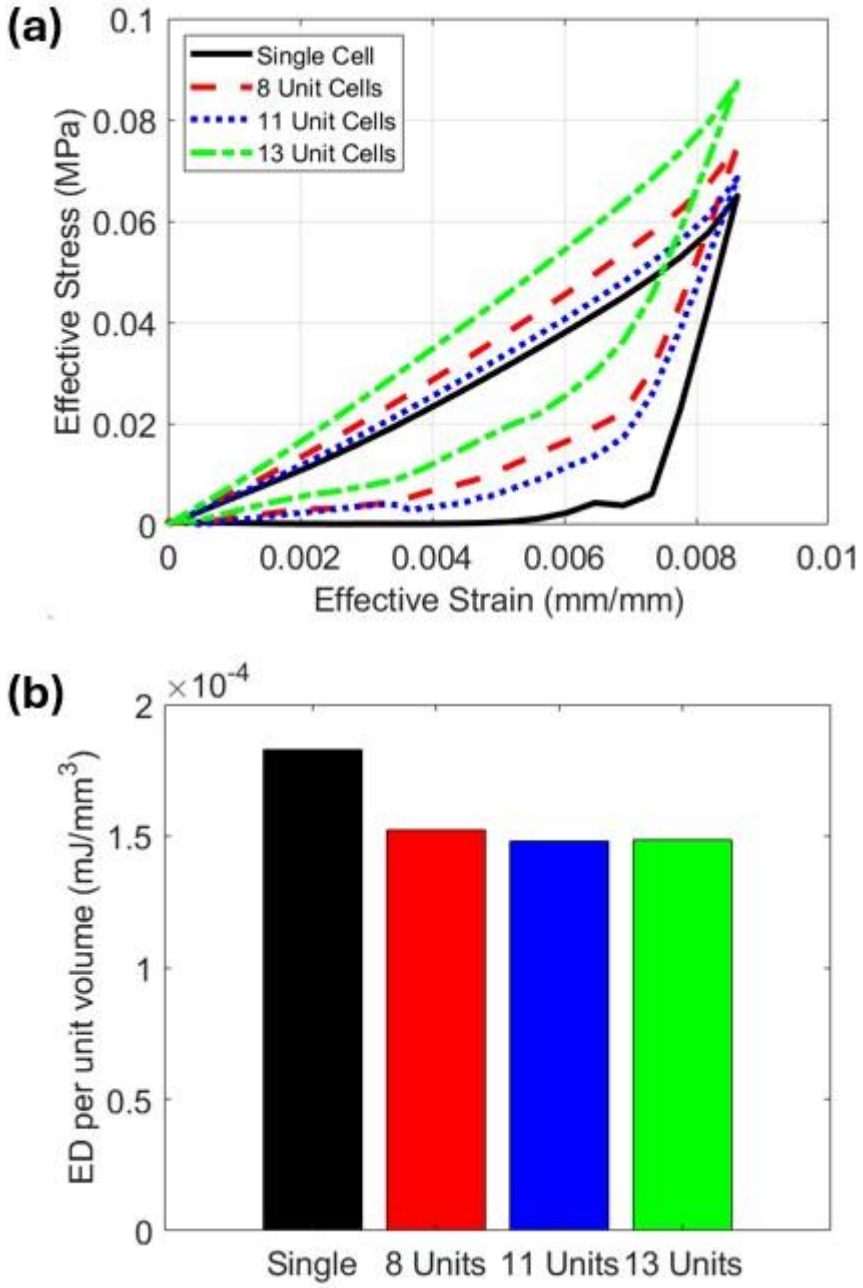

Figure 4.6. (a) Effective stress – effective strain curves from FE simulations of the single unit cell under a 0.5 mm compression cycle, the 8-unit and 13- unit cell metamaterials under a 1.5 mm compression cycle, and the 11-unit cell metamaterial under a 2 mm compression cycle; and (b) the energy dissipation per unit volume calculated from the FE simulations for these compression cycles.

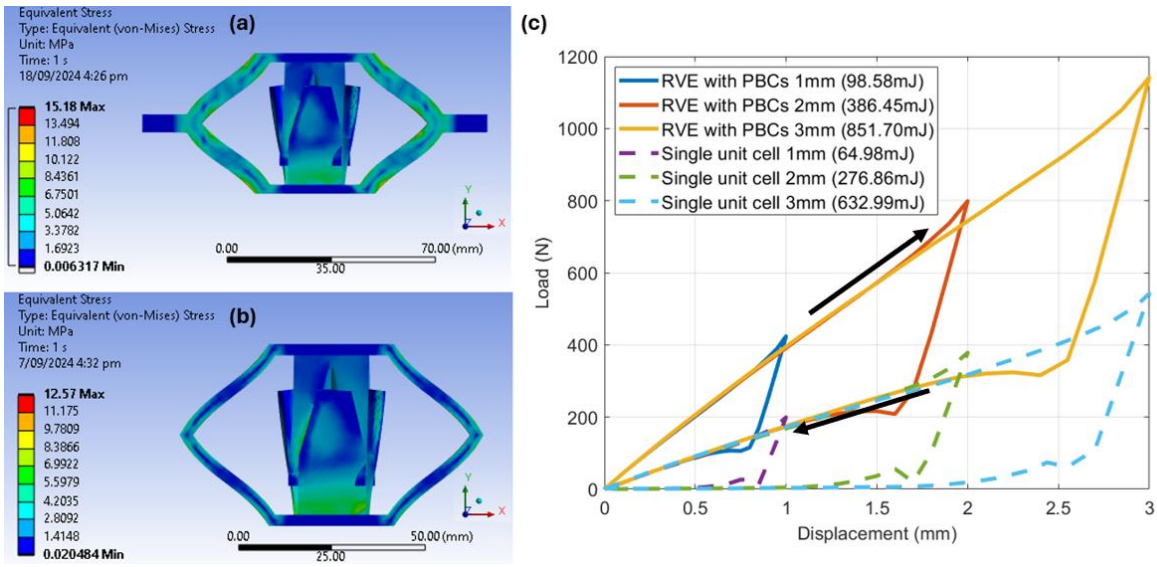

Figure 4.7. Comparison of the visualised deformation aspects and the numerical discrepancies in terms of equivalent stress and energy dissipation. (a) Equivalent stress distribution in the RVE geometry with PBCs applied and a displacement of 1.5mm on the top and bottom faces, respectively, facing each other toward the centre which equals a total 3mm displacement. (b) Equivalent stress distribution in the single conventional hexagon unit cell without PBCs and a displacement of 1.5mm on the top and bottom faces, respectively, facing each other toward the centre. (c) Force-displacement plots obtained from FE simulation by using RVE model with PBCs and single conventional unit cell without PBCs. The black arrows on the plot indicate the forward (loading) and reverse (unloading) directions.

4.4. Discussion

Aside from the well-known variability of 3D printed part shapes and dimensions relative to CAD model geometry, the disparities between the results from compression experiments and FE simulations can be attributed to two main factors. The first is the reliance of FE simulations on idealisations, particularly around contact and friction at the interface between the blades and the columns but also in connections. For example, the connection between the hexagonal frame and the connecting upper and lower parts were modelled as perfectly bonded. However, the actual fabricated parts were assembled using interference fits, which may not be as rigid.

The other and perhaps more important factor is that simulated material properties do not perfectly match real-world behaviour. The unit cell FE simulations used the CPE HG100 compressive modulus as measured by ASTM standard tests. However, because parts of the unit cell structure such as the frame are acting in bending and the measured tensile modulus is significantly higher than the compressive one, the real unit cells can be expected to be stiffer than in the simulation.

For the unit cell with the conventional hexagonal frame, Figure 4.4 shows good qualitative agreement between the shapes of the experimental and computational compression cycles. The experiments consistently produced a higher peak load during loading and a slightly higher load

during the inflection of the unloading curve, which is consistent with the expectation of the experimental unit cell being stiffer due to the material being significantly stiffer in tension and bending than compression. For the re-entrant frame the differences are more marked, with experimentally measured loads being noticeably higher than those predicted by the simulations, particularly for higher compressions. This is because the re-entrant geometry induces higher bending of the frame corners, increasing the influence of the difference between the material's tensile and compressive moduli. There is also less rebounding during unloading which is interpreted as the manufactured re-entrant frame storing greater elastic energy during loading than predicted and facilitating positive separation of the contact surfaces due to the negative Poisson's ratio effect upon unloading.

The single unit cell FE simulation results below the inflection point of the unloading step show a gradual decrease towards zero, unlike the plateaus in the experimental data. In practical experiments, it was observed that in most cases, the load reaches zero before the end of the unloading step, after which it either increases until the end of the unloading step or reaches a certain level and stabilises. This discrepancy between experiments and simulations is hypothesised to stem from the fact that, unlike the simulation model under ideal boundary conditions, in the physical model the contact surfaces, with their aforementioned small-scale unevenness, are not positively separated during the unloading process. The irregular contact surfaces lead to high stick-slip during the loading process, preventing them from completely returning to their original non-contacting state. During the loading step of experiments, significant internal stresses are developed within the contact interfaces due to frictional forces and deformation. The observed rebound in force after it reduces to zero in the unloading step is indicative of these residual internal stresses. As the external load is removed, the internal stresses attempt to restore the structure to its original configuration. However, due to the frictional locking and micro-scale interactions, the columns do not fully return to a stress-free state. This leads to a bounce back to positive force as the internal stresses partially release. After the initial rebound, the force stabilises to a constant positive value during the remainder of the unloading step. This constant force represents the equilibrium state where the residual internal stresses are balanced by the frictional forces at the contact interfaces. The micro-scale roughness and asperities at the contact surfaces prevent complete separation, resulting in a persistent contact force even in the absence of an external load. On the other hand, in the FE simulation, ideal boundary conditions and smooth contact surface geometries are assumed, which do not fully capture the complex microscale interactions and frictional behaviour observed in the physical model. Consequently, the simulation shows a more idealised unloading response, where the force decreases back to zero after the rebound, as the model does not account for the residual internal stresses and persistent

frictional forces present in the actual experiment.

The energy dissipation calculated from the theoretical model, from frictional sliding only, was found to be only about two-thirds of the energy dissipation measured from the experimental and simulation models across all displacements. However, adding all three components of work (Equation 4.17) resulted in better alignment with the experiments. The discrepancy between the theoretical model and the other models is due to the oversimplification of the theoretical model, which results in the theoretical model's estimate of the normal force on the contact surface being significantly off, and also to the uneven nature of the additively manufactured contact surface and the practical difficulties in accurately capturing the resulting frictional forces across the sliding surfaces. While the FE simulation predictions are better, generally being in the neighbourhood of the lower end of the range of experimentally derived values and approximately 10% lower than the experimental average for the 3 mm compression cycle. The FE simulations also match the experimental observations in that the energy dissipation calculated for the unit cell with re-entrant frame is higher than for the conventional frame for all compression cycle depths. However, since the 55×10^3 mm^3 volume of the re-entrant unit cell is about 12.4% greater than that of the 49×10^3 mm^3 conventional unit cell, the actual energy dissipation per unit volume of the conventional hexagonal unit cell is higher than that of the re-entrant version. For the deepest compression cycle this energy dissipation density reaches 0.0143 mJ/mm^3 (average experimental) or 0.0129 mJ/mm^3 (FE simulation) for the conventional unit cell versus 0.0126 mJ/mm^3 (average experimental) or 0.0122 mJ/mm^3 (FE simulation) for the re-entrant version.

As more unit cells are added to the FE model, the peak compressive force and effective stress tended to be larger, while the values of energy dissipation per unit volume tended to be smaller. For example, the 8- and 13-unit cell models had 14.9% and 34.5% higher peak stress, respectively, compared to the single unit cell model. However, the energy dissipation per unit volume was 19.8% and 23.2% lower than that of single unit cell, respectively, which is due to the nature of having a sliding friction surface inside the unit cell, where the honeycomb structures in each half of the top and bottom of the even-numbered columns are inevitably excluded from the sliding mechanism, with or without the geometry inside the hexagonal structure. It is interesting to note that while the energy dissipation per unit volume for the 11-unit cell models is close to that of the 13-unit cell, the peak efficient stress is about 9% lower than even that of the 8-unit cell, suggesting that the addition of more rows of unit cells toward the axis where external force is applied, can lead to results similar to the peak efficient stress value of the single unit cell. The middle units of an even row will exhibit a sliding mechanism indirectly in response to its neighbouring cells, unlike the odd rows where the displacement condition is set directly at the top. As a result, it seems reasonable that the energy dissipation per unit volume values for metamaterial models with a

limited number of unit cells tend to decrease as the number of even-numbered columns increases. However, assuming a frictional metamaterial with an infinite number of honeycomb structures, especially with many rows, it can be inferred that the proportion of half unit cells that are excluded from the energy dissipation mechanism at both ends of the metamaterial will be infinitesimally small in the total metamaterial, and in this case, the results will be almost identical to those of the single cell model.

The higher stresses in the RVE cell with PBCs significantly affect the path of the force-displacement curves. The change in the peak force at the maximum displacement between the RVE cell and single hexagonal unit cell is approximately double, an increase which can be interpreted as a consequence of the additional stiffness induced by the PBC constraints in the RVE cell. In terms of energy dissipation, the RVE cell achieves a higher quantity of around 40%, due to an increase in the frictional stress levels during contact and sliding between the columns and blades. In other words, this result reveals that the proposed frictional metamaterial will have significantly better energy dissipation performance than a single unit cell and holds promise for applications requiring repeatable energy dissipation under relatively slow to moderate loading rates, i.e. vibration damping and not impact or shock.

4.5. Conclusions

This chapter proposes a mechanical metamaterial that dissipates energy through friction while operating within the elastic regime, which allows it to perform repeated energy dissipation cycles, unlike many other mechanical metamaterials and architected materials that depend on plasticity and fracture. It also differs from other metamaterials that use friction in the novel design of its frictional mechanism. The proposed frictional metamaterial was studied through experiments, theoretical analysis, and finite element simulations of its unit cell. Both conventional and re-entrant versions of the hexagonal unit cell were considered. For the experiments, multiple unit cells were manufactured by 3D printing with CPE HG100, a stiff polymer. Once the computational simulation had been validated through comparisons to the experimental data and theoretical model, it was then extended to the simulation of finite meta-material specimens consisting of less than and more than ten unit cells.

When the unit cells were subjected to low-speed compression cycles there was a good match between the shapes of the experimental and computational load-displacement curves. However, the experimental curves exhibited higher force and stress for any given displacement than those produced by the finite element model, i.e. the curves were shifted up. This difference was relatively minor for the conventional hexagonal unit cells but more marked for the re-entrant cells, and this greater stiffness of the physical unit cells was attributed to the use of the compressive

elastic moduli in the simulations.

This similarity between the shapes of the load-displacement curves expressed itself in good agreement between experiments and simulations in the area between the loading and unloading curves, and therefore the energy dissipated per cycle, particularly for the conventional hexagonal unit cell. When the finite element simulations were extended to finite metamaterials, it was found that with the change in unit cell boundary conditions, there was a drop in energy dissipation per unit cell, but this reduction tapered off once there were more than ten unit cells in the metamaterial.

These results demonstrate the potential of this frictional metamaterial concept to provide superior elastic energy absorption and dissipation performance. This makes it an interesting solution for applications in which repeated energy dissipation or damping under cyclical loads is required in combination with light weight. Future unit simulations and experiments on unit cells using different constituent materials and additive manufacturing methods will explore the potential of different combinations and the influence of varied loading rates.

CHAPTER 5: ENERGY DISSIPATION IN A NONLINEAR METAMATERIAL WITH INTERNAL DAMPING

This chapter unveils the experimental and finite element models of a frictional mechanical metamaterial for investigating the energy dissipation behaviour of the TPU 95A, a family of Thermoplastic Polyurethane which presents hyperelastic and viscoelastic behaviour, at quasi-static uniaxial loading, validated by comparing each result. Theoretical calculation is also carried out to reinforce the reliability of this analysis. The frictional mechanical metamaterials made of TPU 95A filament by fused deposition modelling (FDM) are examined under various applied displacement conditions. Mooney-Rivlin 3 parameter for the hyperelastic material model is selected to curve fitting the raw data obtained from the compression test with cylindrical specimens and for the major material parameters calculations. To reflect the complex mechanical behaviours of the TPU 95A used in this study, loading experimental data and unloading experimental data are applied to the corresponding simulation steps, respectively. Only using the previous theoretical equations in Chapter 4 for typical elastic metamaterials revealed that a bit of discrepancy occurs compared to experimental results. To compensate for this, an energy dissipation factor inside the material was added to the existing theoretical model.

5.1. Introduction

Mechanical metamaterials have emerged as an attractive area of research in engineering and materials science as they offer a paradigm shift in the design and fabrication of structures and mechanisms, with several remarkable mechanical properties, such as negative stiffness [16, 19] and negative refractive index [21, 22] having already been achieved. Furthermore, metamaterials offer great design flexibility owing of their tailored properties and the possibility of tuning them in response to external stimuli [28, 29]. Mechanical metamaterials achieve these remarkable properties while using existing constituent materials because of their engineered structural geometries. These geometries are designed to manipulate mechanical behaviours like deformation, wave propagation and damage tolerance in unprecedented ways, leading to materials with properties not normally seen in nature. Generally, ‘loss’ or energy dissipation has been considered anathema in metamaterials, and something to be avoided or minimized as much as possible. However, a paradigm shift has emerged where engineered losses are becoming a useful ingredient to control and direct mechanical energy transport in ways that give rise to exotic wave phenomena, which can then be used to create devices ranging from hypersensitive sensors to perfect absorbers.

Energy dissipation is also crucial for applications where vibration control is important, such as in many machines, buildings, and aerospace structures. In recent years, there have been several

studies of proposed mechanical metamaterials that achieve energy dissipation through friction: a design in which beams are inserted inside a hexagonal structure and actuated by a mechanism that causes contact and sliding between the beams when an external force is applied [85], another in which energy dissipation is the result of a combination of contact friction and interlocking mechanisms in a multilayered, parrot-beak-like structure inside a cylindrical-shape unit cell [125], an I-shape structure in which orthogonal beams are designed inside intended to induce energy dissipation through internal contact and vibration [87], while original intuitive or bio-inspired designs have continue to be reported.

Internal material damping, an intrinsic property in viscoelastic materials, is another potentially important source of energy dissipation and is included in this study. The idea of leveraging the internal energy dissipation effect of materials and applying it to metamaterials with more complex geometries was proposed by Dykstra *et al*. [126]. Numerous studies have explored the various mechanisms of internal damping across diverse materials. In polymers, viscoelastic damping is predominantly the result of molecular chain mobility, which leads to significant energy dissipation as these chains undergo internal friction and rearrangement. Rubber-like elastomeric polymers possess high damping properties, making them attractive for use in vibration isolators [127, 128]. Shape memory alloys, like Nitinol, exhibit phase transformation damping capacity, where the reversible transformation between the martensite and austenite phases leads to energy dissipation [129, 130]. Crystalline metals mainly display dislocation damping, where energy is dissipated by the movement of dislocations through the defects in the crystal lattice [131]. These studies highlight the different mechanisms by which different materials dissipate energy internally. By understanding and harnessing these mechanisms, mechanical metamaterials for energy dissipation do not rely solely on the design of internal structures for friction, but on the internal energy dissipation of the materials that make up the metamaterial itself.

Thermoplastic polyurethanes (TPU) are an attractive option as a constituent material for dissipative metamaterials because they offer a combination of hyperelasticity and viscoelasticity [132, 133]. TPU presents an interesting avenue for developing mechanical metamaterials with significant internal damping due to their ability to be subjected to large deformations or rotations and then fully return to the initial shape when unloaded, with zero to negligible plastic deformation. This behaviour is commonly observed in materials like rubber, elastomers, soft tissues, and foams. The resilience characteristic at high strain rates makes hyperelastic materials reusable [134, 135]. In civil engineering, hyperelastic materials are utilised in seismic isolation devices for buildings and bridges. Their ability to facilitate energy dissipation helps prevent structural damage during earthquakes [136, 137]. Hyperelastic materials are also used in prosthetics and orthotics to provide comfort to users via energy-absorbing components [138, 139].

By absorbing external impacts during walking or running, alleviating the shock on a joint. In addition, thanks to the properties of superior damping capability and high deformability, hyperelastic materials are used in multiple automotive components, including car door seals, suspension systems and engine mount components [140, 141].

The previous chapter studied a dissipative mechanical metamaterial 3D printed from CPE HG100, a stiff linearly elastic material with negligible internal damping, where the energy dissipation was generated by friction. This chapter examines the energy dissipation capacity under cyclic loading of a dissipative metamaterial that combines significant material damping with friction. It does so through the analysis and testing of a metamaterial unit cell prototype made of TPU 95A, a material that combines a large elastic strain capability with viscoelastic characteristics. In other words, in this chapter, softer materials with viscoelastic properties are used to investigate the contribution of the material's internal damping to the overall energy dissipation and the effect of low material stiffness. Experimental results are compared and analysed with finite element (FE) simulations and theoretical analyses.

5.2. Methodology

The TPU 95A material covered in this chapter is a nonlinear material with hyperelastic and viscoelastic properties, which is distinctly different from the linear material such as CPE HG100 covered in Chapter 4. This section describes the nonlinear material models, presents an enhanced theoretical model, and discusses the methodology for modifying the finite element model to include nonlinear materials.

5.2.1 Nonlinear material models

TPUs have emerged as a versatile material across a range of industries, attributable to their exceptional synergy of mechanical and thermal properties. Within the engineering fields, TPUs, with their superior resilience and ability to undergo large displacements for energy dissipation, have garnered attention as a potential alternative to high-damping rubber [142]. The mechanical response of TPUs is inherently complex, exhibiting hyperelstic properties such as strain-dependent stiffness as well as viscoelastic properties like load rate dependence [143-145]. In order to simulate TPU with such nonlinear mechanical behaviour, a number of attempts have been made and various constitutive models have been presented.

From simple simulations using the hyperelastic constitutive models in ANSYS, we selected the Mooney Rivlin 3-parameter model for unit cells FE simulations based on its high agreement with compression experimental data using the cylindrical shape specimens. Experiments in three modes of deformation are carried out, followed by calibration, or curve-fitting for the hyperelastic coefficients. These three deformation modes involve uniaxial tension, uniaxial compression or

biaxial tension, and shear. Taken together, these modes supply a comprehensive dataset necessary for the precise calibration of hyperelastic materials. In cases where materials are either entirely or nearly incompressible, volumetric data measurements can be excluded, operating under the assumption that the material is completely incompressible. Utilising test data for calibration of a hyperelastic model in only one of these three deformation modes will result in a reliable model response only within that specific deformation mode. Since the unit cell designed in this paper experiences sliding along friction surfaces during the compression process, curve fitting was performed using data obtained under the uniaxial compression model.

5.2.2 Theoretical analysis

When analysing the proposed dissipative metamaterial unit cell, it is assumed that there are four main factors to consider when calculating the total work W_{total} under uniaxial compression. The first three were addressed in previous chapter [146]; bending work W_{frame} for the side walls of the frame (Figures 3.1g and 3.2a), bending $W_{columns}$ of the four tapered columns (Figure 3.1a), and sliding at the four pairs of column-blade contact surfaces $W_{sliding}$. Here we add a fourth work component W_I to represent the contribution of internal energy dissipation, that is the material's internal damping. The first and second components of this total work are stored as elastic energy, which can be recovered during unloading, while the last two components are dissipated. Equations 5.2, 5.3, and 5.4 are previously derived formulas for computing the values of the first three components of the total energy input to the unit cell from the work done by the compressive load.

$$W_{total} = W_{frame} + W_{columns} + W_{sliding} + W_I \tag{5.1}$$

$$W_{frame} = \int_0^{\delta} F\, d\delta' = \frac{E * b * h^3 * \delta^2}{L^3 * sin^2(\theta_1) * 2} \tag{5.2}$$

$$W_{columns} = \int_0^{\delta} F_{bending}\, d\delta' * 4 = \frac{\delta_{bending}^2 * 3 * E * I_{column}}{2 * l^3} * 4 \tag{5.3}$$

$$W_{sliding} = \frac{\mu * 3 * E * I_{Column} * \delta^2}{l^3 * cos(\theta_2) * sin(\theta_2) * tan\,(\theta_2)} * 4 \tag{5.4}$$

Next the internal energy dissipation component W_I is added and the other three terms are modified to take into account the nonlinear nature of the material's stress-strain response to

loading. The modified theoretical model can then be expressed as

$$W_{total} = \left[\frac{b * h^3 * \delta^2}{L^3 * sin^2(\theta_1) * 2} + \frac{\delta_{bending}^2 * 6 * I_{column}}{l^3} + \frac{\mu * 3 * I_{column} * \delta^2 * 4}{l^3 * \cos(\theta_2) * \sin(\theta_2) * \tan(\theta_2)}\right] \int_0^{\delta_{max}} E(\delta)\, d\delta + W_I \quad (5.5)$$

Here, integral part refers to the nonlinear Young's Modulus which varies as a function of the applied displacement. In this research, Young's moduli were investigated through compression tests on cylindrical specimens, whose results are presented in Table S5 in Appendix I.

We attempted to calculate the internal damping effect of hyperelastic material using the Mooney-Rivlin 3 parameter model and the derivation process can be found in Appendix J. The final derived form of W_{hyper}, the strain energy per unit volume, is presented in Equation 5.6.

$$W_{hyper} = C_{10}\left(\lambda^2 + \frac{2}{\lambda} - 3\right) + C_{01}\left(2\lambda + \frac{1}{\lambda^2} - 3\right) + C_{11}\left(\lambda^2 + \frac{2}{\lambda} - 3\right)\left(2\lambda + \frac{1}{\lambda^2} - 3\right) + \frac{1}{d}(J-1)^3 \quad (5.6)$$

From the Appendix J, W_{hyper} represents the stored energy in the material under compression. Compression testing of TPU 95A material specimens reveals that the loading and unloading curves are best represented by different hyperelastic coefficients, resulting in hysteresis that is a manifestation of this material's viscoelastic side. To account for this combination of hyperelastic and viscoelastic behaviour, W_{hyper} is multiplied by the energy loss fraction value, which is denoted as the amount of energy absorbed by the amount of energy dissipated, to calculate the internal energy dissipation, W_I.

$$W_I = W_{hyper} * \frac{Energy\ Dissipation}{Energy\ Absorption} \quad (5.7)$$

In the compression testing of the material the energy loss fraction varies with the degree of strain applied and tends to increase as the applied displacement increases.

5.2.3 Finite element analysis (FEA)

The constituent material in this section, TPU 95A, was considered incompressible, and its viscoelastic behaviour was captured by applying two different hyperelastic material laws during the loading and unloading parts of the load cycle. Both material laws were in the Mooney-Rivlin 3-parameter form but with different coefficients derived from compression tests on material specimens.

Two different FEA models were examined, with the first model replicating the unit cell compression test described in Figure 3.3 and the second model in Figure 3.5 representing a unit cell embedded in a periodic meta-material under uniaxial compression.

5.2.3.1 Hyperelastic material models

Materials within hyperelastic category share certain common attributes. They tend to carry a soft nature in comparison to the majority of metals, exhibit a nonlinear stress-strain response with a monotonically increasing behaviour, and follow the same path on the stress-strain curve during both loading and unloading phases. It suggests that the energy expended during their deformation is preserved, being stored as internal energy that is fully recoverable upon unloading. These particular characteristics of the hyperelastic materials are utilised in the formulation of constitutive models, which centre on the strain energy density. This density represents the amount of internal energy stored within a given volume of the material.

The strain energy density, also known as the total strain energy stored per unit volume indicates the area under the stress-strain curve towards the point of deformation. Equation 5.8 is determined by the strain the material is subjected to, while the stresses Equation 5.9 generated are computed based on the type of deformation - tension, compression, or shear. Consequently, the response of a material can vary depending on the mode of deformation it undergoes. Due to the intricate stress-strain interactions intrinsic in elastomeric materials, hyperelasticity is generally defined by an equation referred to as a strain energy potential. The difficulty lies in ascertaining the coefficients within this equation to effectively characterize the material properties at hand. This is where experimental data from controlled tests plays a key role in aiding in the determination of these coefficients.

$$\Psi = f(\varepsilon) \tag{5.8}$$

$$\sigma = g(\varepsilon) \tag{5.9}$$

To accurately represent the strain energy density of a specific hyperelastic material using appropriate theories and methods, various hyperelastic constitutive models have been suggested by researchers. Notable examples include the Neo-Hookean [147], Mooney-Rivlin [148], Ogden [149], Yeoh [150], and Gent models [151]. Since there is no clear-cut distinction as to which hyperelastic model works most suitably, the raw data from the mechanical test with samples should be examined against the above-mentioned models to determine which model best describes the material response.

5.2.3.2 Curve fitting

Calibrating hyperelastic material models by curve-fitting to data in Ansys Workbench 2023R2 is necessary to carry out simulations with a constituent material, TPU 95A, which could be considered possessing hyperelastic mechanical properties due to its high flexibility. The process of calibrating a material model entails the selection of a hyperelastic constitute model and its adaptation to fit the existing experimental data. Consequently, constants that serve as representative material properties can be derived. Within Ansys Mechanical, there exist multiple hyperelastic material models that users can choose, subsequently tuning them via curve-fitting within the engineering data module. The curve-fitting procedure involves the computation of the cumulative disparity between the data from experiments and the model's predictions, intending to minimise this divergence to identify an optimal array of material constants. This disparity is measured by an error function known as the least squares function. The method employed to minimise this function varies depending on the model's nature and the number of material constants, it encompasses both linear and nonlinear regression techniques. Equation 5.10 displays the least square function.

$$Error = \sum_{i=1}^{n} (\sigma_E^i - \sigma_M^i)^2 \tag{5.10}$$

Here, σ_E and σ_M denote the stress data of the experiment and model's prediction, respectively.

The minimised value of this error function is known as a residue, which can be used as a means to evaluate and compare the fitting quality of different models. In each hysteresis loop of three deformation modes, there exists an inflection point somewhere within the response. This characteristic typically suggests the possibility of the material response being composed of two or more contributing terms. To perform curve-fitting through ANSYS Workbench, access engineering data, add new hyperelastic material, and attach property on uniaxial test data from the toolbox under hyperelastic experimental data.

5.2.3.3 Implementation of experimental data for TPU 95A in ANSYS Workbench

In the case of TPU 95A used in this study, although it exhibits some hyperelastic properties, compression experiments using cylindrical specimens revealed energy dissipation due to the mismatch between the loading and unloading force-displacement curves. This behaviour defers from that of purely hyperelastic material, which exhibits perfect incompressibility, where the loading and unloading curves coincide, resulting in no hysteresis region.

The discrepancy in the stress-strain curves of the loading and unloading steps led to the requirement to define the two segments with separate engineering data. In fact, when FEA was

performed using only loading data, it was found that the curve progression in the unloading step followed a path that was quite different from the experimental results. Therefore, we defined the data extracted from the single cycle loading experiment with the specimens as separate engineering data by dividing it into a loading part and an unloading part, respectively, and then applied the data to each time step corresponding to the loading and unloading of the simulation. This was done using an APDL snippet, and the flow chart below visualises the method sequentially (Figure 5.1). In ANSYS Workbench, as of the 2023 version, there was no option to directly apply different material properties to one body for each step, so we were able to implement this idea by adding a separated extra body that was not involved in dissipating energy through compression, pre-applying the unloading data, and then swapping the material properties when the simulation moved to the unloading step.

In order to obtain internal energy dissipation from FE simulation, two different settings – 1) loading data are applied to the loading step, and unloading data are applied to the unloading step. 2) only loading data are applied to the whole simulation process – are established. The total energy dissipation can be obtained from the first simulation setting and the internal energy dissipation can be obtained from the gap between the first and second setting simulation results.

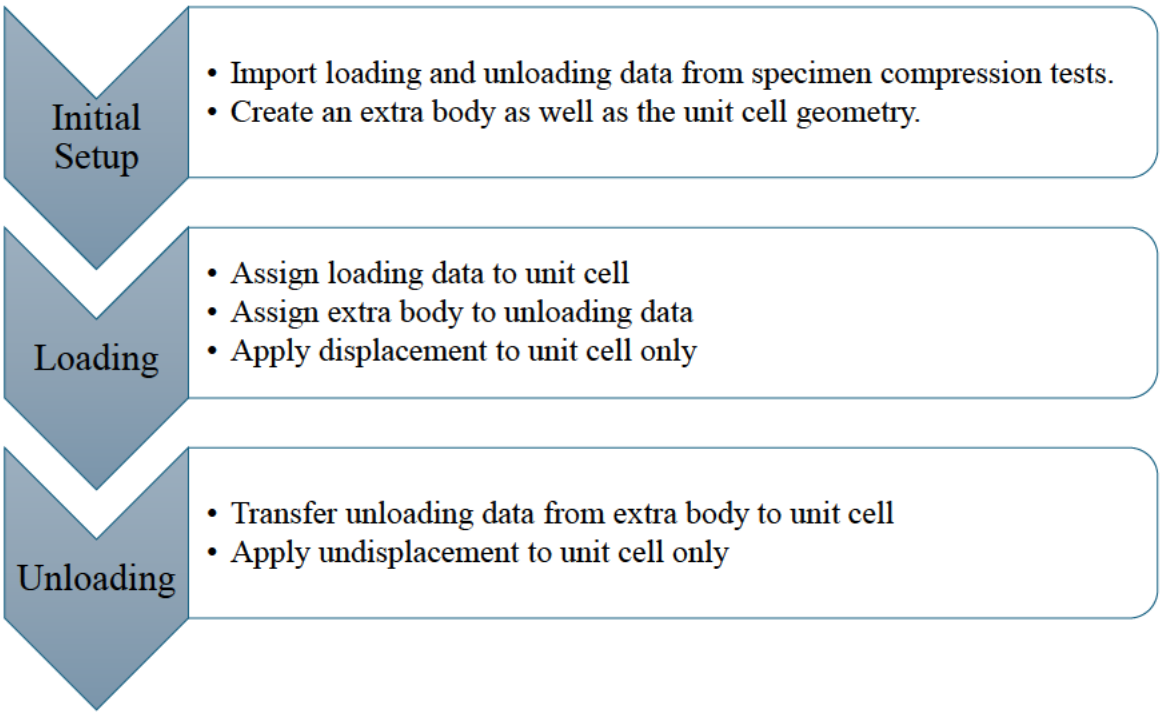

Figure 5.1. Flow chart to describe the process of FEA with two different material properties applied at two different time steps.

5.3. Results

5.3.1 Material characterisation

The data from the 50% strain compression tests were imported into ANSYS 2023R2 Workbench where it was found that the Mooney-Rivlin three-parameter model was the closest fit to the experimental data. (Appendix G, Figure S9.). Under compression the cylindrical material characterisation specimen exhibited inflection points in the stress-strain graph, a typical feature of hyperelastic materials. However, TPU 95A's viscoelastic aspect manifested itself in a large difference in response between the loading and unloading steps. The hyperelastic material model fitting function in ANSYS Workbench assumes that the material follows the same trajectory when loading and unloading, so the data was divided into two parts, one corresponding to loading and the other to unloading, and curves fitted separately.

The loading and unloading responses are shown in Figure 5.2 which plots the test data and the Mooney-Rivlin model that resulted from curve fitting for each of these two steps. The values of the Mooney-Rivlin model coefficients C_{10}, C_{01}, and C_{11} for TPU 95A are shown in Table 5.1 and Table 5.2. The incompressibility parameters D1, D2, and D3 are shown as zero because it was assumed to be a perfect hyperelastic material.

Table 5.1. Material constants for Mooney-Rivlin 3 parameter strain energy density function by using loading data.

Coefficient	Value (MPa)
C_{10}	-1.6428
C_{01}	4.7527
C_{11}	0.5021

Table 5.2. Material constants for Mooney-Rivlin 3 parameter strain energy density function by using unloading data.

Coefficient	Value (MPa)
C_{10}	-9.4744
C_{01}	10.858
C_{11}	4.5649

The path difference between loading and unloading explicitly indicates that there is some degree of hysteresis involved, which results in energy dissipation. The measured ratio of energy

dissipation and absorption in tests with 0.0156 mm/mm, 0.0312 mm/mm, and 0.0467 mm/mm maximum strain are 25.5%, 25.9% and 27.0%, respectively (Figure S8 in Appendix F.). These calculated energy loss fractions are substituted into the theoretical model to calculate W_I, which represents the internal energy dissipation (Equation 5.7).

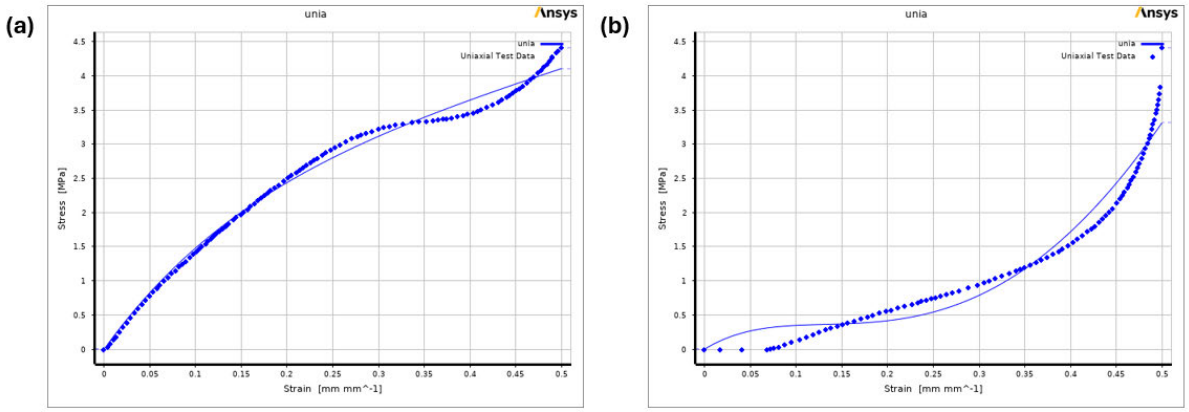

Figure 5.2. Plotts of the solid cylinder test data up to 50% compression strain (points) and the corresponding curve fits (solid lines) with the Mooney-Rivlin 3-parameter model in ANSYS Workbench for (a) loading and (b) unloading phases.

5.3.2 Single unit cells

When finding the total work in the theoretical model, consider the relationship between strain and stretch expressed in Equation 5.11, instead of directly substituting the effective strain+1 value into the stretch λ, equivalent elastic strain (also called von Mises elastic strain) values were obtained from the FEA and substituted into Equation 5.6 to obtain W_{hyper}. The von Mises or equivalent strain ε_{equ} can be calculated as Equation 5.12.

$$\lambda = 1 + \varepsilon \tag{5.11}$$

$$\varepsilon_{equ} = \frac{1}{1+v'}\left(\frac{1}{2}[(\varepsilon_1 - \varepsilon_2)^2 + (\varepsilon_2 - \varepsilon_3)^2 + (\varepsilon_3 - \varepsilon_1)^2]\right)^{\frac{1}{2}} \tag{5.12}$$

where v' indicates the effective Poisson's ratio.

Table 5.3 lists the Von Mises Elastic Strain values as a function of displacement for the unit cell model.

Table 5.3. Von Mises Elastic Strain values as a result of the applied displacements, as measured from the FEA performed using ANSYS Workbench 2023R2.

Maximum compression (mm)	Von Mises Elastic Strain (mm/mm)
1	0.0024469
2	0.0048847
3	0.0071519

Figures 5.3(a-c) and Figures 5.3(d-f) depict the stress-strain curves for a single uniaxial load cycle from compression tests and FE simulations under maximum vertical uniaxial compression of 1mm, 2mm, and 3mm for both conventional hexagonal and re-entrant unit cell, respectively.

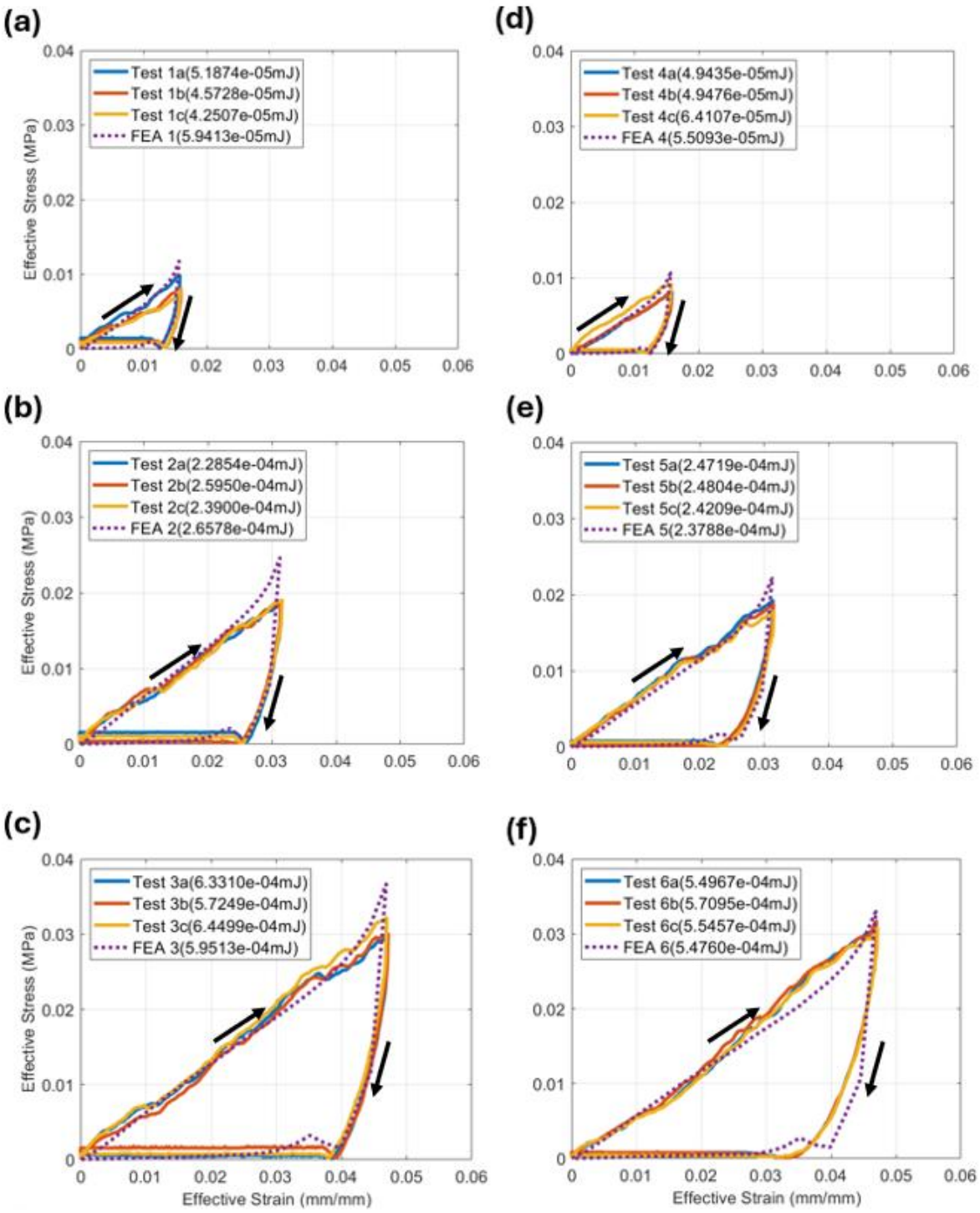

Figure 5.3. Effective stress-strain results from compression experiments and FE simulations for (a) 1mm (b) 2mm and (c) 3mm compression cycle applied to unit cell with a conventional hexagonal frame illustrated in Figure 3.3a; and equivalent results for (d) 1mm, (e) 2mm and (f) 3mm compression cycle applied to unit cells with a re-entrant frame illustrated in Figure 3.3b.

The energy dissipation is calculated from the area within the stress-strain loops in Figure 5.3. Table 5.4 lists the energy dissipation predicted by the finite element models, and the theoretical

model, together with the range of values obtained from each set of experiments.

Table 5.4. Comparison of energy dissipation (mJ) between theoretical model, FE simulations, and experiments.

Max effective strain (mm/mm)	Theoretical model	FE simulation (Conventional)	Experimental (Conventional)		FE simulation (Re-entrant)	Experimental (Re-entrant)	
			Min	Max		Min	Max
0.0156	4.1567	5.7212	4.09	5.00	5.9779	5.36	6.96
0.0312	20.1734	25.5933	22.01	24.99	25.8113	26.27	26.91
0.0467	45.9014	57.3093	55.13	62.11	59.4176	59.64	61.95

The energy dissipation predicted by the theoretical model and FE simulations are also compared to the experimental measurements in Figure 5.4, with error bars included to illustrate the range of variation in the experimental results.

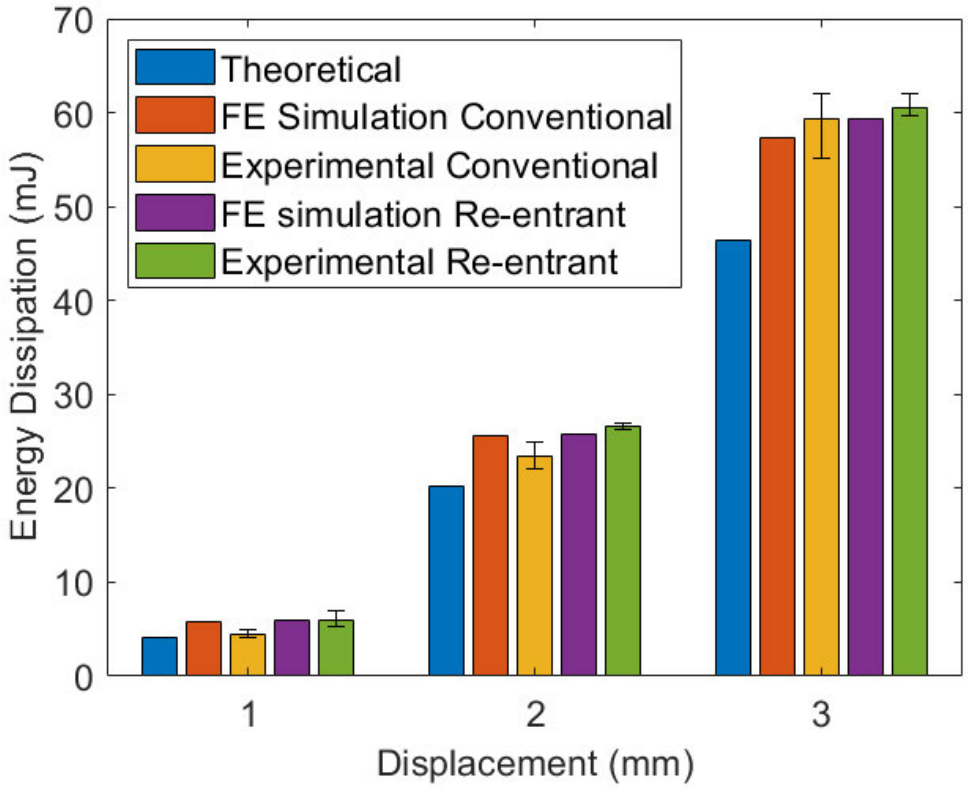

Figure 5.4. The energy dissipation per compression cycle calculated from the theoretical model, the FE simulations and the experiments, with error bars to indicate the scatter in the experimental data.

The stress distributions under compression for each unit cell frame geometries illustrated in Figure 3.1g and Figure 3.2a are exemplified by Figure 5.5. This part of the unit cell functions as a spring, bending when an external force is applied, storing energy, and then trying to return to its original shape when unloaded. Because of this bending behaviour some areas of this structure can be under tension even though the overall unit cell is under compression. Figure 5.5 distinctly illustrates the distribution of the maximum principal stress, which indicates the existence of tensile stress regions.

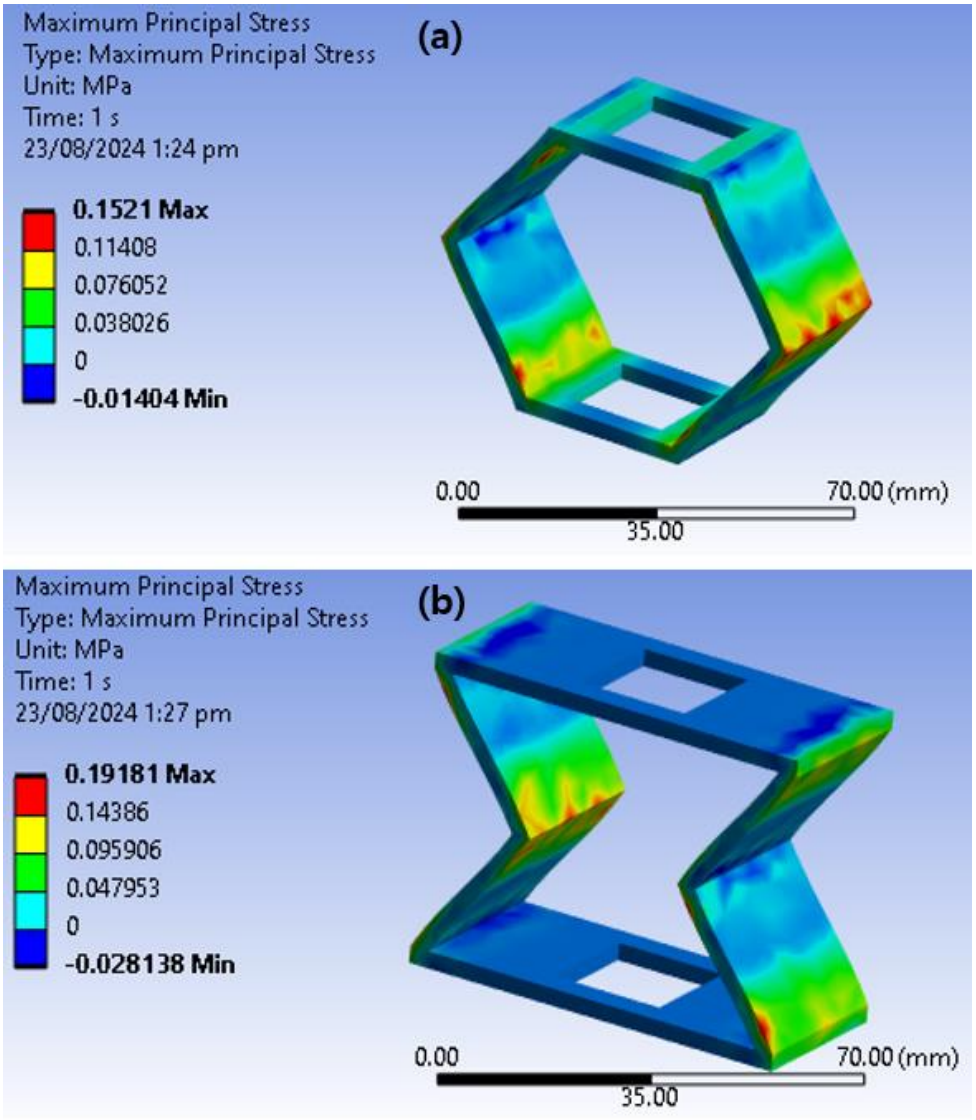

Figure 5.5. Comparison of the maximum principal stress distribution in the unit cell frame of (a) conventional hexagon and (b) re-entrant shapes. Because the compressive displacement direction is opposite to the coordinate system axis, positive values indicate compressive areas and negative values (dark blue) indicate tensile regions.

5.3.3 RVE cell in a periodic metamaterial

Figures 5.6a and 5.6b illustrate the equivalent stress distributions when a total compression of 7 mm is applied to the conventional hexagonal RVE model with and without PBC, respectively. Likewise, Figures 5.6d and 5.6e display the equivalent stress distributions for the re-entrant RVE cell with PBC and without PBC. This applied displacement is beyond the repeatable elastic deformation range of 3 mm for frictional metamaterials made of CPE HG100 as a constituent material and was set to check the repeatable energy dissipation ability of TPU 95A, which has soft physical properties, under more excessive displacement conditions. Note that a scale factor of 1.3 has been applied to the deformations to enhance their visibility. Figures 5.6c and 5.6f show the force-displacement curves produced by the FE simulation, which are significantly different than those for the single unit cell, as shown in Figure 5.3.

It is interesting to note that for the single unit cell there was little stress in the oblique sides of the frame while for both RVE cells it was significantly higher, and around the sliding contact surfaces the peak equivalent stress value was slightly lower. However, the increased bending stiffness of the oblique frame sides in the RVE cell resulted in significantly higher vertical forces and elastic energy for a given compressive displacement, while the average contact pressure was of a similar order of magnitude, which together contributed significantly to the expansion of the hysteresis region as the stored elastic energy was released relatively rapidly upon unloading.

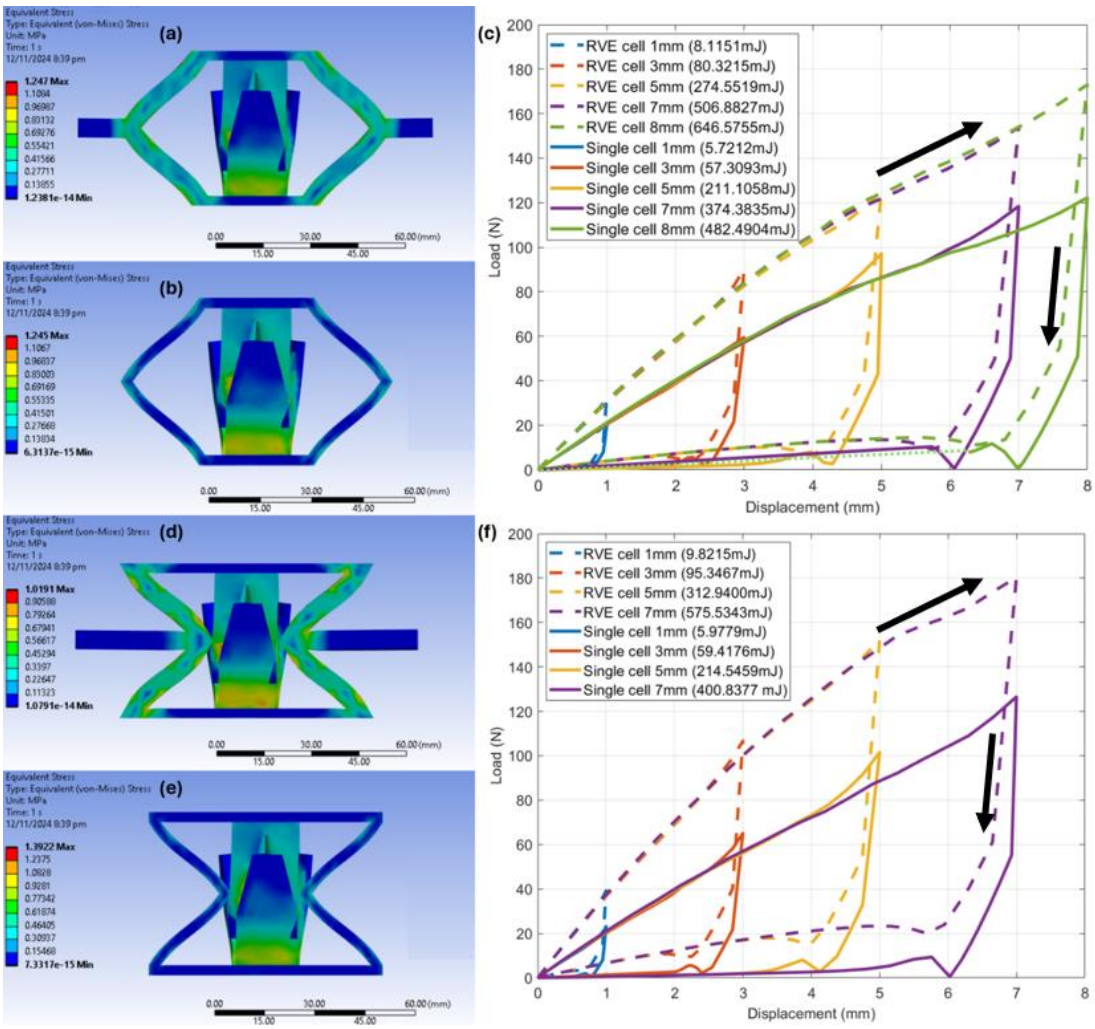

Figure 5.6. FE simulation results for RVE cells with PBC and a single unit cell without PBC, both under 7 mm compression, showing (a) contour plot of equivalent (von Mises) stress in the deformed conventional hexagonal RVE, (b) contour plot of equivalent stress in the single conventional hexagonal unit cell, (c) force-displacement plots for the hexagonal RVE and single hexagonal unit cell, (d) equivalent stress contour plot for the re-entrant RVE, (e) equivalent stress contour plot for the single re-entrant unit cell and (f) force-displacement plots for the re-entrant RVE and single re-entrant unit cell. For the 8 mm displacement curve for the single unit cell in Figure 5.6c, the simulation did not go all the way through, so we extrapolated the missing parts and plotted them as a dotted line and estimated the predicted energy dissipation based on the completed plot. For the Re-entrant model, we did not apply displacements greater than 7 mm due to the penetration between the exterior wall and internal structure. For Figures 5.6d and 5.6e, a scale value of 1.3 was applied, so penetration appears to occur, but this was not the case when the true scale value was applied.

5.3.4 Contribution of internal material damping to energy dissipation

The respective proportions of energy dissipation due to friction and internal damping resulting from the component itself in the theoretical and simulation models are shown in Table 5.5 and Figure 5.7. The columns in Table 5.5 first provide the calculated values of the frictional sliding of

the theoretical model, then the internal energy dissipated through material damping, denoted as W_I in this paper, and finally the total work applied to the unit cell except the elastic factors. The contribution of internal material damping in the FE simulation was computed through additional FE simulations that were performed using only the loading data, and compared to the FE simulation results in Figure S11 in Appendix H. Figure 5.7 compares the contribution of sliding only, and internal energy dissipation factor only to the total energy dissipation in both models.

Table 5.5. Relative contributions of material hysteresis and frictional hysteresis to energy dissipation via the theoretical model.

Max Effective Strain (mm/mm)	Theoretical Frictional Sliding (mJ)	Material only W_I (mJ)	Sliding + Material (mJ)	Ratio Material per Total (%)
0.0156	3.0016	0.6956	3.6972	18.8142
0.0312	13.9020	2.8072	16.7092	16.8003
0.0467	30.7688	6.4041	37.1729	17.2279

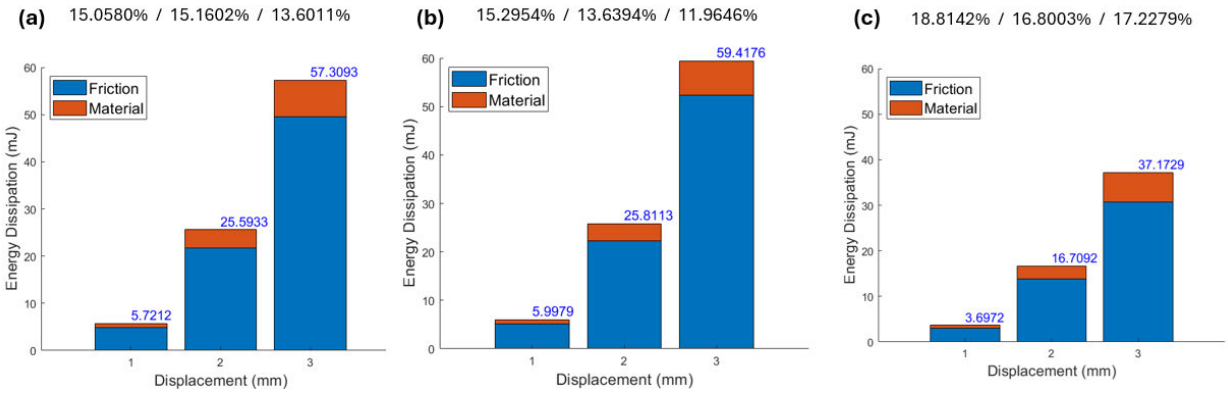

Figure 5.7. Ratio of internal energy dissipation to total energy dissipation, indicated by the orange bars. (a) FE simulation of conventional model. (b) FE simulation of re-entrant model. (c) Theoretical model. The three percentage numbers at the top indicate the share of internal energy dissipation at displacements of 1 mm, 2 mm, and 3 mm, respectively. The numbers at the top of each bar, meanwhile, refer to the total energy dissipation.

5.3.5 Comparing energy dissipation quantity between the CPE HG100 model and the TPU 95A model

In a previous study in Chapter 4, the energy dissipation of frictional metamaterial unit cells of similar design but constructed from a comparatively stiff material with negligible internal

damping was evaluated through calculations and experiments. The dissipative metamaterial unit presented here makes use of the comparatively soft TPU 95A's hyperelastic aspects to increase the amplitude of sliding motion between the frictional contact surface, and its viscoelasticity to increase the material's contribution to total energy dissipation. Results of an experimental dissipative performance comparison with both the conventional hexagonal and re-entrant versions of the previously studied metamaterial single unit cells, under equivalent compressive strains, are presented in Table 5.6.

FE simulation results indicated a similar behaviour. From Figure 5.8 and Table 5.7, the energy dissipation of the unit cell made of TPU 95A is one order of magnitude lower than that of the unit cell made of CPE HG100.

Table 5.6. Experimentally measured energy dissipation per loading cycle of the metamaterial single unit cells and that obtained previously for geometrically similar stiffer unit cells constructed from CPE HG100, a linearly elastic polymer with minimal material damping.

Max Effective Strain (mm/mm)	Experimental result of TPU 95A (Conventional, Average)	Experimental result of TPU 95A (Re-entrant, Average)	Experimental result of CPE HG100 (Conventional, Average)	Experimental result of CPE HG100 (Re-entrant, Average)
0.0156	4.497 mJ	5.896 mJ	59.52 mJ	71.097 mJ
0.0312	23.337 mJ	26.668 mJ	302.04 mJ	332.582 mJ
0.0467	59.402 mJ	60.589 mJ	677.22 mJ	688.12 mJ

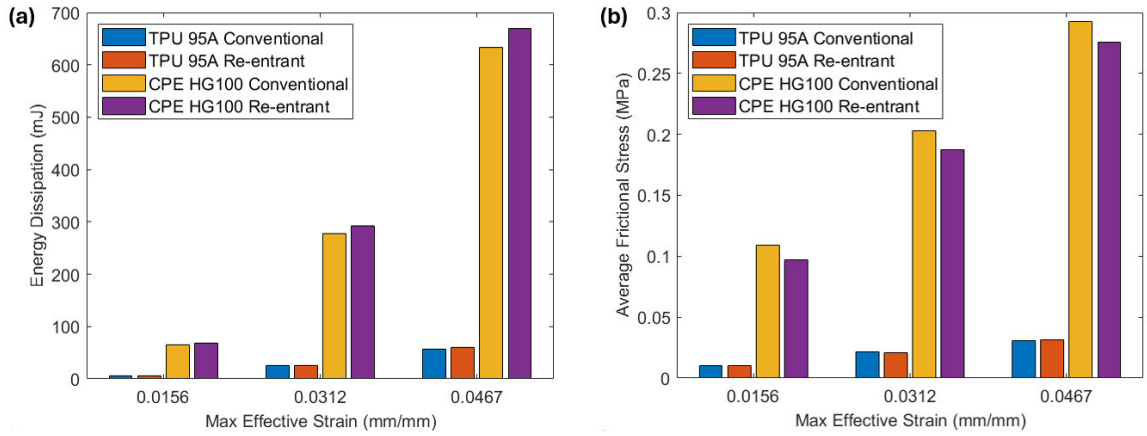

Figure 5.8. Comparison of single unit cells of mechanical metamaterials that use hyperelastic and viscoelastic behaviour versus those that are limited to stiffer, linearly elastic response in terms of (a) energy dissipation and (b) average frictional stress.

Table 5.7. FE simulation model's energy dissipation per loading cycle of the metamaterial single unit cells shown in Figure 5.3, and that obtained previously for geometrically similar stiffer unit cells constructed from CPE HG100, a linearly elastic polymer with minimal material damping. These data are visualised in the bar graphs in Figure 5.8a.

Max Effective Strain (mm/mm)	FE simulation result of TPU 95A (Conventional)	FE simulation result of TPU 95A (Re-entrant)	FE simulation result of CPE HG100 (Conventional)	FE simulation result of CPE HG100 (Re-entrant)
0.0156	5.72 mJ	5.98 mJ	64.98 mJ	68.81 mJ
0.0312	25.59 mJ	25.81 mJ	276.86 mJ	293.03 mJ
0.0467	57.31 mJ	59.42 mJ	632.99 mJ	669.02 mJ
0.0779	211.11 mJ	214.55 mJ	-	-
0.1090	374.38 mJ	400. 84 mJ	-	-
0.1246	482.49 mJ	-	-	-

5.4. Discussion

It is clear from Figure 5.3 that for the single unit cell case there is good overall agreement between the experimental and simulated compression cycles for both conventional and re-entrant hexagonal frames. The areas within the measured and predicted hysteresis loops have similar values, generally within approximately 10% of each other, although there is a noticeable dependence on the amplitude of the compression cycle as well as the frame geometry. For the conventional hexagonal frame, the FE simulation yields a higher energy dissipation result than any of the tests at the lowest 1 mm amplitude, a situation that persists for the 2 mm cycle, but at the maximum amplitude of 3 mm the simulation result is within the test data range. For the re-entrant frame at any cycle amplitude the energy dissipation computed by the FE simulation is within or slightly below the range of values calculated from the test measurements for all cycle amplitudes. The difference in performance between the conventional and re-entrant frame is likely related to the difference in top and bottom surface lateral displacement constraints between simulations and experiments, as the main difference between these two frame geometries is their effective Poisson's ratio.

However, although the effective vertical stress versus strain curve from the FEA-based simulation tracked well against the experimentally derived data for much of the compression cycle, it consistently predicted a higher peak load near the end of the loading phase than was observed during testing, and in some cases also a slightly higher load during the inflection of the unloading

curve. These discrepancies were present in both frame configurations, though they appeared less significant in the re-entrant units.

A primary factor contributing to this divergence is likely the Mullins effect, also known as stress-softening, a well-documented phenomenon in thermoplastic polyurethanes (TPU) [152]. While its underlying mechanisms have been debated for decades [153], it is now generally understood to arise from microstructural damage and irreversible rearrangements of polymer chains, such as disentanglement and microcavity formation, which collectively reduce stiffness during repeated loading [154]. The three-parameter Mooney-Rivlin model applied in this work does not incorporate stress-softening or load-history effects and therefore cannot account for the influence of multiple loading cycles on the specimens, nor the pronounced contact pressures, frictional peaks within the central structure, or stress concentrations at frame corners.

Beyond the limitations of the material model, modelling choices and assumptions related to boundary conditions may have introduced additional artificially stiffening. The adoption of higher-order tetrahedral SOLID187 elements was necessary to accommodate the unit cell's intricate geometry, yet this choice can induce numerical stiffening when compared to the hexahedral SOLID 186 formulation. Although the reduced integration scheme of SOLID 187 is computationally efficient, it is less effective at resolving steep stress gradients near contact regions and corners, thereby exaggerating local stiffness. Nevertheless, the mesh convergence study **(Appendix N)** indicates that finer meshes, which nearly double the numbers of degrees of freedom, altered the peak force and total energy dissipation by only a few percent. Interestingly, this mesh refinement results in a small increase in peak force rather than a reduction, increasing the discrepancy between simulation and experiment. This outcome is attributed to the highly localised nature of the contact pressure distribution, with the finer mesh more precisely capturing the pressure peaks and stress concentrations in the model.

The replicated boundary conditions may also have played a role. In the simulations, the bottom surface of model was fixed, and a unidirectional displacement was imposed on the top face of the model. While these constraints were intended to mimic the experimental conditions, they may have restricted minor lateral motions and deformations that occur in the physical tests and reduce the test article's effective stiffness.

Additional contributing factors to the divergence between simulation and experiment are the discrepancies between the hyperelastic material model used in the FE simulation (Figure 5.2) and the more complex reality of TPU load-displacement response, in combination with the FE model's idealised representation of interface mechanics, particularly contact and friction between the blades and the columns, which fails to fully capture the influence of the 3D printed test article's

imperfections. The relative importance of these various contributing factors will require further investigation to improve simulation accuracy for future frictional metamaterial designs.

In contrast, the energy dissipation calculated using the frictional sliding theoretical model was around 30% lower, as can be seen in Figure 5.4, indicating that it does not fully capture the friction and internal damping observed in experiments or simulations. Examination of the contact pressure and frictional stress distributions in the simulation reveals that friction is highly concentrated around the lower edge of the contact surfaces. This is an important difference from the assumptions underpinning the theoretical model, which calculates contact and friction forces as an effective value evenly distributed over contact surfaces. Of course, while frictional stress concentrations may lead to higher energy dissipation performance, they also entail the risk of more critical and faster abrasion phenomena.

Conventional hexagonal and re-entrant structural frames cause the oblique side walls to bend when an external force is applied, resulting in effective energy absorption. These geometric single unit cell frames exhibit unique mechanical behaviour, with some regions possessing tension even under compression, as observed in Figure 5.5.

Given the good match between simulation and experiment obtained for the single unit cell, the FE methodology was applied to periodic metamaterials composed of these unit cells. To take advantage of the hyperelastic behaviour of TPU, the amplitude of the compression cycle was gradually extended to 7 mm for the re-entrant frame and 8 mm for the conventional hexagonal frame, the re-entrant frame being limited by contact between frame and central body at larger compression amplitudes. The resultant stress distributions in the periodic metamaterial's representative volume element (RVE) and the single unit cells are significantly different, particularly in the frame parts, as can be seen from Figures 5.6(a-b) and 5.6(d-e). Instead of frame bending being mostly concentrated around the corners as is evident in the single unit cell, with regions of tensile stress even under compression, there is now considerable bending and shear distributed over the entirety to the frame sides. The stresses in the periodic metamaterial's unit cell frame are generally more than twice as high due to the constraining effect of the surrounding cells and start to approach the magnitude of the sliding friction stresses, which also increases the importance of the material's internal damping contribution to total energy dissipation.

The increased effective compressive stiffness of the periodic metamaterial RVE is evident in Figures 5.6(c, f), with the peak force values at the end of the loading phase and the total energy dissipation being approximately 40% to 50% higher than those found for the corresponding single unit cell, regardless of applied displacements.

The material's internal energy dissipation was estimated as a percentage of the total energy

dissipation and was found to be approximately 11% to 15% for the FE simulations across all compression amplitude values for both the conventional hexagonal and re-entrant structures. For the theoretical model it was calculated to be around 16% to 18% which is fairly consistent with the simulation results. Overall, these results suggest that internal material damping is a useful but not a decisive contributor to the metamaterial's energy dissipation performance. However, the performance of this class of material is highly sensitive to the strain rate applied. In the present study, due to the limitations of the experimental apparatus, only quasi-static (1-10 mm/min) compression rates could be applied. A compression rate of 3mm/min was selected, which corresponds to an intermediate value within the range commonly reported for TPU in the literature [155, 156]. The available data indicates that rate changes within this regime will raise peak stresses and load-displacement curve slopes only by amounts in the range of 10-20%. Consequently, although some quantitative differences are expected, the qualitative trends and governing mechanisms of energy dissipation, particularly the interplay between structural friction and internal material damping, are not change significantly with different strain rates within this quasi-static range, and therefore the broad conclusions are not compromised. Large changes in material response would require increases in the strain rate of one or two orders of magnitude, which are beyond both the scope of this work and its potential applications.

Compared to previous work on linearly elastic metamaterials made of much stiffer materials with far lower internal damping, the energy dissipation derived from the experiments reported here is an order of magnitude lower, approximately 11 to 13 times lower at the same compression amplitude. The difference in energy dissipation is clearly due to the much lower Young's modulus of TPU 95A, which results in lower compression force and lower average frictional stress. However, the FE simulations show that when taking advantage of TPU's ability to withstand larger deformations by increasing the compression amplitude, the energy dissipation in the softer metamaterial reaches about $^3/_4$ of the stiff single unit cells with a conventional hexagonal frame. These larger displacements are not available to the stiffer metamaterial due to structural damage and failure. In conclusion, soft metamaterials with hyperelastic behaviour are particularly advantageous in applications where large deformations are expected, energy dissipation is required over a range of displacements, and structural failure must be avoided over long periods of use. Their unique mechanical properties, a combination of flexibility, energy absorption, and durability, can be utilised for industries such as shock-absorbing flooring, vibration control systems, soft robotics and prosthetics.

Comparisons with the most relevant studies from the past five years, summarised in Table 5.8, provide useful context for interpreting the present results. One key finding is that although the initial elastic modulus of TPU 95A is roughly 60 or more times lower than that of the materials

used in these previous works, which significantly impacts energy dissipation performance as discussed in section 5.3.5, the energy dissipation of the unit cell proposed here is considerably higher than that of corresponding single hexagonal cell in Garland *et. al.* [85] and the I-shaped cell in Lv *et. al*. [87]. Its performance is also broadly comparable to that of the re-entrant cell reported by Chen and Ma [157]. For the parrot beak-inspired configuration introduced by Hamzehei et. al. [125], single cell performance result values were not directly provided. However, when the total energy dissipation of their macro cylinders is divided by the number of cells, the values in the range of 17 to 91 mJ are obtained, significantly lower than those obtained in this study at 12.5% strain, despite the cylinder's larger 38% overall strain and higher Young's modulus.

The various frictional unit cell designs reviewed in Table 5.8 vary substantially in geometry. Nevertheless, the energy dissipation per unit volume of both the single unit cell and the metamaterial representative unit cell (RVE) presented here surpass that of three out of four of the referenced designs. Although the innovative re-entrant unit cell recently developed by Chen and Ma [157] achieves superior volumetric energy dissipation by a factor of two to five, its current configuration lacks the geometric symmetries necessary for periodicity, rendering it unsuitable as an RVE for a dissipative metamaterial. As is the case for the other referenced designs, the use of much stiffer material generates higher frictional stresses but limits deformation, so substantial frictional work is contingent upon buckling.

Taken together, these comparisons indicate that considerable opportunities for improvement in frictional metamaterials remain. Importantly, none of the unit cell concepts discussed here have been subjected to systematic mathematical optimization processes. Moreover, some of the designs appear to overlook critical considerations related to the transition from individual unit cells to the assembled metamaterial structure. The upper limits of energy dissipation performance remain unexplored, underscoring the need for further research to establish the full potential of friction-based dissipative mechanical metamaterials. Therefore, future work should focus on quantifying the relative roles of frictional and viscoelastic dissipation with higher precision, extending characterisation to a broader range of strain rates, and exploring scenarios involving higher loading rates and frequencies that are relevant for real-world applications.

Table 5.8. Comparison of energy dissipation per unit volume and key information of the models in the reference papers.

Unit	Nominal strain (%)	Young's modulus (MPa)	Peak force (N)	Energy dissipation per cycle (mJ)	Volume (cm^3)	Energy dissipation per unit volume (mJ/cm^3)	Loading rate (mm/min)
Single macro cell [85]	3	>1000	0.75	0.23 to 0.76	2.8	0.082 to 0.271	N/A
15-cell macro lattice [85]	3	>1000	135	2.57	42	0.061	N/A
48-cell macro cylinder [125]	38	900	>780	812.5 to 4375	367.6 to 395.8	2.1 to 11.6	5
Single cell [87]	8.85	1149	8	3 to 12	226.9	0.013 to 0.053	2
Single cell [157]	7	1000-1200	N/A	172.3 to 468.8	14.1 to 14.9	12.22 to 31.46	2
Single cell (test)	4.7	16	53	59.4	78.47	0.757	3
Single cell (FEA)	12.5	16	122	482.5	78.47	6.15	-
RVE cell (FEA)	12.5	16	173	646.6	174.56	3.70	-

5.5. Conclusion

This chapter proposes a dissipative nonlinear metamaterial that combines sliding friction and internal energy dissipation and examines its performance through theoretical analysis, finite element modelling, and compression testing of 3d-printed test specimens at slow loading rates. Both auxetic and non-auxetic versions of this metamaterial concept are considered. The test specimens are made by Fused Deposition Modelling (FDM) of a thermoplastic polyurethane (TPU 95A) that exhibits a combination of hyperelastic and viscoelastic behaviour, allowing the metamaterial to endure large deformations. The relative contribution of different energy dissipation mechanisms was assessed and the overall dissipation performance was compared with that of a linearly elastic equivalent.

When compared to the finite element modelling results, the experimentally measured force-displacement cycles exhibited some discrepancies, with a more gradual stress increase at the end of the loading step. Nevertheless, the overall hysteresis loop shape and total energy dissipation quantity show a good correlation between simulations and experiments. And a comparison of the specific ratios of the internal energy dissipation of the theoretical and FE simulation models indicates that they are generally similar and consistent.

Unlike almost all static and dynamic metamaterials, whose functionality is typically reliant on linear mechanisms, the energy-dissipating unit cells presented here represent a distinct class of mechanical metamaterials whose very existence and functionality are predicated on nonlinearity. This essential nonlinearity arises from multiple distinct and interacting sources. One of the most important of these is friction, as frictional nonlinearity generates the hysteresis loop and governs its shape, mainly through evolving contact pressure and sliding area in the simulations, although microscale stick–slip may also play a role in the experiments. Another important nonlinearity is the geometric or kinematic nonlinearity that arises under larger strain conditions and can enhance the metamaterial's non-affine deformation patterns, sequentially activate different contact zones, and broaden the hysteresis region. Finally, depending on the choice of materials, material nonlinearity can also play a role. Viscolelasticity contributes additional dissipation, which was observed in experiments, although it was not explicitly captured in the finite model, and hyperelasticity enables large deformations, allowing the frictional stresses to perform considerably more work that significantly increases the total dissipation.

A distinguishing feature of the proposed metamaterial is its ability to repeatably withstand large deformation which enhances its damage tolerance allowing it to reliably dissipate energy in situations where a wide range of load cycle amplitudes could be encountered, including high amplitude pulses or transients, or low-velocity impacts.

Chapter 6 is embargoed until the 22nd of September, 2026

Chapter 6 is embargoed until the 22nd of September, 2026

Chapter 6 is embargoed until the 22nd of September, 2026

Chapter 6 is embargoed until the 22nd of September, 2026

Chapter 6 is embargoed until the 22nd of September, 2026

Chapter 6 is embargoed until the 22nd of September, 2026

Chapter 6 is embargoed until the 22nd of September, 2026

Chapter 6 is embargoed until the 22nd of September, 2026

Chapter 6 is embargoed until the 22nd of September, 2026

Chapter 6 is embargoed until the 22nd of September, 2026

Chapter 6 is embargoed until the 22nd of September, 2026

Chapter 6 is embargoed until the 22nd of September, 2026

Chapter 6 is embargoed until the 22nd of September, 2026

Chapter 6 is embargoed until the 22nd of September, 2026

Chapter 6 is embargoed until the 22nd of September, 2026

Chapter 6 is embargoed until the 22nd of September, 2026

Chapter 6 is embargoed until the 22nd of September, 2026

Chapter 6 is embargoed until the 22nd of September, 2026

Chapter 6 is embargoed until the 22nd of September, 2026

Chapter 6 is embargoed until the 22nd of September, 2026

Chapter 6 is embargoed until the 22nd of September, 2026

Chapter 6 is embargoed until the 22nd of September, 2026

Chapter 6 is embargoed until the 22nd of September, 2026

Chapter 6 is embargoed until the 22nd of September, 2026

Chapter 6 is embargoed until the 22nd of September, 2026

Chapter 6 is embargoed until the 22nd of September, 2026

Chapter 6 is embargoed until the 22nd of September, 2026

Chapter 6 is embargoed until the 22nd of September, 2026

Chapter 6 is embargoed until the 22nd of September, 2026

Chapter 6 is embargoed until the 22nd of September, 2026

Chapter 6 is embargoed until the 22nd of September, 2026

Chapter 6 is embargoed until the 22nd of September, 2026

CHAPTER 7: CONCLUSIONS AND FUTURE WORKS

As a unique characteristic of mechanical metamaterials, energy dissipation mainly based on the sliding friction was investigated through designing, simulating, manufacturing and experiments in this study. This chapter concisely summaries the research findings and insights, contributions of knowledge, limitations and challenges, and future works.

7.1 Conclusions

7.1.1. Key findings and insights

This study investigated a friction-based mechanical metamaterial composed of a hexagonal unit cell with internal blades and columns contact surfaces that dissipate energy through a sliding friction mechanism.

A key finding from the literature review is that while frictional mechanical metamaterials have been explored in prior studies, standardised design parameters and optimal geometries for efficient energy dissipation remain underdeveloped. This study contributes to filling that gap by systematically designing, simulating, fabricating, and experimentally validating frictional metamaterials.

Through iterative simulations and experimental validation, it was confirmed that frictional sliding between internal contact surfaces occurs as expected under external unidirectional perpendicular loading. Theoretical and simulation models provided insights into the mechanical behaviours of these metamaterials, although some discrepancies arose due to simplifications in theoretical modelling.

The study further revealed that different material choices significantly influence the metamaterial's energy dissipation performance. The TPU 95A-based metamaterials, representing nonlinear material properties, exhibited internal damping mechanical behaviour leading to modifications in the theoretical model and refined curve fitting through hyperelastic modelling in ANSYS Workbench. The findings highlight the importance of selecting appropriate material models to capture the complex mechanical response of frictional metamaterials accurately.

Moreover, the research explored variations in metasurface geometries and contact surface partitioning. The implementation of right-angled isosceles triangles, rectangles, and semi-elliptical patterns on the contact area of the unit cell structure demonstrated different loading-displacement responses. This suggests that optimising contact surface design can further enhance energy dissipation performance.

In summary, this study advances the understanding of frictional metamaterials by demonstrating

the combined effects of geometry, material properties, and frictional interactions. These insights contribute to the broader development of energy-dissipating metamaterials and provide a foundation for future work aimed at optimising their performance under real-world conditions where energy dissipation and shock mitigation are required.

7.1.2 Answering to research questions

RQ1 asked how the internal structure should be designed to maximise energy dissipation for the same unit volume. We went through iterative design and simulation work to address this and were able to design columns with pinwheel structure inside to maximise the contact area inside the same volume. This design, introduced in Chapter 3, was successful in achieving a wide hysteresis area in metamaterial fabrication and experiments using CPE HG100 and TPU 95A as unit cell constituent materials in Chapters 4 and 5, respectively.

RQ2 questioned how the applied metasurface on the metamaterial affects the energy dissipation and peak force. To answer this question, we applied right-angled isosceles triangles, rectangles, and semi-elliptical patterns to the contact surface of the metamaterial and were able to cross-validate the simulation and compression experiments to conclude that the energy dissipation and peak force values increased slightly due to the metasurfaces. Although we only focused on the development of metamaterials at the macroscopic scale owing to the limitations of the available equipment, these results explicitly show that the application of metasurfaces provides a rationale for the increase in contact area and subsequent increase in energy dissipation while using the same volume of constituent material, and may inspire future researchers who have access to 3D printers capable of fine and detailed fabrication.

RQ3 was a question about how to develop an FE simulation model to represent the properties of metamaterials using nonlinear soft materials, and a question about modifying the theoretical model to represent internal damping. We used various hyperelastic models in ANSYS Workbench to curve fit each of them and employed the Mooney-Rivlin 3rd order to develop the simulation model as it exhibited the best fit to the sample data. In order to avoid errors, the loading and unloading data of the sample blocks were registered separately and applied to the corresponding steps of the simulation model, which succeeded in representing the properties of TPU 95A, which has both hyperelastic and viscoelastic properties. A theoretical model for metamaterials manufactured using nonlinear soft materials is presented in Chapter 5 by adding an internal damping element from the formulation in Chapter 4 for models with linear properties.

7.2 Contribution

Creating novel designed geometries for frictional mechanical metamaterials: In Chapter 3, we proposed a new frictional mechanical metamaterial designed to assemble the central part of a

conventional hexagonal or re-entrant structure frame, the bottom body including four tapered pillars, and the top body that can be characterised as blade-like structure. The cross-section of each of the four tapered pillars is a combination of a quarter circle and a quarter circular spandrel, which maximises the contact area, leading to better energy dissipation than a triangular or semi-circular cross-section structure with the same volume. This metamaterial undergoes non-affine deformations when external load is applied. This is because all structural parts of the metamaterial are not deformed uniformly. Displacement contour plots highlight that the frictional contact zones shift more than other parts of the structure and this amplification of motions results in amplification of energy dissipation. While classical frictional systems rely on a single interface, like a flat brake pad, the proposed metamaterial uses internally structured contact surfaces and non-affine deformation to activate multiple local frictional interactions**.** These interactions do not occur simultaneously across the entire surface, but rather sequentially or in localized stress zones, as shown in the simulation stress contours (Fig 6.16). This non-uniform activation is a direct result of the metamaterial's geometry and internal constraints. The novel design contributes to broadening the horizon of field applicability of frictional metamaterials and may inspire other researchers who wish to study tribological metamaterials in the future.

Proposal of the angle difference between contact surfaces as a representative parameterised design variable

Our FE simulation results showed that the distribution of contact stress varies depending on the angle between contact surfaces, indicating that designed geometry can be deliberately tuned to control where and how friction is activated. Among many possible geometric variables such as pillar tapering or surface curvature, the angle difference was chosen in this study as a representative parameter because it directly governs the sequential activation of contact zones under loading. While we do not claim that the 3-degree angular difference used here is universally optimal, this case demonstrates that treating the angle between contact surfaces as a tuneable design variable enables controlled redistribution of frictional stress, thereby providing a pathway for standardising parameterisation in frictional metamaterial design.

Theoretical, simulation, and experimental demonstration of frictional metamaterials with linear properties: In Chapter 4, the unit cell specimens that will make up the frictional metamaterial with linear properties were fabricated and the hysteretic loop region of the FE simulation closely matched the compression experiments performed. This allowed us to validate the energy dissipation ability of the fabricated material and provide confidence in its future field applicability.

A new simulation approach for analysing a material that is both hyperelastic and

viscoelastic is presented: When the simulation process to investigate the energy dissipation performance of unit cell specimens manufactured using TPU 95A, a nonlinear soft material, the hyperelastic model in ANSYS Workbench alone could not capture the discrepancy of the curve roots between loading and unloading of the actual sample experiment. To compensate for this, the loading data and unloading data of the sample experiment were separated, and the loading data was applied to the loading step of the simulation and the unloading data was applied to the unloading step. This was achieved by entering a command to toggle the existing loading data with the unloading data when switching from a loading step to an unloading step. In chapter 5, the results of the simulation model and the experimental model made of TPU 95A were cross-validated to ensure the reliability of the developed model. The theoretical and simulation models were used to investigate the contribution of internal damping to the total energy dissipation, and the results from both models were similar, providing continuity. This series of studies will be useful in the future to predict the mechanical behaviour of frictional metamaterial made of materials with nonlinear properties.

Application of metasurfaces to contact surfaces of frictional metamaterials and the expansion possibility of applying various mechanical properties of the contact surfaces: At the macroscopic scale, by applying patterns to the sliding contact surfaces, it is possible to expand the contact area under the same volume condition, and this finding provides an inspiring point for maximising energy dissipation under limited fabrication material conditions. Designed models have been demonstrated through simulation and compression tests to improve energy dissipation performance. Furthermore, by proposing and demonstrating a design that allows the assembly of parts made of different materials by partitioning some areas of the contact surface, it offers the possibility of tuning the unique energy dissipation behaviour in response to displacement through the combination of different constituent materials in the future.

7.3 Limitations and challenges

The range of research questions addressed was to develop theoretical and simulation models, and to demonstrate that 3D frictional metamaterials and various 2D metasurfaces geometries can be programmed and tuned for enhanced energy dissipation capabilities using experiments and design iterations. This was achieved through the construction of unit cell systems with internal sliding tribological surfaces in the frame of conventional honeycomb and re-entrant structures. However, several limitations and challenges were encountered that affected both the experimental and theoretical aspects of the research. These constraints, primarily related to manufacturing limitations and computational complexities, are discussed below.

Limited loading rate capabilities for compression experiments: Due to experimental

constraints, only slow quasi-static loading rates were available for compression testing. The subjected loading rate was restricted to 3mm/min because the testing procedure required manual intervention to halt the loading process. This limitation precluded the investigation of dynamic or high-speed loading effects, which could potentially influence the frictional energy dissipation behaviour. Consequently, the results obtained may not fully capture the response of the metamaterial under more realistic or extreme loading rate conditions that occur in practical applications.

Constraints in displacement measurement: The study relied on the displacement measurements provided by the universal testing machine (UTM) equipped with a load cell. However, potential inaccuracies may exist due to minor discrepancies between the actual displacement experienced on the metamaterial and the displacement recorded by the UTM. This gap could arise from system compliance, sensor inaccuracies, or mechanical deformations within the machine itself. Ideally, a more precise measurement technique, such as video tracking of the deformation process combined with image processing software, should have been employed to obtain a more accurate representation of the actual displacement. However, the approach was not implemented in the current study owing to the restricted accessibility of equipment, introducing potential measurement uncertainties.

Constraints of accessibility for high-resolution 3D printers and other equipment: One of the primary challenges faced during this study was the limitation imposed by the available AM technology. The only 3D printer accessible in the laboratory was a low-cost commercial model utilising the FDM method. The inherent limitations of this technology, including layer adhesion issues and resolution constraints, restricted the precision and quality of the fabricated specimens. Specifically, the 3D printer's nozzle diameter of 0.2 mm posed significant difficulties in achieving fine geometrical details, thereby limiting the resolution of the manufactured metamaterial unit cells including metasurfaces. This restriction directly impacted the accuracy of the experimental models compared to their idealised theoretical counterparts, potentially introducing minor inconsistencies between the experimental and simulated results. We also wanted to experiment under multiple loading-unloading cycle conditions instead of a single loading-unloading cycle, but this was also hampered by the inaccessibility of the fatigue testing machine.

Unsophisticated theoretical model: The theoretical model developed in this research provided a foundational framework for understanding the energy dissipation characteristics of the frictional metamaterials. However, the model exhibited some limitations in capturing the full complexity of the system. Specifically, it yielded lower energy dissipation values compared to both experimental and FEA results. This disparity suggests that additional factors, such as micro-scale interactions, and residual stresses, may not have been fully accounted for in the theoretical

framework. A more sophisticated modelling approach incorporating additional factors could improve predictive accuracy and alignment with experimental observations.

Challenges in implementing patterns on curved contact surfaces: Another major challenge encountered was the difficulty in implementing intricate patterns on curved contact surfaces. An effort was made to integrate patterned structures on the contact surfaces of metamaterials in Chapters 4 and 5, featuring an internal pinwheel configuration. However, the high geometric complexity of these designs led to meshing difficulties, often resulting in non-convergence errors during FE simulations. This limitation necessitated slight modifications to the internal structure of the metamaterial unit cell, ultimately requiring a transition to flat contact surfaces for the successful application of metasurfaces. Although this modification enabled the simulation to proceed, it may have influenced the overall contact area and led to less energy dissipation than the metamaterial that holds the curved surfaces.

7.4 Future works

The previous limitations and challenges of the study pointed out a number of areas that need more investigation to support the finding, gain a deeper understanding of the system involved or advance the system for use in other contexts.

Further work on the theoretical model: In Chapters 4 and 5, the energy dissipation of the theoretical model was found to be relatively low compared to the results of the simulation and experimental models. This highlights the fact that the theoretical model does not fully reflect the mechanical behaviour of real experiments and simulations, where only a few areas of the contact surface have a strong stress concentration. It is possible that the hysteresis region extracted from the actual compression test results is not solely the result of sliding friction inside the unit cell, but there are additional intervening factors. Future research will involve adding other undiscovered factors that affect the hysteresis region to the theoretical model.

Cyclic testing: There is a need for cyclic testing (multi-cycle compression testing) to be carried out in the future to ensure the reusability and repeatability of the tribological metamaterial. Throughout the previous concepts from the other researchers, a number of multi-cyclic tests have been done to validate their model's long lifespan under extreme conditions. Unfortunately, due to the limitation of accessibility to the test machine, the newly suggested model in this study only be focused on simple situations like a single cycle compression. In order to perform cyclic test simulation from ANSYS Workbench, a prior experiment also should be completed to gain an S-N curve, indicating the number of cycles (N) to failure within a given stress (S), to define the behaviour of constituent material. Although the single-cycle compression tests confirmed that no permanent deformation or rupture occurred, further research in multi-cycle compression testing

area will provide the opportunities to move beyond simple single shock situations to ensure or even improve design performance under environmental conditions where sustained impacts are inflicted.

Fabrication and experimentation of metamaterials composed of multiple unit cells: In Chapter 4, we focused our study on FE simulation results using CAD files of metamaterials with 8-, 11-, and 13-unit cells transferred to ANSYS Workbench. Unlike the design works in Chapter 3, where the concept was for the three parts to be assembled to form a single unit cell, the bulk metamaterial is intended to be fabricated as a single form that would inevitably be connected at the time of fabrication due to its structure. However, in this case, the narrow spaces that exist between the contacting surfaces should be able to avoid the failures caused by the melting of the filaments and pressing them together during the fabrication process. The 3D printer employed in this research is a relatively inexpensive commercially available machine and is not suitable for high quality. This was deemed to be a prominent reason for the failure to achieve sufficient hysteresis loop area in the reproduction of the design proposed by other researchers, although there are various other potential reasons. Even though the simulation work using the RVE models provided a good understanding of the energy dissipation capability of multiple unit cells, further compression experiments of a model consisting of multiple unit cells would be helpful to compare and analyse the experimental and simulation results to demonstrate the validity of the constraint equations applied in the single unit cell simulation.

Applying a variety of materials for metamaterial fabrication: The study focused on two filaments for fabricating the specimens - CPE HG100 and TPU 95A. Unit samples fabricated using each of the two materials were successfully demonstrated, but both materials have limitations if the proposed specimens are to be used in industry. CPE HG100 and TPU 95A melted and extruded adequately at nozzle temperatures set at approximately 270 ℃ and 230 ℃, respectively, suggesting that the application of metamaterials manufactured using these materials as components in the industry field at higher temperatures is restricted. Metamaterials made from the filaments used above may be suitable for certain industries such as protect hats and footwear, which are typically used in room temperature environments, or for vibration absorbing structures in buildings and soft robotics. However, properties such as the relatively low melting point of the material limit their use in aerospace applications, where they may be exposed to extremely high temperatures, and should motivate further exploration of the possibility of manufacturing frictional mechanical metamaterials using other materials with higher melting points. Further research throughout the fabrication of frictional metamaterials via additive manufacturing using a wider variety of materials, such as ceramics or polymers, may increase the potential for applying the proposed metamaterial concepts to environments such as more severe shocks or temperature

extremes.

Higher loading rate compression tests: One of the Future studies will explore higher loading rate compression tests to better understand how frictional dissipation mechanisms behave under dynamic conditions. Experimental results from dynamic loading could be compared with rate-dependent friction models, such as velocity-dependent Coulomb friction, to refine predictive models. Investigating the effect of higher loading rates will provide valuable insights into the potential of frictional metamaterials for high-performance energy dissipation applications.

Applying metasurfaces on the curved contact surfaces: Future work should focus on developing robust modelling techniques that enable accurate meshing and simulation of patterned curved surfaces. Potential solutions include using advanced meshing algorithms, or adaptive re-meshing techniques that better capture contact interactions. Additionally, experimental validation of metasurfaces on curved contacts should be pursued to determine whether the increased contact complexity leads to improved energy dissipation.

Future works to address the limitations could expand the design possibilities for frictional metamaterials, enabling more efficient and adaptable energy dissipation mechanisms tailored to specific engineering applications.

REFERENCES

1. Parveen, K., *Metamaterials: Types, applications, development, and future scope.* Intemational Journal of Advance Research, Ideas and Innovations in Technology, 2018.
2. Veselago, V.G., *Electrodynamics of substances with simultaneously negative and.* Usp. fiz. nauk, 1967. **92**(7): p. 517.
3. Kumar, R., M. Kumar, J.S. Chohan, and S. Kumar, *Overview on metamaterial: History, types and applications.* Materials Today: Proceedings, 2022. **56**: p. 3016-3024.
4. Pendry, J.B., A.J. Holden, D.J. Robbins, and W. Stewart, *Magnetism from conductors and enhanced nonlinear phenomena.* IEEE transactions on microwave theory and techniques, 1999. **47**(11): p. 2075-2084.
5. Smith, D.R., W.J. Padilla, D. Vier, S.C. Nemat-Nasser, and S. Schultz, *Composite medium with simultaneously negative permeability and permittivity.* Physical review letters, 2000. **84**(18): p. 4184.
6. Shelby, R.A., D.R. Smith, and S. Schultz, *Experimental verification of a negative index of refraction.* science, 2001. **292**(5514): p. 77-79.
7. Smith, D.R., J.J. Mock, A. Starr, and D. Schurig, *Gradient index metamaterials.* Physical Review E, 2005. **71**(3): p. 036609.
8. Leonhardt, U., *Optical conformal mapping.* science, 2006. **312**(5781): p. 1777-1780.
9. Pendry, J.B., D. Schurig, and D.R. Smith, *Controlling electromagnetic fields.* science, 2006. **312**(5781): p. 1780-1782.
10. Ergin, T., N. Stenger, P. Brenner, J.B. Pendry, and M. Wegener, *Three-dimensional invisibility cloak at optical wavelengths.* science, 2010. **328**(5976): p. 337-339.
11. Yin, M., A. Petrusek, J. Seda, and J. Wolinska, *Fine-scale temporal and spatial variation of taxon and clonal structure in the Daphnia longispina hybrid complex in heterogeneous environments.* BMC Evolutionary Biology, 2012. **12**: p. 1-12.
12. Liu, C.R., J.H. Wu, F. Ma, X. Chen, and Z. Yang, *A thin multi-order Helmholtz metamaterial with perfect broadband acoustic absorption.* Applied Physics Express, 2019. **12**(8): p. 084002.
13. Yang, M., S. Chen, C. Fu, and P. Sheng, *Optimal sound-absorbing structures.* Materials Horizons, 2017. **4**(4): p. 673-680.
14. Zhang, B. and H. Zirath, *Metallic 3-D printed rectangular waveguides for millimeter-wave applications.* IEEE Transactions on Components, Packaging and Manufacturing Technology, 2016. **6**(5): p. 796-804.
15. Bückmann, T., M. Thiel, M. Kadic, R. Schittny, and M. Wegener, *An elasto-mechanical unfeelability cloak made of pentamode metamaterials.* Nature communications, 2014. **5**(1): p. 4130.
16. Goldsberry, B.M. and M.R. Haberman, *Negative stiffness honeycombs as tunable elastic*

metamaterials. Journal of Applied Physics, 2018. **123**(9).

17. Klatt, T. and M.R. Haberman, *A nonlinear negative stiffness metamaterial unit cell and small-on-large multiscale material model.* Journal of Applied Physics, 2013. **114**(3).
18. Ren, C., D. Yang, and H. Qin, *Mechanical performance of multidirectional buckling-based negative stiffness metamaterials: an analytical and numerical study.* Materials, 2018. **11**(7): p. 1078.
19. Tan, X., S. Chen, B. Wang, J. Tang, L. Wang, S. Zhu, K. Yao, and P. Xu, *Real-time tunable negative stiffness mechanical metamaterial.* Extreme Mechanics Letters, 2020. **41**: p. 100990.
20. Litchinitser, N.M., I.R. Gabitov, A.I. Maimistov, and V.M. Shalaev, *Negative refractive index metamaterials in optics.* Progress in Optics, 2008. **51**: p. 1-67.
21. Padilla, W.J., D.N. Basov, and D.R. Smith, *Negative refractive index metamaterials.* Materials today, 2006. **9**(7-8): p. 28-35.
22. Zhang, S., Y.-S. Park, J. Li, X. Lu, W. Zhang, and X. Zhang, *Negative refractive index in chiral metamaterials.* Physical review letters, 2009. **102**(2): p. 023901.
23. Hou, X. and V.V. Silberschmidt, *Metamaterials with negative poisson's ratio: A review of mechanical properties and deformation mechanisms.* Mechanics of Advanced Materials: Analysis of Properties and Performance, 2015: p. 155-179.
24. Mizzi, L., K.M. Azzopardi, D. Attard, J.N. Grima, and R. Gatt, *Auxetic metamaterials exhibiting giant negative Poisson's ratios.* physica status solidi (RRL)–Rapid Research Letters, 2015. **9**(7): p. 425-430.
25. Mizzi, L., E. Mahdi, K. Titov, R. Gatt, D. Attard, K.E. Evans, J.N. Grima, and J.-C. Tan, *Mechanical metamaterials with star-shaped pores exhibiting negative and zero Poisson's ratio.* Materials & Design, 2018. **146**: p. 28-37.
26. Wang, H., Y. Zhang, W. Lin, and Q.-H. Qin, *A novel two-dimensional mechanical metamaterial with negative Poisson's ratio.* Computational Materials Science, 2020. **171**: p. 109232.
27. Yang, H. and L. Ma, *Multi-stable mechanical metamaterials with shape-reconfiguration and zero Poisson's ratio.* Materials & Design, 2018. **152**: p. 181-190.
28. Walia, S., C.M. Shah, P. Gutruf, H. Nili, D.R. Chowdhury, W. Withayachumnankul, M. Bhaskaran, and S. Sriram, *Flexible metasurfaces and metamaterials: A review of materials and fabrication processes at micro-and nano-scales.* Applied Physics Reviews, 2015. **2**(1).
29. Xiao, S., T. Wang, T. Liu, C. Zhou, X. Jiang, and J. Zhang, *Active metamaterials and metadevices: a review.* Journal of Physics D: Applied Physics, 2020. **53**(50): p. 503002.
30. Raghavan, S. and V. Rajeshkumar, *An overview of metamaterials in biomedical applications.* Prog. Electromagn. Res, 2013. **25**: p. 369.
31. Deery, D., L. Flanagan, G. O'Brien, H.J. Rice, and J. Kennedy. *Efficient modelling of acoustic metamaterials for the performance enhancement of an automotive silencer*.

in *Acoustics*. 2022. MDPI.

32. Sato, K., S.H. Yonak, T. Nomura, S.-i. Matsuzawa, and H. Iizuka. *Metamaterials for automotive applications*. in *2007 IEEE Antennas and Propagation Society International Symposium*. 2007. IEEE.
33. Palma, G., H. Mao, L. Burghignoli, P. Göransson, and U. Iemma, *Acoustic metamaterials in aeronautics.* Applied Sciences, 2018. **8**(6): p. 971.
34. Geng, Z., X. Zhang, Z. Fan, X. Lv, and H. Chen, *A route to terahertz metamaterial biosensor integrated with microfluidics for liver cancer biomarker testing in early stage.* Scientific reports, 2017. **7**(1): p. 16378.
35. Kabashin, A.V., P. Evans, S. Pastkovsky, W. Hendren, G.A. Wurtz, R. Atkinson, R. Pollard, V.A. Podolskiy, and A.V. Zayats, *Plasmonic nanorod metamaterials for biosensing.* Nature materials, 2009. **8**(11): p. 867-871.
36. Cummer, S.A., J. Christensen, and A. Alù, *Controlling sound with acoustic metamaterials.* Nature Reviews Materials, 2016. **1**(3): p. 1-13.
37. Gao, N., Z. Zhang, J. Deng, X. Guo, B. Cheng, and H. Hou, *Acoustic metamaterials for noise reduction: a review.* Advanced Materials Technologies, 2022. **7**(6): p. 2100698.
38. Audoly, C., *Acoustic metamaterials and underwater acoustics applications.* Fundamentals and Applications of Acoustic Metamaterials: From Seismic to Radio Frequency, 2019. **1**: p. 263-285.
39. Zhu, Z., N. Hu, J. Wu, W. Li, J. Zhao, M. Wang, F. Zeng, H. Dai, and Y. Zheng, *A review of underwater acoustic metamaterials for underwater acoustic equipment.* Frontiers in Physics, 2022. **10**: p. 1296.
40. Chen, Z., B. Guo, Y. Yang, and C. Cheng, *Metamaterials-based enhanced energy harvesting: A review.* Physica B: Condensed Matter, 2014. **438**: p. 1-8.
41. Xu, X., Q. Wu, Y. Pang, Y. Cao, Y. Fang, G. Huang, and C. Cao, *Multifunctional metamaterials for energy harvesting and vibration control.* Advanced Functional Materials, 2022. **32**(7): p. 2107896.
42. Brûlé, S., S. Enoch, and S. Guenneau, *Emergence of seismic metamaterials: Current state and future perspectives.* Physics Letters A, 2020. **384**(1): p. 126034.
43. Mu, D., H. Shu, L. Zhao, and S. An, *A review of research on seismic metamaterials.* Advanced Engineering Materials, 2020. **22**(4): p. 1901148.
44. Zhao, Y.-j., B.-c. Zhou, Z.-k. Zhang, R. Zhang, and B.-y. Li, *A compact tunable metamaterial filter based on split-ring resonators.* Optoelectronics Letters, 2017. **13**(2): p. 120-122.
45. Kumar, P., T. Ali, and M.M. Pai, *Electromagnetic metamaterials: A new paradigm of antenna design.* IEEE Access, 2021. **9**: p. 18722-18751.
46. Fan, J., L. Zhang, S. Wei, Z. Zhang, S.-K. Choi, B. Song, and Y. Shi, *A review of additive manufacturing of metamaterials and developing trends.* Materials Today, 2021. **50**: p. 303-328.

47. Wang, H., Y. Lyu, S. Bosiakov, H. Zhu, and Y. Ren, *A review on the mechanical metamaterials and their applications in the field of biomedical engineering.* Frontiers in Materials, 2023. **10**.
48. Chen, X., J. Moughames, Q. Ji, J.A.I. Martínez, H. Tan, G. Ulliac, V. Laude, and M. Kadic, *3D lightweight mechanical metamaterial with nearly isotropic inelastic large deformation response.* Journal of the Mechanics and Physics of Solids, 2022. **169**: p. 105057.
49. Yang, K., L. Rao, L. Hu, F. Pan, Q. Yin, and Y. Chen, *Flexible, efficient and adaptive modular impact-resistant metamaterials.* International Journal of Mechanical Sciences, 2023. **239**: p. 107893.
50. Kolken, H.M. and A. Zadpoor, *Auxetic mechanical metamaterials.* RSC advances, 2017. **7**(9): p. 5111-5129.
51. Balan, M., J. Mertens, and M.R. Bahubalendruni, *Auxetic mechanical metamaterials and their futuristic developments: A state-of-art review.* Materials Today Communications, 2023. **34**: p. 105285.
52. Tomita, S., K. Shimanuki, S. Oyama, H. Nishigaki, T. Nakagawa, M. Tsutsui, Y. Emura, M. Chino, H. Tanaka, and Y. Itou, *Transition of deformation modes from bending to auxetic compression in origami-based metamaterials for head protection from impact.* Scientific Reports, 2023. **13**(1): p. 12221.
53. Bauer, J., L.R. Meza, T.A. Schaedler, R. Schwaiger, X. Zheng, and L. Valdevit, *Nanolattices: an emerging class of mechanical metamaterials.* Advanced Materials, 2017. **29**(40): p. 1701850.
54. Jiang, Y. and Q. Wang, *Highly-stretchable 3D-architected mechanical metamaterials.* Scientific reports, 2016. **6**(1): p. 34147.
55. Fang, H., S.C.A. Chu, Y. Xia, and K.W. Wang, *Programmable self-locking origami mechanical metamaterials.* Advanced Materials, 2018. **30**(15): p. 1706311.
56. Neville, R.M., F. Scarpa, and A. Pirrera, *Shape morphing Kirigami mechanical metamaterials.* Scientific reports, 2016. **6**(1): p. 31067.
57. Zhai, Z., L. Wu, and H. Jiang, *Mechanical metamaterials based on origami and kirigami.* Applied Physics Reviews, 2021. **8**(4).
58. Messner, M.C., *Optimal lattice-structured materials.* Journal of the Mechanics and Physics of Solids, 2016. **96**: p. 162-183.
59. Bertoldi, K., V. Vitelli, J. Christensen, and M. Van Hecke, *Flexible mechanical metamaterials.* Nature Reviews Materials, 2017. **2**(11): p. 1-11.
60. Ingrole, A.A., *Auxetic and hybrid structure designs and advanced manufacturing study for energy absorption improvements*. 2018, The Florida State University.
61. Hwang, D.-G. and M.D. Bartlett, *Tunable mechanical metamaterials through hybrid kirigami structures.* Scientific reports, 2018. **8**(1): p. 3378.
62. Yang, H. and L. Ma, *1D to 3D multi-stable architected materials with zero Poisson's*

ratio and controllable thermal expansion. Materials & Design, 2020. **188**: p. 108430.

63. Yuan, C., X. Mu, C.K. Dunn, J. Haidar, T. Wang, and H. Jerry Qi, *Thermomechanically triggered two-stage pattern switching of 2D lattices for adaptive structures.* Advanced Functional Materials, 2018. **28**(18): p. 1705727.
64. Chen, Y. and L. Jin, *Geometric role in designing pneumatically actuated pattern-transforming metamaterials.* Extreme Mechanics Letters, 2018. **23**: p. 55-66.
65. Jackson, J.A., M.C. Messner, N.A. Dudukovic, W.L. Smith, L. Bekker, B. Moran, A.M. Golobic, A.J. Pascall, E.B. Duoss, and K.J. Loh, *Field responsive mechanical metamaterials.* Science advances, 2018. **4**(12): p. eaau6419.
66. Montgomery, S.M., S. Wu, X. Kuang, C.D. Armstrong, C. Zemelka, Q. Ze, R. Zhang, R. Zhao, and H.J. Qi, *Magneto-mechanical metamaterials with widely tunable mechanical properties and acoustic bandgaps.* Advanced Functional Materials, 2021. **31**(3): p. 2005319.
67. Wang, L.-C., W.-L. Song, and D. Fang, *Twistable origami and kirigami: from structure-guided smartness to mechanical energy storage.* ACS applied materials & interfaces, 2018. **11**(3): p. 3450-3458.
68. Wang, L.C., W.L. Song, Y.J. Zhang, M.J. Qu, Z. Zhao, M. Chen, Y. Yang, H. Chen, and D. Fang, *Active reconfigurable tristable square-twist origami.* Advanced Functional Materials, 2020. **30**(13): p. 1909087.
69. Li, C., Z.-K. Peng, and Q. He, *Stimuli-responsive metamaterials with information-driven elastodynamics programming.* Matter, 2022. **5**(3): p. 988-1003.
70. Gupta, A., R. Sharma, A. Thakur, and P. Gulia, *Metamaterial foundation for seismic wave attenuation for low and wide frequency band.* Scientific Reports, 2023. **13**(1): p. 2293.
71. Kacin, S., M. Ozturk, U.K. Sevim, B.A. Mert, Z. Ozer, O. Akgol, E. Unal, and M. Karaaslan, *Seismic metamaterials for low-frequency mechanical wave attenuation.* Natural Hazards, 2021. **107**: p. 213-229.
72. Shim, J., C. Perdigou, E.R. Chen, K. Bertoldi, and P.M. Reis, *Buckling-induced encapsulation of structured elastic shells under pressure.* Proceedings of the National Academy of Sciences, 2012. **109**(16): p. 5978-5983.
73. Reye, G., X. Huang, L.M. Haupt, R.J. Murphy, J.J. Northey, E.W. Thompson, K.I. Momot, and H.J. Hugo, *Mechanical Pressure Driving Proteoglycan Expression in Mammographic Density: a Self-perpetuating Cycle?* Journal of Mammary Gland Biology and Neoplasia, 2021. **26**(3): p. 277-296.
74. Guan, Q., M. Lu, X. Wang, and C. Jiang, *Solid dynamic models for analysis of stress and strain in human hearts.* Computational and Mathematical Methods in Medicine, 2012. **2012**.
75. Greaves, G.N., A.L. Greer, R.S. Lakes, and T. Rouxel, *Poisson's ratio and modern materials.* Nature materials, 2011. **10**(11): p. 823-837.

76. Yu, X., J. Zhou, H. Liang, Z. Jiang, and L. Wu, *Mechanical metamaterials associated with stiffness, rigidity and compressibility: A brief review.* Progress in Materials Science, 2018. **94**: p. 114-173.
77. Ren, X., R. Das, P. Tran, T.D. Ngo, and Y.M. Xie, *Auxetic metamaterials and structures: a review.* Smart materials and structures, 2018. **27**(2): p. 023001.
78. Argatov, I.I., R. Guinovart-Díaz, and F.J. Sabina, *On local indentation and impact compliance of isotropic auxetic materials from the continuum mechanics viewpoint.* International Journal of Engineering Science, 2012. **54**: p. 42-57.
79. Bohara, R.P., S. Linforth, T. Nguyen, A. Ghazlan, and T. Ngo, *Anti-blast and -impact performances of auxetic structures: A review of structures, materials, methods, and fabrications.* Engineering Structures, 2023. **276**: p. 115377.
80. Coenen, V. and K. Alderson, *Mechanisms of failure in the static indentation resistance of auxetic carbon fibre laminates.* Physica status solidi (b), 2011. **248**(1): p. 66-72.
81. Evans, K.E. and A. Alderson, *Auxetic materials: functional materials and structures from lateral thinking!* Advanced materials, 2000. **12**(9): p. 617-628.
82. Evans, K.E. and K. Alderson, *Auxetic materials: the positive side of being negative.* Engineering Science & Education Journal, 2000. **9**(4): p. 148-154.
83. Cho, H., D. Seo, and D.N. Kim, *Mechanics of auxetic materials.* Handbook of mechanics of materials, 2019: p. 733-757.
84. Li, X., W. Peng, W. Wu, J. Xiong, and Y. Lu, *Auxetic mechanical metamaterials: from soft to stiff.* International Journal of Extreme Manufacturing, 2023. **5**(4): p. 042003.
85. Garland, A.P., K.M. Adstedt, Z.J. Casias, B.C. White, W.M. Mook, B. Kaehr, B.H. Jared, B.T. Lester, N.S. Leathe, E. Schwaller, and B.L. Boyce, *Coulombic friction in metamaterials to dissipate mechanical energy.* Extreme Mechanics Letters, 2020. **40**: p. 100847.
86. McCrary, A., M.S. Hashemi, and A. Sheidaei, *Programmable bidirectional mechanical metamaterial with tunable stiffness and frictional energy dissipation.* Advanced Theory and Simulations, 2022. **5**(7): p. 2200135.
87. Lv, W., P. Yu, and D. Li, *An energy dissipation metamaterial based on Coulomb friction and vibration.* International Journal of Mechanical Sciences, 2024. **263**: p. 108764.
88. Li, J., Z. Chen, Q. Li, L. Jin, and Z. Zhao, *Harnessing Friction in Intertwined Structures for High-Capacity Reusable Energy-Absorbing Architected Materials.* Adv Sci (Weinh), 2022. **9**(13): p. e2105769.
89. Fu, K., Z. Zhao, and L. Jin, *Programmable Granular Metamaterials for Reusable Energy Absorption.* Advanced Functional Materials, 2019. **29**(32).
90. Blau, P.J., *Friction Science and Technology: From Concepts to Applications, Second Edition (2nd ed.).* 2008.
91. Paulo Davim, J., *Traditional Machining Processes-Research Advances*. 2015, Springer-Verlag, Berlin-Heidelberg.

92. Hutchings, I.M., *Leonardo da Vinci's studies of friction.* Wear, 2016. **360–361**: p. 51-66.
93. Popova, E. and V.L. Popov, *The research works of Coulomb and Amontons and generalized laws of friction.* Friction, 2015. **3**(2): p. 183-190.
94. Chang, S., X. Guo, and X. Ni, *Optical Metasurfaces: Progress and Applications.* Annual Review of Materials Research, 2018. **48**(1): p. 279-302.
95. Zahra, S., L. Ma, W. Wang, J. Li, D. Chen, Y. Liu, Y. Zhou, N. Li, Y. Huang, and G. Wen, *Electromagnetic metasurfaces and reconfigurable metasurfaces: a review.* Frontiers in Physics, 2021. **8**: p. 593411.
96. Assouar, B., B. Liang, Y. Wu, Y. Li, J.-C. Cheng, and Y. Jing, *Acoustic metasurfaces.* Nature Reviews Materials, 2018. **3**(12): p. 460-472.
97. Babaee, S., S. Pajovic, A. Rafsanjani, Y. Shi, K. Bertoldi, and G. Traverso, *Bioinspired kirigami metasurfaces as assistive shoe grips.* Nature Biomedical Engineering, 2020. **4**(8): p. 778-786.
98. Ramezani, M. and Z. Mohd Ripin, *4D printing in biomedical engineering: Advancements, challenges, and future directions.* Journal of functional biomaterials, 2023. **14**(7): p. 347.
99. Luna Vera, O.S., C.W. Kim, and Y. Oshima, *Energy dissipation and absorption capacity influence on experimental modal parameters of a PC girder.* Journal of Physics: Conference Series, 2017. **842**.
100. Lopez, I.o., J.M. Busturiab, and H. Nijmeijera. *Energy dissipation of a friction damper*. 2004.
101. Meyer, N. and R. Seifried, *Energy dissipation in horizontally driven particle dampers of low acceleration intensities.* Nonlinear Dynamics, 2022. **108**(4): p. 3009-3024.
102. Giuriani, E. and A. Marini, *Wooden Roof Box Structure for the Anti-Seismic Strengthening of Historic Buildings*. International Journal of Architectural Heritage, 2008. **2**(3): p. 226-246.
103. Yenidogan, C., *Earthquake-Resilient Design of Seismically Isolated Buildings: A Review of Technology.* Vibration, 2021. **4**(3): p. 602-647.
104. Crupi, V., E. Kara, G. Epasto, E. Guglielmino, and H. Aykul, *Prediction model for the impact response of glass fibre reinforced aluminium foam sandwiches.* International Journal of Impact Engineering, 2015. **77**: p. 97-107.
105. Jiang, R., Z. Gu, T. Zhang, D. Liu, H. Sun, Z. Pan, and D. Peng, *Energy Absorption Characteristics of a CFRP-Al Hybrid Thin-Walled Circular Tube under Axial Crushing.* Aerospace, 2021. **8**(10): p. 279.
106. Khatkar, V. and B.K. Behera, *Experimental investigation of composite leaf spring reinforced with various fiber architecture.* Advanced Composite Materials, 2020. **29**(2): p. 129-145.
107. Ha, N.S., V.T. Le, and N.S. Goo, *Investigation of punch resistance of the Allomyrira*

dichtoloma beetle forewing. Journal of Bionic Engineering, 2018. **15**(1): p. 57-68.

108. Nayeon, L., H.M. F., R. Hongjoo, N. Ben, L. Jun, and W.L. N, *Hierarchical multiscale structure–property relationships of the red-bellied woodpecker (Melanerpes carolinus) beak.* Journal of The Royal Society Interface, 2014. **11**.
109. Fischer, S., M. Thielen, R.R.L. M.Sc., R. Seidel, C. Fleck, T. Speck, and A. Bührig-Polaczek, *Pummelos as Concept Generators for Biomimetically Inspired Low Weight Structures with Excellent Damping Properties.* Advanced Engineering Materials, 2010. **12**(12): p. B658-B663.
110. Hull, C.W., *The birth of 3D printing.* Research-Technology Management, 2015. **58**(6): p. 25-30.
111. Zhu, S. and X. Zhang, *Metamaterials: artificial materials beyond nature.* National Science Review, 2018. **5**(2): p. 131-131.
112. Wang, Z., C. Luan, G. Liao, J. Liu, X. Yao, and J. Fu, *Progress in Auxetic Mechanical Metamaterials: Structures, Characteristics, Manufacturing Methods, and Applications.* Advanced Engineering Materials, 2020. **22**(10).
113. Cai, W., U.K. Chettiar, A.V. Kildishev, and V.M. Shalaev, *Optical cloaking with metamaterials.* Nature photonics, 2007. **1**(4): p. 224-227.
114. Schurig, D., J.J. Mock, B. Justice, S.A. Cummer, J.B. Pendry, A.F. Starr, and D.R. Smith, *Metamaterial electromagnetic cloak at microwave frequencies.* Science, 2006. **314**(5801): p. 977-980.
115. Xue, R., X. Cui, P. Zhang, K. Liu, Y. Li, W. Wu, and H. Liao, *Mechanical design and energy absorption performances of novel dual scale hybrid plate-lattice mechanical metamaterials.* Extreme Mechanics Letters, 2020. **40**: p. 100918.
116. Hamidreza, Y.S., A.H. Akbarzadeh, A. Mirbolghasemi, and K. Hermenean, *3D printed meta-sandwich structures: Failure mechanism, energy absorption and multi-hit capability.* Materials & Design, 2018. **160**: p. 179-193.
117. Giri, T.R. and R. Mailen, *Controlled snapping sequence and energy absorption in multistable mechanical metamaterial cylinders.* International Journal of Mechanical Sciences, 2021. **204**: p. 106541.
118. Bacigalupo, A., V. Diana, and L. Gambarotta, *Energy absorbing multilayered self-recovering metamaterials with chiral topology.* International Journal of Solids and Structures, 2023. **273**: p. 112213.
119. Mercer, C., T. Speck, J. Lee, D.S. Balint, and M. Thielen, *Effects of geometry and boundary constraint on the stiffness and negative Poisson's ratio behaviour of auxetic metamaterials under quasi-static and impact loading.* International Journal of Impact Engineering, 2022. **169**: p. 104315.
120. Morris, C.B., L. Bekker, C.M. Spadaccini, M.R. Haberman, and C.C. Seepersad, *Tunable Mechanical Metamaterial with Constrained Negative Stiffness for Improved Quasi-Static and Dynamic Energy Dissipation.* Advanced Engineering Materials, 2019. **21**.

121. Ling, S.J., J. Sanny, and W. Moebs, *University Physics*. 2016: OpenStax, Rice University.
122. Gibson, L.J., *Cellular solids.* Mrs Bulletin, 2003. **28**(4): p. 270-274.
123. Budynas, R.G. and A.M. Sadegh, *Roark's Formulas for Stress and Strain, 9E*. 2020: McGraw Hill LLC.
124. Beer, F.P., E.R. Johnston, J.T. DeWolf, and D.F. Mazurek, *Mechanics of Materials*. 2015: McGraw-Hill Education.
125. Hamzehei, R., M. Bodaghi, J.A. Iglesias Martinez, Q. Ji, G. Ulliac, M. Kadic, C. Wang, A. Zolfagharian, and N. Wu, *Parrot beak-inspired metamaterials with friction and interlocking mechanisms 3D/4D printed in micro and macro scales for supreme energy absorption/dissipation.* Advanced Engineering Materials, 2023. **25**(11): p. 2201842.
126. Dykstra, D.M., S. Janbaz, and C. Coulais, *The extreme mechanics of viscoelastic metamaterials.* APL Materials, 2022. **10**(8).
127. Huang, J., Y. Xu, S. Qi, J. Zhou, W. Shi, T. Zhao, and M. Liu, *Ultrahigh energy-dissipation elastomers by precisely tailoring the relaxation of confined polymer fluids.* Nature Communications, 2021. **12**(1): p. 3610.
128. Roland, C.M., *Viscoelastic behavior of rubbery materials*. 2011: OUP Oxford.
129. Saedi, S., E. Acar, H. Raji, S.E. Saghaian, and M. Mirsayar, *Energy damping in shape memory alloys: A review.* Journal of Alloys and Compounds, 2023: p. 170286.
130. Sidharth, R., A. Mohammed, W. Abuzaid, and H. Sehitoglu, *Unraveling frequency effects in shape memory alloys: NiTi and FeMnAlNi.* Shape Memory and Superelasticity, 2021. **7**(2): p. 235-249.
131. Zhang, J., R. Perez, and E. Lavernia, *Dislocation-induced damping in metal matrix composites.* Journal of materials science, 1993. **28**: p. 835-846.
132. Haid, D.M., O. Duncan, J. Hart, and L. Foster, *Characterisation of thermoplastic polyurethane (TPU) for additive manufacturing.* Tagungsband zum, 2022. **14**: p. 85-88.
133. Reyes, S.I., M.F. Vassiliou, and D. Konstantinidis, *Experimental characterization and constitutive modeling of thermoplastic polyurethane under complex uniaxial loading.* Journal of the Mechanics and Physics of Solids, 2024. **186**: p. 105582.
134. Bien-aimé, L.K.M., B.B. Blaise, and T. Beda, *Characterization of hyperelastic deformation behavior of rubber-like materials.* SN Applied Sciences, 2020. **2**(4): p. 648.
135. Stephen, K.M., L. Liwu, L. Yanju, and L. Jinsong, *A review on material models for isotropic hyperelasticity.* International Journal of Mechanical System Dynamics, 2021. **1**(1): p. 71-88.
136. Kim, D.S. and K. Konagai, *Seismic isolation effect of a tunnel covered with coating material.* Tunnelling and Underground Space Technology, 2000. **15**(4): p. 437-443.
137. Nawaz Md, Z., M. S C, and S.K.R. Jyosyula, *Development of low-cost base isolation technique using multi-criteria optimization and its application to masonry building.* Soil Dynamics and Earthquake Engineering, 2023. **172**: p. 108024.
138. Brown, N., M.K. Owen, A. Garland, J.D. DesJardins, and G.M. Fadel, *Design of a Single*

Layer Metamaterial for Pressure Offloading of Transtibial Amputees. J Biomech Eng, 2021. **143**(5).

139. Cagle, J.C., P.G. Reinhall, K.J. Allyn, J. McLean, P. Hinrichs, B.J. Hafner, and J.E. Sanders, *A finite element model to assess transtibial prosthetic sockets with elastomeric liners.* Med Biol Eng Comput, 2018. **56**(7): p. 1227-1240.
140. Karthikeyan, R., S. Rajkumar, R.J. Bensingh, M.A. Kader, and S.K. Nayak, *Finite element analysis of elastomer used in automotive suspension systems.* Journal of Elastomers & Plastics, 2020. **52**(6): p. 521-536.
141. Tobajas, R., E. Ibartz, and L. Gracia, *A comparative study of hyperelastic constitutive models to characterize the behavior of a polymer used in automotive engines.* 2nd International Electronic Conference on Materials, 2016.
142. Reyes, S., M.F. Vassiliou, K. Agathos, and D. Konstantinidis. *Finite element modeling of the rolling behavior of a polyurethane sphere for low-cost seismic isolation application*. in *COMPDYN 2023: 9th International Conference on Computational Methods in Structural Dynamics and Earthquake Engineering. Proceedings Volume I*. 2023. Institute of Structural Analysis and Antiseismic Research School of Civil ….
143. Emminger, C., U.D. Çakmak, R. Preuer, I. Graz, and Z. Major, *Hyperelastic material parameter determination and numerical study of TPU and PDMS dampers.* Materials, 2021. **14**(24): p. 7639.
144. Wang, Y., W. Luo, J. Huang, C. Peng, H. Wang, C. Yuan, G. Chen, B. Zeng, and L. Dai, *Simplification of hyperelastic constitutive model and finite element analysis of thermoplastic polyurethane elastomers.* Macromolecular Theory and Simulations, 2020. **29**(4): p. 2000009.
145. Yu, L.-M. and H.-X. Huang, *Temperature and shear dependence of rheological behavior for thermoplastic polyurethane nanocomposites with carbon nanofillers.* Polymer, 2022. **247**: p. 124791.
146. Jeong, E., E. Calius, and M. Ramezani, *Design and Analysis of a 3D Frictional Mechanical Metamaterial for Efficient Energy Dissipation.* Advanced Materials Technologies, 2024. **n/a**(n/a): p. 2400614.
147. Treloar, L.R.G., *The elasticity of a network of long-chain molecules—II.* Transactions of the Faraday Society, 1943. **39**: p. 241-246.
148. Mooney, M., *A Theory of Large Elastic Deformation.* Journal of Applied Physics, 1940. **11**(9): p. 582-592.
149. Ogden, R.W., *Non-linear elastic deformations*. 1997: Courier Corporation.
150. Yeoh, O.H., *Some Forms of the Strain Energy Function for Rubber.* Rubber Chemistry and Technology, 1993. **66**: p. 754-771.
151. Gent, A.N., *A new constitutive relation for rubber.* Rubber chemistry and technology, 1996. **69**(1): p. 59-61.
152. Qi, H.J. and M.C. Boyce, *Stress–strain behavior of thermoplastic polyurethanes.*

Mechanics of materials, 2005. **37**(8): p. 817-839.

153. Diani, J., B. Fayolle, and P. Gilormini, *A review on the Mullins effect.* European Polymer Journal, 2009. **45**(3): p. 601-612.
154. Ma, C., T. Ji, C.G. Robertson, R. Rajeshbabu, J. Zhu, and Y. Dong, *Molecular insight into the Mullins effect: irreversible disentanglement of polymer chains revealed by molecular dynamics simulations.* Physical Chemistry Chemical Physics, 2017. **19**(29): p. 19468-19477.
155. Baniasadi, M., E. Yarali, M. Bodaghi, A. Zolfagharian, and M. Baghani, *Constitutive modeling of multi-stimuli-responsive shape memory polymers with multi-functional capabilities.* International Journal of Mechanical Sciences, 2021. **192**: p. 106082.
156. Yousefi, A., S. Jolaiy, M. Lalegani Dezaki, A. Zolfagharian, A. Serjouei, and M. Bodaghi, *3D-Printed soft and hard meta-structures with supreme energy absorption and dissipation capacities in cyclic loading conditions.* Advanced Engineering Materials, 2023. **25**(4): p. 2201189.
157. Chen, Y.-L. and L. Ma, *Synchronous enhancement of extreme-damping and stiffness in elastic mechanical metamaterials via self-tensioning friction mechanism.* International Journal of Solids and Structures, 2025. **313**: p. 113282.
158. Rubinstein, S., G. Cohen, and J. Fineberg, *Visualizing stick–slip: experimental observations of processes governing the nucleation of frictional sliding.* Journal of Physics D: Applied Physics, 2009. **42**(21): p. 214016.
159. Spikes, H., *Stress-augmented thermal activation: Tribology feels the force.* Friction, 2018. **6**: p. 1-31.
160. Blanchette, M.G. and C.M. Powers, *The influence of footwear tread groove parameters on available friction.* Applied ergonomics, 2015. **50**: p. 237-241.
161. Li, K.W. and C.J. Chen, *The effect of shoe soling tread groove width on the coefficient of friction with different sole materials, floors, and contaminants.* Applied ergonomics, 2004. **35**(6): p. 499-507.
162. Li, K.W., H.H. Wu, and Y.-C. Lin, *The effect of shoe sole tread groove depth on the friction coefficient with different tread groove widths, floors and contaminants.* Applied ergonomics, 2006. **37**(6): p. 743-748.
163. Wallaschek, J. and B. Wies, *Tyre tread-block friction: modelling, simulation and experimental validation.* Vehicle system dynamics, 2013. **51**(7): p. 1017-1026.
164. Löwer, J., P. Wagner, H.-J. Unrau, B. Wies, and F. Gauterin, *Model for the pattern-dependent wet grip prediction of tires.* Vehicles, 2021. **3**(1): p. 84-110.
165. Liu, Y., H. Chen, S. Wu, J. Gao, Y. Li, Z. An, B. Mao, R. Tu, and T. Li, *Impact of vehicle type, tyre feature and driving behaviour on tyre wear under real-world driving conditions.* Science of the Total Environment, 2022. **842**: p. 156950.
166. Moore, D.F., *Friction and wear in rubbers and tyres.* Wear, 1980. **61**(2): p. 273-282.
167. Wu, J., L. Chen, D. Chen, Y. Wang, B. Su, and Z. Cui, *Experiment and simulation research*

on the fatigue wear of aircraft tire tread rubber. Polymers, 2021. **13**(7): p. 1143.

168. Ilie, F. and A.-C. Cristescu, *Tribological behavior of friction materials of a disk-brake pad braking system affected by structural changes—A review.* Materials, 2022. **15**(14): p. 4745.
169. Yu, L., B. Ma, C. Zheng, M. Chen, Q. Wang, and B. Zhang, *Study on the groove area effects on the friction-wear properties of a Cu-based wet clutch.* Tribology International, 2021. **163**: p. 107096.
170. Sha, Z., X. Li, C. Song, L. Shi, J. Yin, Y. Liu, and S. Zhang, *Research on the influence of floating brake pad structure on the friction interface performance of disc brake.* Tribology Transactions, 2024(just-accepted): p. 1-25.
171. Cross, R., *Effects of friction between the ball and strings in tennis.* Sports engineering, 2000. **3**(2): p. 85-97.
172. Rekilä, K.-P. and A. Klein-Paste, *Measuring bicycle braking friction in winter conditions.* Cold regions science and technology, 2016. **125**: p. 108-116.
173. Caldwell, A.W., *Development and Comparison of 3D Dynamic Models of Golf Clubhead-Ball Impacts*. 2023, University of Waterloo.
174. Shi, G., X. Yu, H. Meng, F. Zhao, J. Wang, J. Jiao, and H. Jiang, *Effect of surface modification on friction characteristics of sliding bearings: A review.* Tribology international, 2023. **177**: p. 107937.
175. Grabovic, E., A. Artoni, M. Gabiccini, M. Guiggiani, L. Mattei, F. Di Puccio, and E. Ciulli, *Friction-induced efficiency losses and wear evolution in hypoid gears.* Machines, 2022. **10**(9): p. 748.
176. Bortnowski, P., W. Kawalec, R. Król, and M. Ozdoba, *Types and causes of damage to the conveyor belt–Review, classification and mutual relations.* Engineering Failure Analysis, 2022. **140**: p. 106520.
177. Aymard, A., E. Delplanque, D. Dalmas, and J. Scheibert, *Designing metainterfaces with specified friction laws.* Science, 2024. **383**(6679): p. 200-204.
178. Slesarenko, V. and L. Pastewka, *The bumpy road to friction control.* Science, 2024. **383**(6679): p. 150-151.
179. Liefferink, R.W., B. Weber, C. Coulais, and D. Bonn, *Geometric control of sliding friction.* Extreme Mechanics Letters, 2021. **49**: p. 101475.
180. Okereke, M. and S. Keates, *Finite element applications.* Cham: Springer International Publishing AG, Springer, 2018.
181. Chagnon, G., J. Ohayon, J.-L. Martiel, and D. Favier, *Hyperelasticity modeling for incompressible passive biological tissues*, in *Biomechanics of living organs*. 2017, Elsevier. p. 3-30.

APPENDICES

Appendix A. Material properties of CPE HG100

The average values of Young's modulus and Poisson's ratio were obtained from five compression experiments, resulting in values of 284.4 MPa and 0.3, respectively (see Fig. S1). The mass and volume of the cylindrical specimen were measured at 4.89 g and 6.2832 cm^3, respectively. By dividing the mass by the volume, the sample's density was calculated, yielding a value of 0.7783 g/cm^3.

From the coefficient of friction (CoF) measurements in Section 3.4.1, the experimental results showed an average CoF of 0.547 for the contact pair. Table S1 outlines the properties used in the theoretical model as well as in the finite element (FE) simulations.

Table S1. Summary of measured properties for CPE HG100.

Young's modulus (MPa)	Poisson's ratio	Density (g/mm^3)	CoF
284.4	0.3	0.7783	0.547

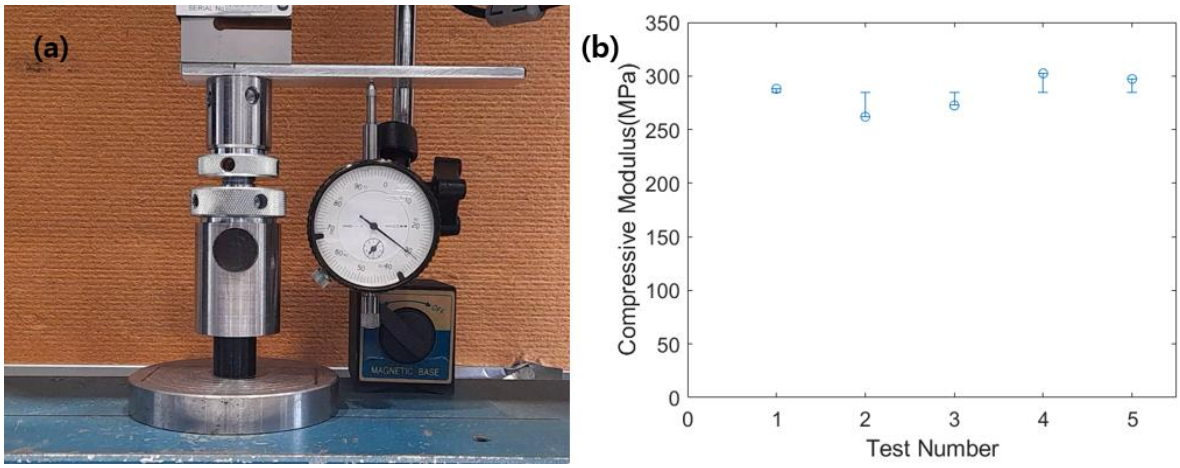

Figure S1. (a) Compression test setup with a cylindrical specimen. (b) Scatter plots with error bars derived from the experimental results.

Appendix B. Mesh convergence study with contact surface resolutions

In ANSYS, resolution values range from 1 to 7, with higher values indicating finer mesh quality. While finer meshes provide greater accuracy, they also significantly increase the computational time required for mesh generation and solving the requested simulation.

In this study, a 1mm displacement was applied to the unit cell with a constant CoF value. We systematically adjusted the mesh level from 0 to 5 to assess mesh sensitivity and observe the resulting changes in peak force and hysteresis (see Fig. S2). We found that without contact sizing, both peak force and hysteresis were noticeably lower. However, as the resolution value increased, the peak force stabilised at around 212.85N at a resolution level of 3 (see Table S2), while the hysteresis area continued to increase, albeit to a lesser extent (see Fig. S2b).

Taking into account both accuracy and computational efficiency, we selected a resolution level of 4. At this setting, the total number of elements in the unit model was 14,712, with the central hexagonal part containing 1,560 elements. The pinwheel and four column sections, which experience direct friction, had 6,065 and 7,087 elements, respectively. This configuration utilised a finer mesh in the contact areas, improving the accuracy of friction dissipation analysis.

Table S2. Variation in peak force from finite element simulations at different contact sizing resolution values.

Contact sizing resolution	Peak force (N)
0 (no contact sizing)	204.11
1	211.13
2	212.32
3	212.85
4	212.56
5	212.26

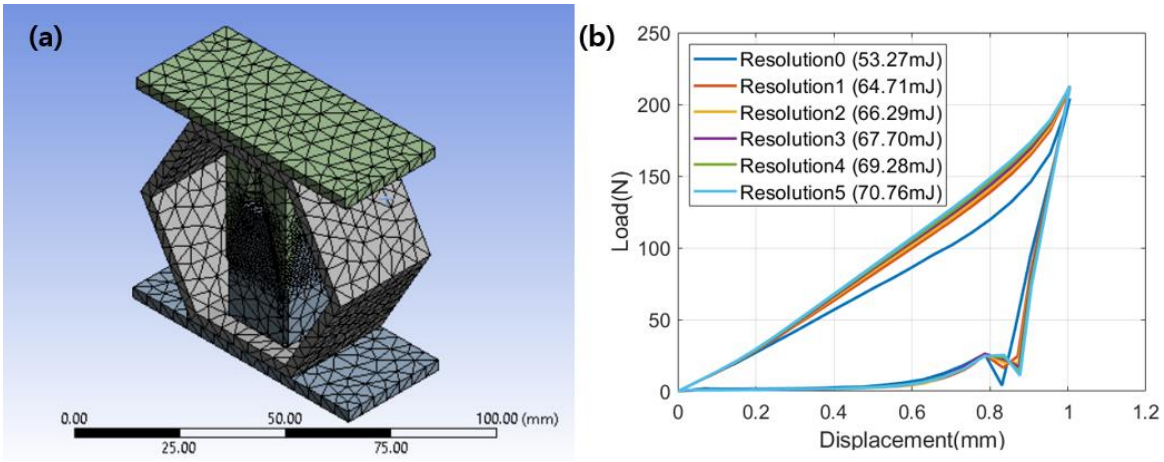

Figure S2. (a) Mesh generation on the CAD model. (b) Plots formed from each of the different resolution settings.

Appendix C. Force-displacement curves from quasi-static compression tests using CPE HG100 unit cell specimens and numerical results

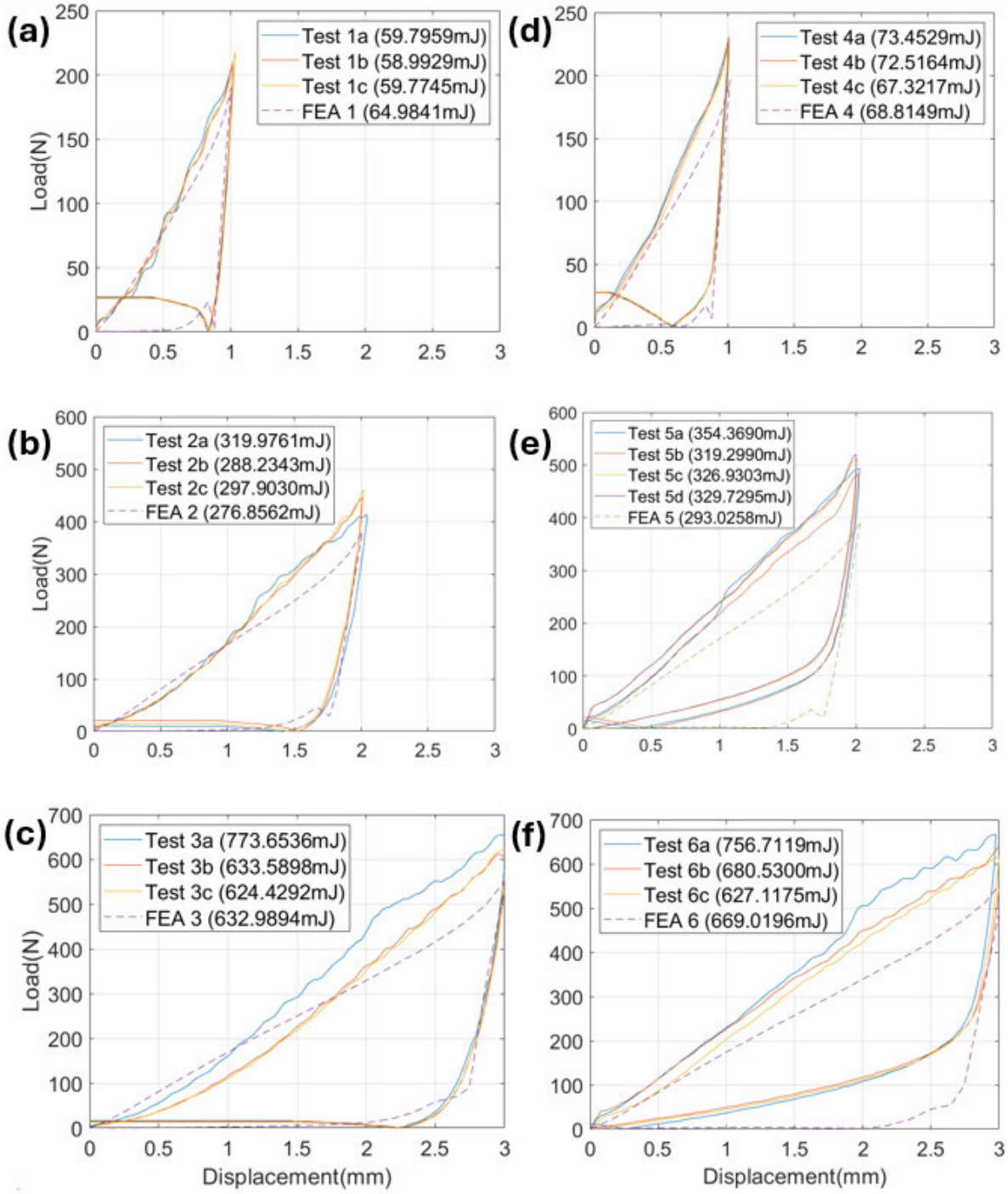

Figure S3. Conventional hexagon model's force-displacement plots obtained from experiments and FE simulations, under (a) 1mm displacement, (b) 2mm displacement, and (c) 3mm displacement. Force-displacement plots from the re-entrant hexagon model under (d) 1mm displacement, (e) 2mm displacement, and (f) 3mm displacement.

Table S3. Summary of numerical results from compression tests with the conventional hexagon model and the re-entrant hexagon model, including measures of energy dissipation (ED), energy accumulation (EA), and peak force (PF).

Displacement (mm)	Conventional hexagon			Re-entrant hexagon		
	ED (mJ)	EA (mJ)	PF (N)	ED (mJ)	EA (mJ)	PF (N)
1	59.80	90.15	205.52	73.45	102.02	226.67
1	58.99	90.43	210.00	72.52	101.07	230.83
1	59.77	92.70	217.81	67.32	94.98	223.33
2	319.98	392.20	413.93	354.37	484.44	493.00
2	288.23	373.17	445.83	319.30	444.78	484.00
2	297.90	382.16	461.67	326.93	486.52	511.90
2	-	-	-	329.73	487.51	520.00
3	773.65	921.94	657.53	756.71	1044.70	667.21
3	633.59	769.85	612.33	680.53	1007.40	652.00
3	624.43	758.64	620.83	627.12	930.53	618.33

Appendix D. Applying periodic boundary conditions (PBCs) in FE simulations using a representative volume element (RVE)

In order to implement periodic boundary conditions in ANSYS Workbench, the constraint equation functions are used. There are various periodic boundary condition types within finite element modelling. The first of them, one of the commonest boundary condition types, is the Dirichlet boundary condition such as displacement and temperature these are values that can be applied directly onto the nodes and then they will displace at a constant at a defined value. Next one is the Neuman boundary condition which is things like pressure the forces across the domain. The third is a mid-mode boundary condition which is basically a combination of the Dirichlet and the Neuman. The final type is the periodic boundary condition.

The definition of the PBC stipulates that under a specific loading history, opposite pairs of edges or surfaces on the boundary of an RVE should deform identically [180]. This principle implies the two phases must have a uniform or repetitive deformation pattern. In other words, every node on the system a corresponding node on the other face must have a corresponding equivalent deformation. To implement the PBC within FEA solvers, periodic mesh is used to ensure that all the nodes on one surface of the pair have matching with the corresponding nodes on the opposite surface.

A canonical equation, which is an equation of a variable displacement that must always be equal to zero, is useful for setting constraint equations in ANSYS. This mathematical form refers to the correlation between internal edge nodes that are positioned opposite to each other.

The mathematics Canonical equation for PBCs can be illustrated like:

$$P_{(x,y)}^{N_a} - P_{(x,y)}^{N_b} = 0 \tag{S1}$$

on boundary Ω_k.

P is the model parameter which can be displacement, temperature, and velocity on the face. N_a and N_b are nodes that are kinematically linked on opposite positions so the displacement on one face in the x and y axis must equal to the displacement on another face parallel connected. k indicates a direction of the upper, lower, left, and right of base boundaries. Equation S1 states that the displacement of node a must be equal to displacement of node b as a fundamental principle. Figure S4 illustrates the simplified PBCs imposed on the unit cell.

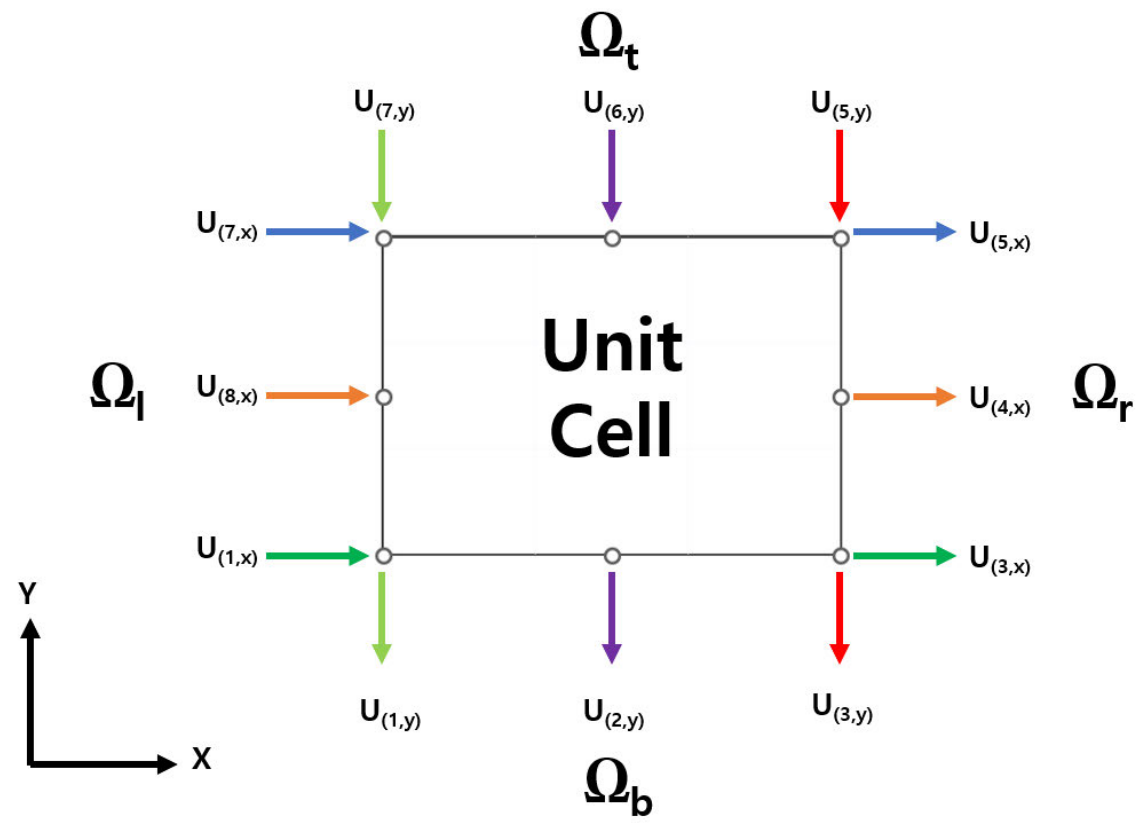

Figure S4. A simplified representation of the PBCs imposed on the boundary of a unit cell using canonical equations.

To employ PBC in RVE cells configured based on conventional hexagonal and re-entrant structures, respectively, we select as remote points the outer top and bottom faces of the central frame and the outer vertical faces of the two horizontal half-walls protruding from the sides of the base hexagon (see Figure S5).

Face 1, which represents the top face of each RVE cell, and face 2, which corresponds to the bottom face, are paired together to reflect the fact that displacement boundary conditions of the same magnitude are applied, but in opposite directions. Face 3 and face 4, which are both vertical faces of the beam extending outward from the midpoint of each oblique side, form another pair with constraint equations applied to reflect that the deformation is applied at the same height along the y-axis. The constraint equations used in ANSYS Workbench are listed in Table S4. The subtraction or addition sign of each equation is assigned to distinguish whether the deformation of the paired faces in the x, y, and z directions occurs in the same or opposite direction.

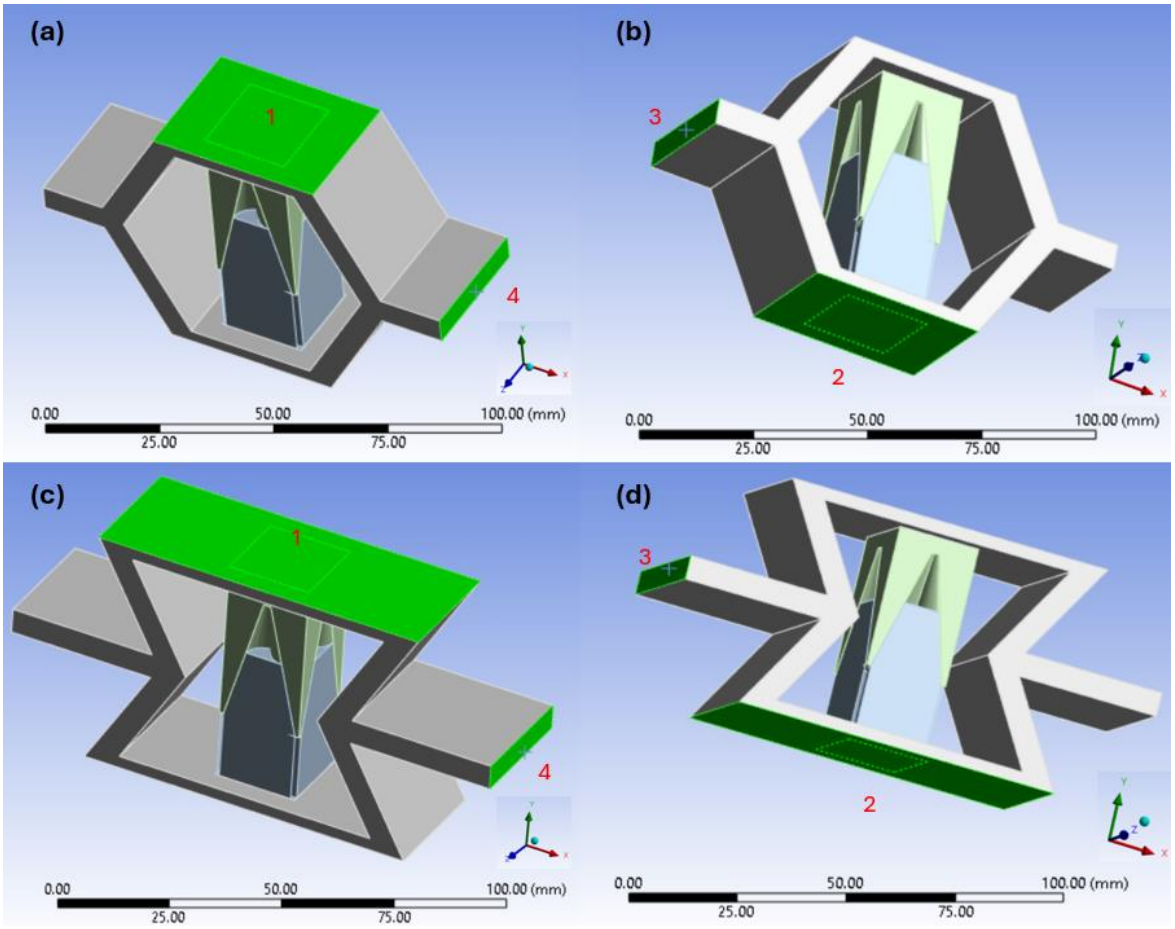

Figure S5. The general perspective of RVE within a hexagonal (a-b) and a re-entrant (c-d) framework featuring sliding internal elements. Two vertical faces on the half-walls and the top and bottom faces on the outer hexagonal frame were chosen as remote points for PBC setup. In order to facilitate the efficient setup of the constraint equations, numbers are assigned to the faces in order to differentiate between them.

Table S4. Every pair of all constraint equations utilised in the PBC setup.

Face 1 and 2 pair	Face 3 and 4 pair
$d_{1x} - d_{2x} = 0$	$d_{3x} + d_{4x} = 0$
$d_{1y} + d_{2y} = 0$	$d_{3y} - d_{4y} = 0$
$d_{1z} - d_{2z} = 0$	$d_{3z} - d_{4z} = 0$

Appendix E. Stress distribution on the 13-unit cells geometry

Equivalent stress distribution on a three-layer geometry consisting of 13-unit cells is investigated through FE simulation. The simulation result shows that the equivalent stress distribution of the cells located at the sides of the middle layer was smaller than the stress distribution of the cells located at the top or bottom layer (Figure S6). This is because the cell geometry of 13-unit cells is assumed to be in the centre of a structure made up of a myriad of honeycombs, with negative y-axis displacements on the top faces and positive y-axis displacements on the bottom faces, and periodic boundary conditions to ensure that the same displacements occur on the outer faces at the same height.

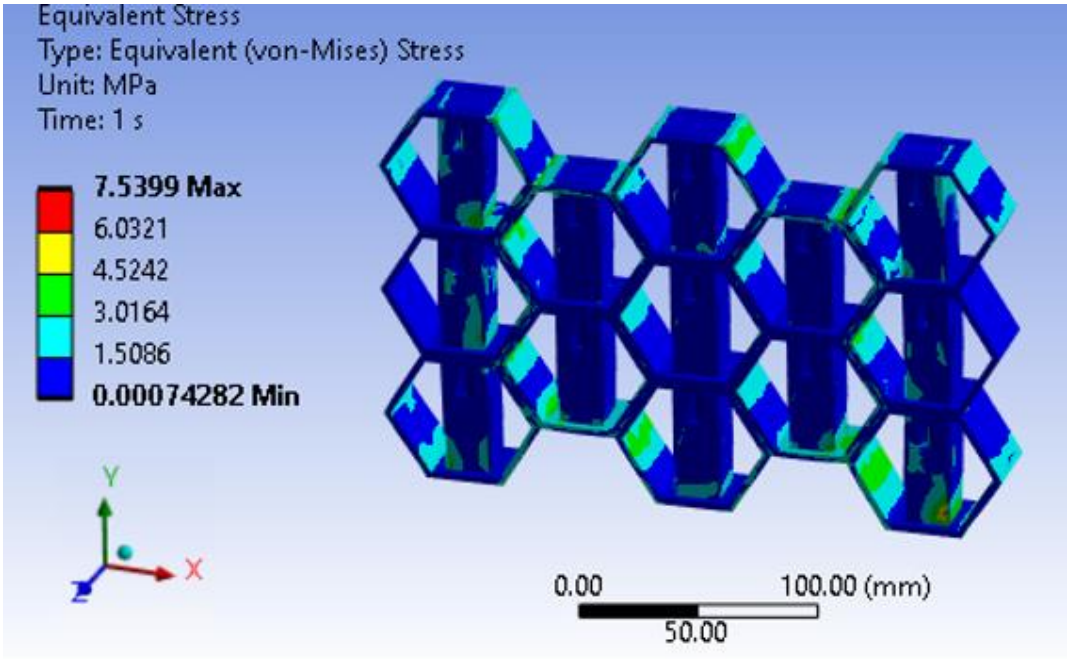

Figure S6. Equivalent (von Mises) stress distribution on the 13-unit cells geometry at the end of the loading step in FE simulation. The top faces are subjected to a displacement of 1.5 mm in the downward direction and the three bottom faces are set to a displacement of 1.5 mm in the upward direction.

Appendix F. Compression tests with cylindrical samples made of TPU 95A

Cylindrical shapes with a 10 mm radius and 20 mm height specimens were prepared to generate data for visualising hyperelastic behaviour of the constituent material – TPU 95A. Compression tests were carried out under different strain value, 40%, 50%, and 60% to observe one of the key characteristics of hyperelastic materials – the inflection point. The results show that the inflection point occurs at approximately 40% strain which demonstrates that 50% or higher strains sufficiently capture this defining feature of hyperelastic materials. Figure S7 exhibits the loading curve corresponding to each applied strain.

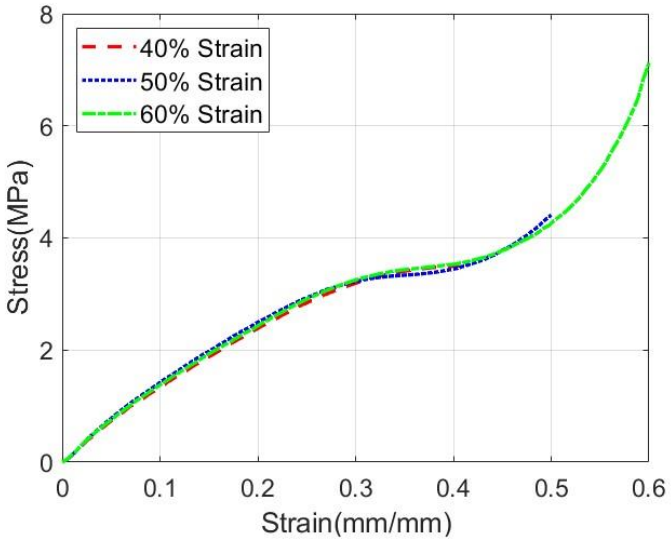

Figure S7. Loading curves under 40 %, 50 %, and 60 % strain boundary conditions from compression tests with cylindrical shape specimens.

The proposed unit cell prototype in this study is approximately 64 mm in height and was subjected to compression tests under displacements of 1 mm, 2 mm, and 3 mm. In order to correspond to the same strain values for cylindrical specimens, additional compression tests were performed by applying strains of 1.56 %, 3.12 % and 4.67 %. The disparity between the paths of the loading and unloading curves creates a hysteresis loop, which was used to measure the internal energy dissipation at each strain (Figure S8). From here, we can also calculate the energy loss fraction, expressed as the energy dissipated divided by the energy absorbed, for each strain, which was measured to be 25.5515 %, 25.9813 %, and 27.7544 % for strains of 1.56 %, 3.12 %, and 4.67 %, respectively. Here, it is explicitly seen that the energy loss fraction increases with increasing strain.

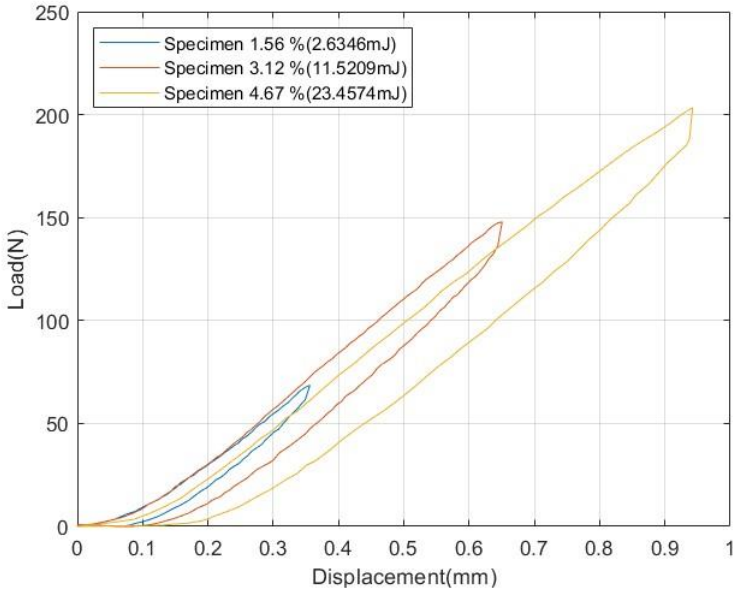

Figure S8. Load-displacement curves under 1.56 %, 3.12 %, 4.67 % strain boundary conditions and corresponding energy dissipation quantities from the compression test with cylindrical shape specimens. The legend includes the hysteresis loop area values corresponding to each strain.

Appendix G. Curve fitting via various hyperelastic constitute models

To select the hyperelastic model that provides the closest fit to the actual experimental data, we applied all the options available in ANSYS, eliminating those models that caused simulation errors due to convergence to certain values of the uniaxial, biaxial, and/or shear curves formed by curve fitting. The Yeoh 3rd order, Mooney-Rivlin 3 parameter, Gent, and Ogden 3rd order models were selected as suitable candidates, and when the curve fitting results were compared, the Mooney-Rivlin 3 parameter model was the closest to the experimental data (Figure S9).

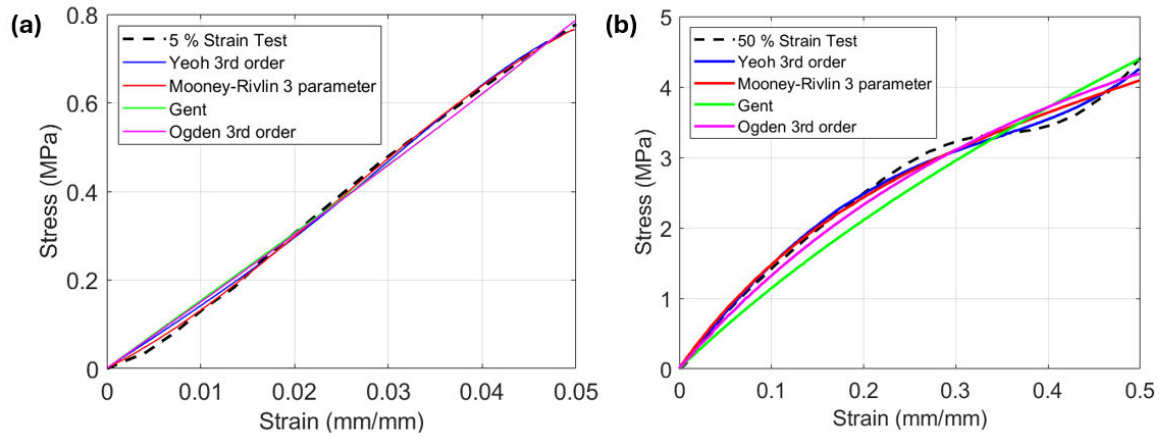

Figure S9. Curve fitting results via Yeoh 3rd order, Mooney-Rivlin 3 parameter, Gent, and Ogden 3rd order models for hyperelastic materials, compared with the (a) 5% strain compression test result and (b) 50% strain compression test result.

In addition, each of constitutive models has two methods for handling and optimising curve fitting: normalised error, and absolute error. Figure S10 illustrates both curve fitting results by using Mooney-Rivlin 3 parameter model, revealing that the absolute error method provides a more synchronised fit to the experimental data.

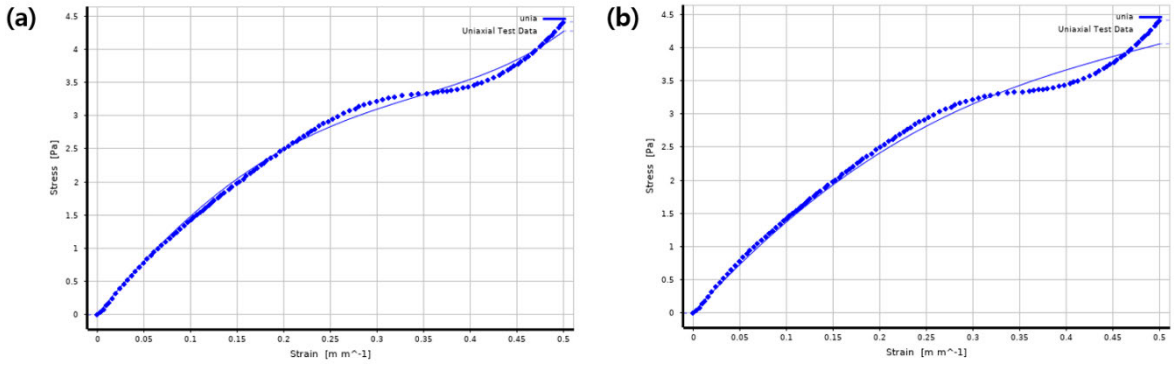

Figure S10. Curve fitting results through (a) absolute error and (b) normalised error in the Mooney-Rivlin 3 parameter model.

Appendix H. Force-Displacement curves of the quasi-static compression tests using TPU 95A unit cell specimens

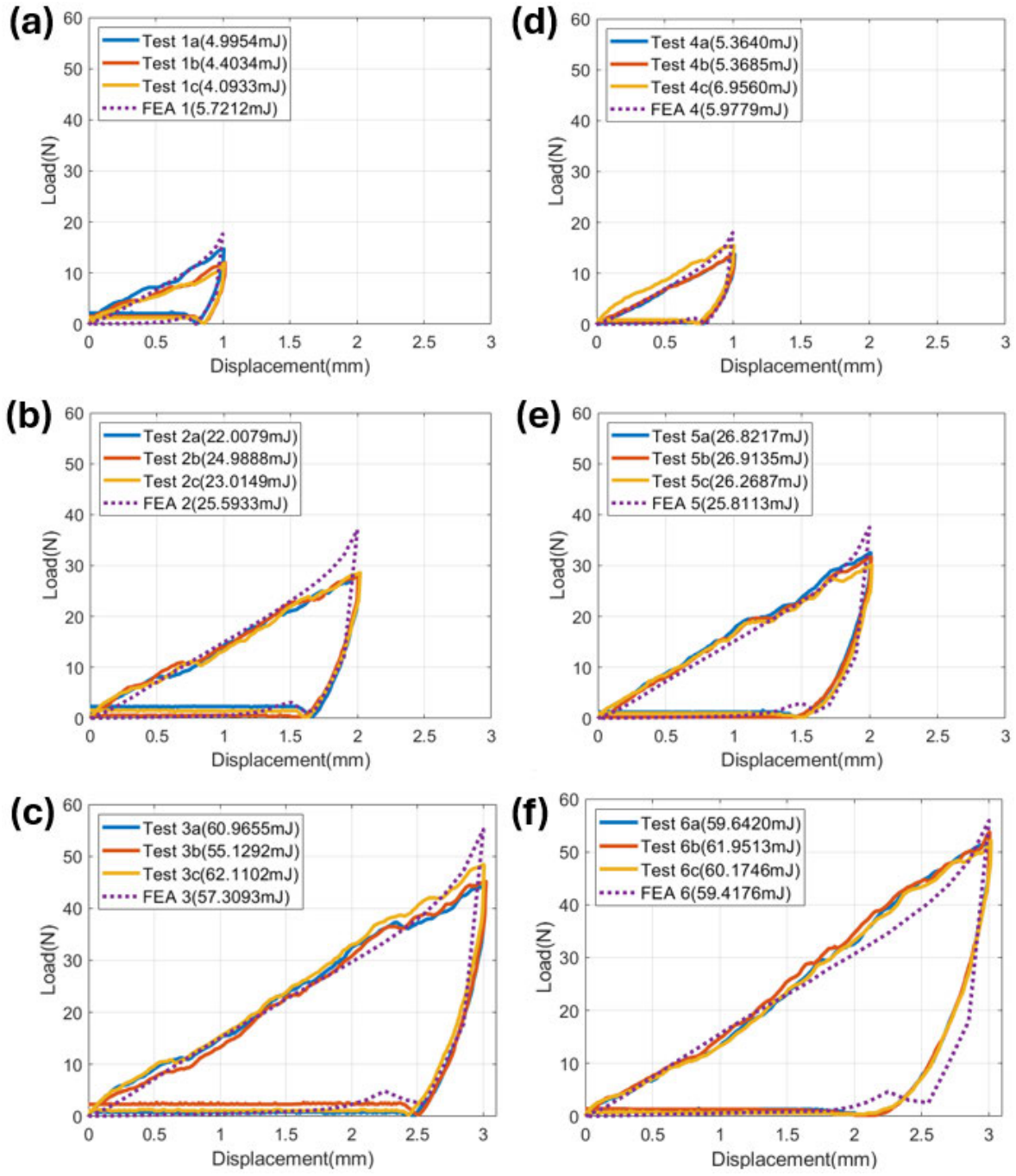

Figure S11. (a) Conventional hexagon model's force-displacement plots under 1mm displacement and a plot generated from FE simulation. (b) 2mm displacement. (c) 3mm displacement. Force-displacement plots from the re-entrant hexagon model under (d) 1mm displacement, (e) 2mm displacement, and (f) 3mm displacement.

Appendix I. Results of compression experiment to measure varied Young's modulus using TPU 95A cylindrical specimens

Due to the slack mechanism at the initial process when we are measuring a displacement from the crosshead of a universal testing machine (UTM), there is a gentle curve at the beginning of the loading of the compression experiments, but for a more accurate Young's modulus measurement, we disregarded this part and measured the slope of the rest of the loading curves in Figure S12. Except for the initial part, the rest of each curve was divided into five parts and the slope was measured for each part in Table S5, which reflects the variable Young's modulus with strain, which is a major feature of hyperelastic materials. There was a total of three compression experiments for each displacement, with average Young's modulus values of 14.3043 MPa, 16.5626MPa, and 16.2922 MPa for displacements of 1 mm, 2 mm, and 3 mm, respectively. These values were substituted in the theoretical model to obtain the energy dissipation for each displacement.

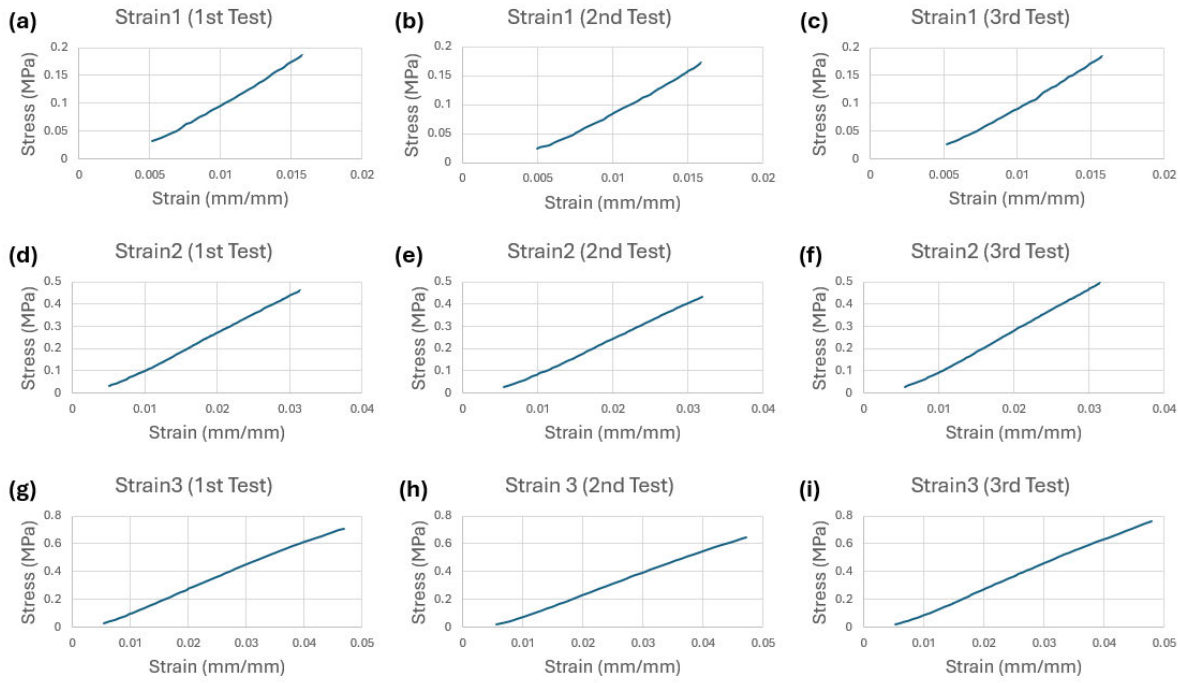

Figure S12. Plots of compression experimental results with cylindrical specimens subjected to various maximum strains of: (a, b, c) 1.56 %, (d, e, f) 3.12 %, (g, h, i) 4.67 %. The experiments were repeated three times for each maximum strain.

Table S5. Measured Young's Modulus from the compression tests by using the cylindrical specimens under 1mm, 2mm, and 3mm displacements. The initial gentle part of each stress-strain curve was removed, then the remaining part was divided into five equal parts to find the slope of each part, which was then averaged to find the Young's modulus of TPU 95A with a variable Young's modulus per strain.

Strain (mm/mm)	1st region E (MPa)	2nd region E (MPa)	3rd region E (MPa)	4th region E (MPa)	5th region E (MPa)	Average E (MPa)
0.0156	11.4019	14.8443	14.2055	15.4895	16.5995	14.50814
0.0156	9.6468	12.8685	13.9942	14.7917	16.0166	13.46356
0.0156	11.4563	14.7369	14.6411	17.6392	16.2327	14.94124
0.0312	13.7508	16.9766	17.3159	16.5534	16.8688	16.2891
0.0312	12.7310	15.7882	16.4672	16.6369	15.2802	15.3807
0.0312	14.4300	18.8439	19.5231	18.6741	18.6192	18.01806
0.0467	16.0113	18.0083	17.6444	16.5109	13.9371	16.4224
0.0467	13.2446	16.2791	16.1841	15.3620	14.0838	15.03072
0.0467	15.4147	19.0586	18.7384	17.7305	16.1758	17.4236

Appendix J. Derivation of the Mooney-Rivlin 3 parameter model for calculating strain energy density of hyperelastic materials

In order to formulate the hyperelastic behaviour of the constituent material, Mooney-Rivlin 3 parameter was adapted to its strain energy density can be expressed like Equation S2.

$$W_{hyper} = C_{10}(\bar{I}_1 - 3) + C_{01}(\bar{I}_2 - 3) + C_{11}(\bar{I}_1 - 3)(\bar{I}_2 - 3) + \frac{1}{d}(J-1)^2 \quad \text{(S2)}$$

where $\bar{I}_1$ and $\bar{I}_2$ are the first and second deviatoric invariant respectively, which are a measure of the deformation of the material. J is the volume ratio after and before deformation. In the case of an incompressible material, the J value is equal to 1.

C_{10}, C_{01}, and C_{11} are material constants that characterise the material's response to deformation and d is material incompressibility parameters. To carry out curve fitting, uniaxial compression test data was transferred into ANSYS.

For an incompressible material, the determinant of the deformation gradient tensor F is unity:

$$\det(F) = 1 \quad \text{(S3)}$$

This condition leads to the relation between the principal stretches $\lambda_1,\ \lambda_2,\ \lambda_3$.

$$\lambda_1 * \lambda_2 * \lambda_3 = 1 \quad \text{(S4)}$$

Under uniaxial compression along a pure single axis, such as x-axis, we have

$$\lambda_1 = \lambda \quad \text{(S5)}$$

$$\lambda_2 = \lambda_3 = \lambda_t \quad \text{(S6)}$$

Due to incompressibility:

$$\lambda * \lambda_t^2 = 1 \quad \text{(S7)}$$

$$\lambda_t = \sqrt{\frac{1}{\lambda}} \quad \text{(S8)}$$

The right Cauchy-Green deformation tensor C is

$$C = F^T F = \begin{pmatrix} \lambda^2 & 0 & 0 \\ 0 & \lambda_t^2 & 0 \\ 0 & 0 & \lambda_t^2 \end{pmatrix} = \begin{pmatrix} \lambda^2 & 0 & 0 \\ 0 & \frac{1}{\lambda} & 0 \\ 0 & 0 & \frac{1}{\lambda} \end{pmatrix} \tag{S9}$$

The invariants $\bar{I}_1$ and $\bar{I}_2$ can be calculated by below Equation S9 and Equation S10 [181].

$$\bar{I}_1 = tr(C) = \lambda^2 + 2 * \lambda_t^2 = \lambda^2 + \frac{2}{\lambda} \tag{S10}$$

$$\bar{I}_2 = \frac{1}{2}[(tr(C))^2 - tr(C^2)] \tag{S11}$$

where tr is the trace operator.

Calculate $tr(C^2)$

$$C^2 = \begin{pmatrix} \lambda^2 & 0 & 0 \\ 0 & \frac{1}{\lambda} & 0 \\ 0 & 0 & \frac{1}{\lambda} \end{pmatrix} * \begin{pmatrix} \lambda^2 & 0 & 0 \\ 0 & \frac{1}{\lambda} & 0 \\ 0 & 0 & \frac{1}{\lambda} \end{pmatrix} = \begin{pmatrix} \lambda^4 & 0 & 0 \\ 0 & \frac{1}{\lambda^2} & 0 \\ 0 & 0 & \frac{1}{\lambda^2} \end{pmatrix} \tag{S12}$$

$$tr(C^2) = \lambda^4 + \frac{2}{\lambda^2} \tag{S13}$$

Substitute Equation S8 and S11 to complete $\bar{I}_2$

$$\bar{I}_2 = \frac{1}{2}\left[(\lambda^2 + \frac{2}{\lambda})^2 - (\lambda^4 + \frac{2}{\lambda^2})\right] = 2\lambda + \frac{1}{\lambda^2} \tag{S14}$$

Therefore, the strain energy per unit volume W_{hyper} is

$$\begin{aligned} W_{hyper} = {} & C_{10}\left(\lambda^2 + \frac{2}{\lambda} - 3\right) + C_{01}\left(2\lambda + \frac{1}{\lambda^2} - 3\right) \\ & + C_{11}\left(\lambda^2 + \frac{2}{\lambda} - 3\right)\left(2\lambda + \frac{1}{\lambda^2} - 3\right) + \frac{1}{d}(J-1)^3 \end{aligned} \tag{S15}$$

Appendix K. Angle optimisation

To set the angles for the simple preliminary study with a base model, a pair of trapezoidal hexahedra, 30, 45 and 60 degrees extruded cutting angles were set from 30×30×60mm cuboid block. Figure S13 illustrates each of the trapezoid hexahedra prepared using the selected tilted angles.

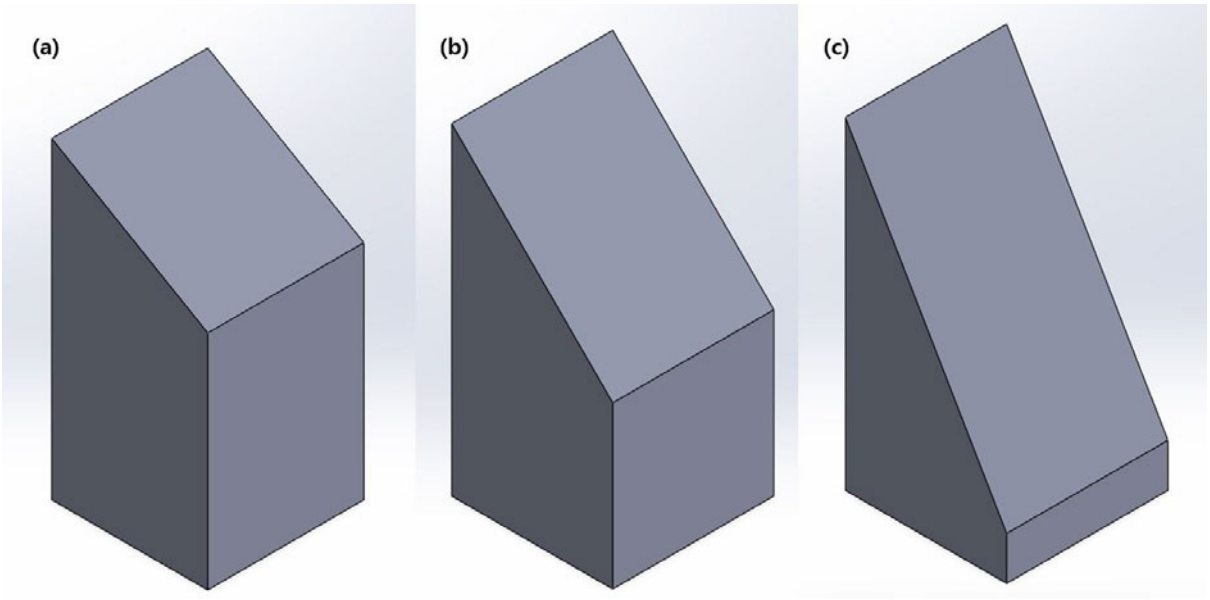

Figure S13. The various angles attempted to be applied between a pair of contacting sliding surfaces. (a) 30-degree, (b) 45-degree and (c) 60-degree.

The results of FE simulations with each of these pairs of trapezoids are shown in Figure S14. The outcomes are quite interesting: the peak force values at the end of the loading step are dominated by the smaller truncation angle values. The 30-degree angle design shows peak force values that are about three times higher than the 45-degree angle design and about five times higher than the 60-degree angle design as shown in Figure S14, which is attributed to the strong stress concentration at the bottom end edge of the contact surface. However, the small cutting incident value is a disadvantage for achieving high energy dissipation, and in fact the 30-degree angle design shows the narrowest hysteresis region results. The 60-degree design had somewhat higher energy dissipation than the 30-degree design, but not as much as the 45-degree design, which led to the final selection of the 45-degree design.

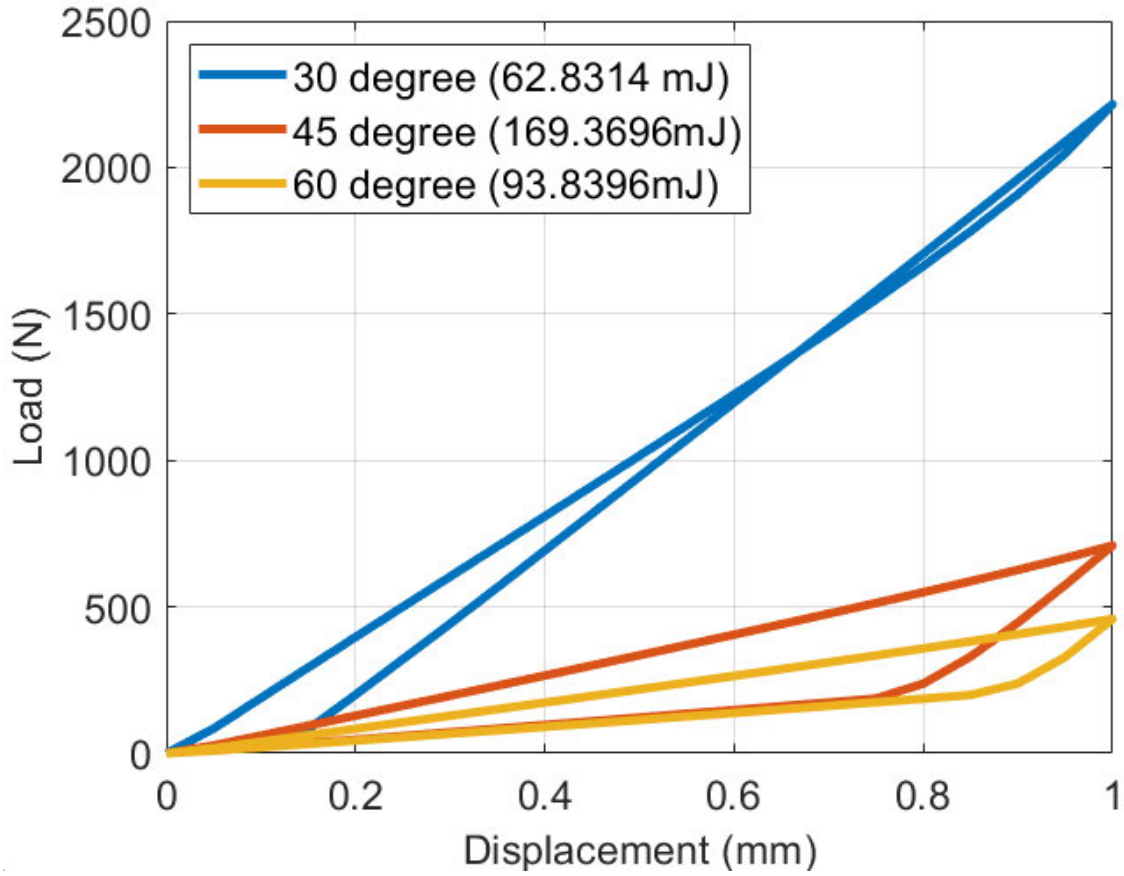

Figure S14. Comparing load-displacement curves FE simulation for simple designs which hold 30-, 45- and 60-degree contact angles.

Appendix L. Parametric study for optimising angle between contact surfaces to mitigate stress concentration on the below edge area

During the previous development of the friction metamaterial, the internal structures with the faces corresponding to the top and bottom tilted contact surfaces were set to be at an angle of 45 degrees to the ground surface, resulting in the two contact surfaces being parallel to each other.

This design approach resulted in stresses being concentrated at the lower edge of the contact surfaces throughout the compression range of up to 3 mm, which was set as the target displacement in Chapters 4 and 5. A method was devised to modify the angle of the lower contact surfaces to achieve stress distribution across the contact surfaces. For this purpose, the incidence angles of the two beams corresponding to the lower part were adjusted to 40, 42, 44, and 46 degrees as illustrated in Figure S15. In addition, the width of the beams was reduced by about half to investigate the stress distribution behaviour. In contrast, the triangular head column corresponding to the upper part was still set at an angle of 45 degrees. The two parts were assembled in a central re-entrant structure to form a unit cell.

The 46-degree model was deemed inappropriate because it promoted contact between the lower edges of the contact surfaces, and simulation results confirmed that the 44-degree model was also insufficient to avoid stress concentration in that region. In the case of the 40-degree model, the lower sides of the contact surfaces were already separated by an excessive distance before the start of loading, which resulted in stress distribution in the upper region of the contact surfaces throughout the loading step.

The 42-degree model, on the other hand, exhibited that stresses were predominantly distributed in the upper region of the contact surface at the beginning of the simulation loading, and as the applied displacement increased, the stress distribution region appeared across the contact surface. The frictional stress distribution region when the applied displacement reaches 1.45 mm, which is approximately half of the maximum displacement, is shown in Figure 6.16 in Chapter 6, which is in line with the ideal stress development we expected. If the displacement is further raised from here, the region of stress concentration shifts to the lower parts of the contact surfaces. This suggests that the 42-degree model is an alternative to eliminate the stress concentration in a specific area at a prescribed displacement, which can minimise part replacement as well as alleviate contact surface wear. It can also be noticed that the angle between the contact surfaces can be considered as a dominant parameter that affects the behaviour of frictional sliding, allowing the stress distribution to be controlled by appropriate adjustments depending on the intended applied displacement.

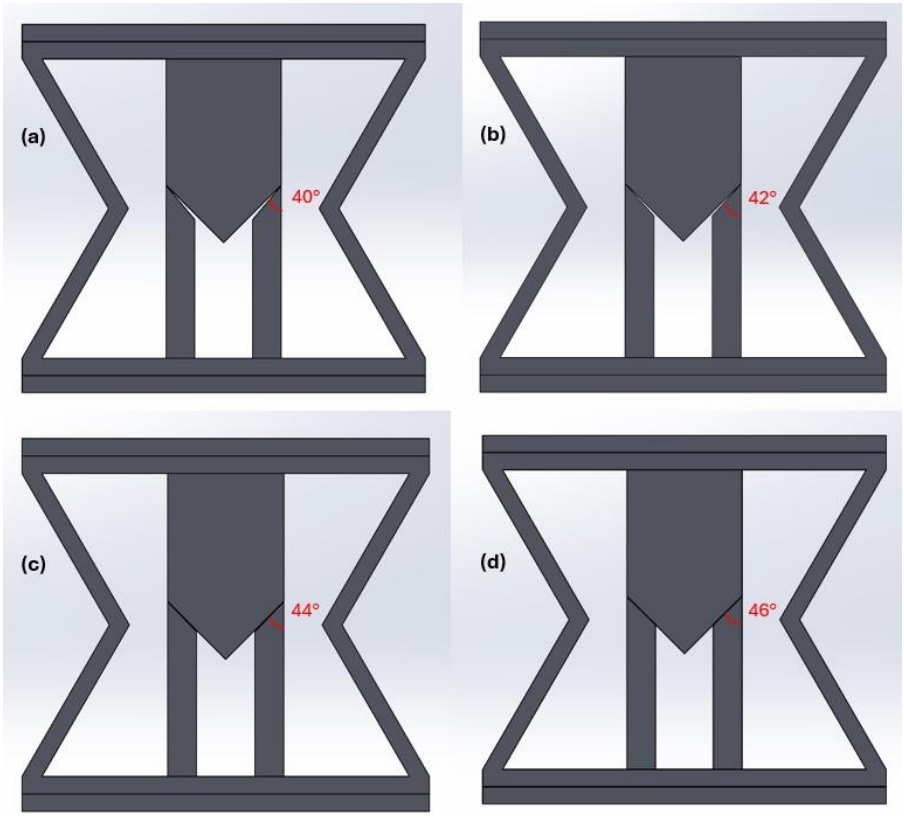

Figure S15. Front view of CAD models describing each unit cell with different incidence angles at the lower part: (a) 40-degree. (b) 42-degree. (c) 44-degree and (d) 46-degree.

Appendix M. Simple modelling with triangle, rectangle, half ellipse, and half circle patterns

Before applying 2D metasurfaces to 3D metamaterial unit cells, the need arose for simple fundamental simulations to compare the performance of potential candidate pattern designs. For this purpose, a pair of trapezoidal hexahedra was adopted as the base model, which can be achieved by extruded cutting triangular parts from the cuboidal model, each with a 45-degree inclination. This 45-degree slope was determined by angle optimisation through FE simulation (see Appendix K). By comparing the simulation results of the basic model that has flat contact surfaces and the model with metasurfaces, a rationale for the application of metasurfaces is established. Subsequently, to comprehensively investigate the effect of various contact geometries on energy dissipation, three different types of metasurfaces – a triangle, a rectangle, and a half ellipse shape – are architected with a constraint to maintain the same contact area (Figure S16). In this case, the contact surface area, which can be considered as the main variable, is removed, making it much easier to focus on the influence of the metasurface pattern.

To fulfil the design condition that the same contact surface area for each model, for the top CAD model part, if an isosceles triangle pattern is applied to the contact surface, the remaining two sides are designed to be 3 mm each, except for one side, which is removed by concave cutting, so that the sum of the concave parts is a total perimeter of 6 mm. In the same way, if a square pattern is applied, it is modelled so that the sum of the lengths of the three sides, except for the one side that was removed, was 6 mm. The semi-elliptical pattern has an arc circumference of 6 mm to match the same contact surface area.

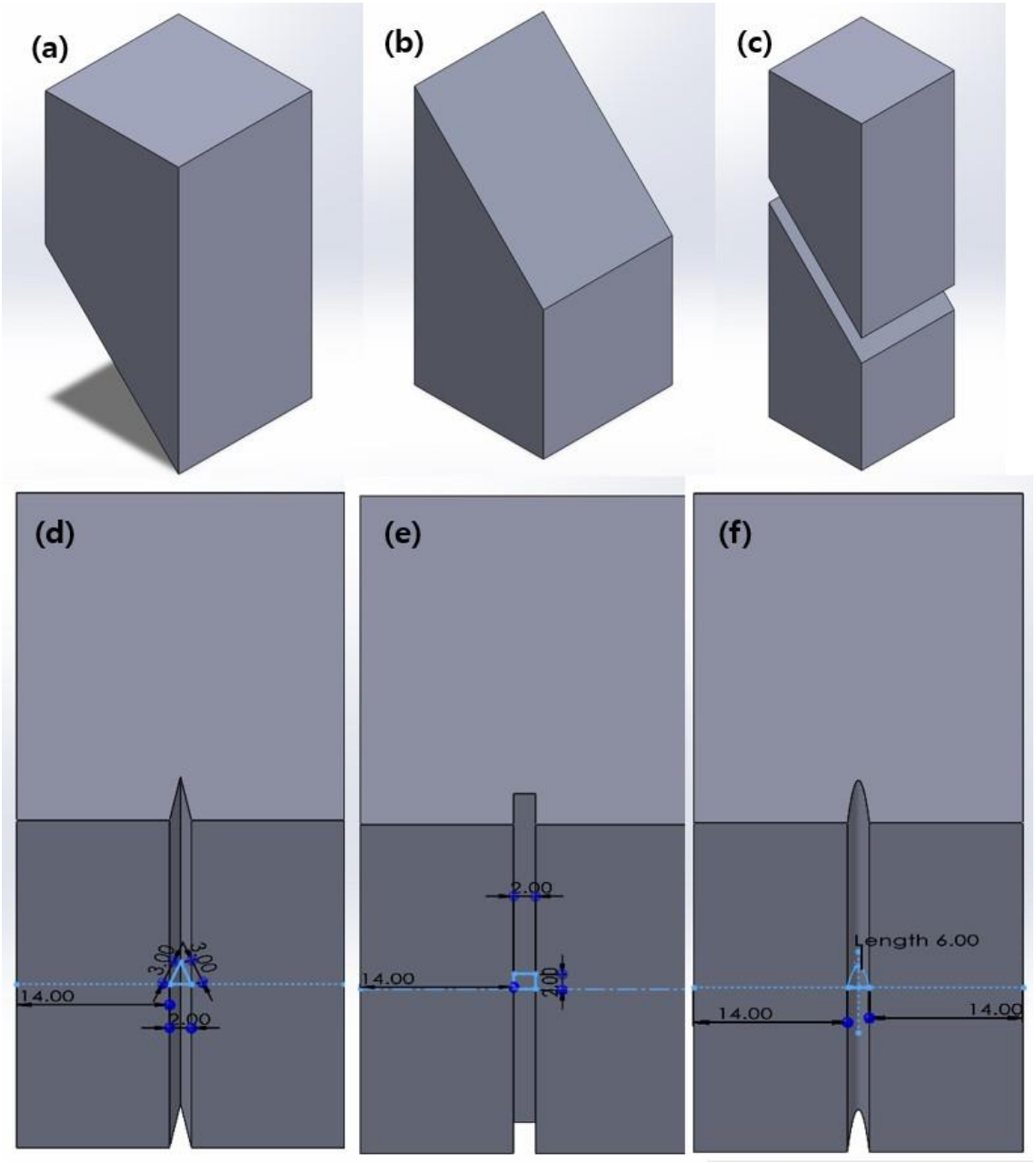

Figure S16. Base model without metasurfaces on the contact area: (a) top part, (b) bottom part, and (c) assembled model. Various patterns – (d) isosceles triangle, (e) rectangle, and (f) half-ellipse are suggested to investigate the performance of metasurfaces.

Following the previous surface designs, a design using a semicircle was also created. Two different types of designs were devised, the first with the same bottom base length (2 mm) as the previous three surfaces (Figure S17a), and the second with a wider diameter to ensure the same contact area. When we consider just one contact part, the length of the contact surface can be 34 mm (Figure S17b). Therefore, if we achieve the same contact area with a half circle pattern, the diameter should be approximately 7.008 mm, as shown in Equation S16.

$$34 = (30 - x) + \frac{\pi}{2}x \tag{S16}$$

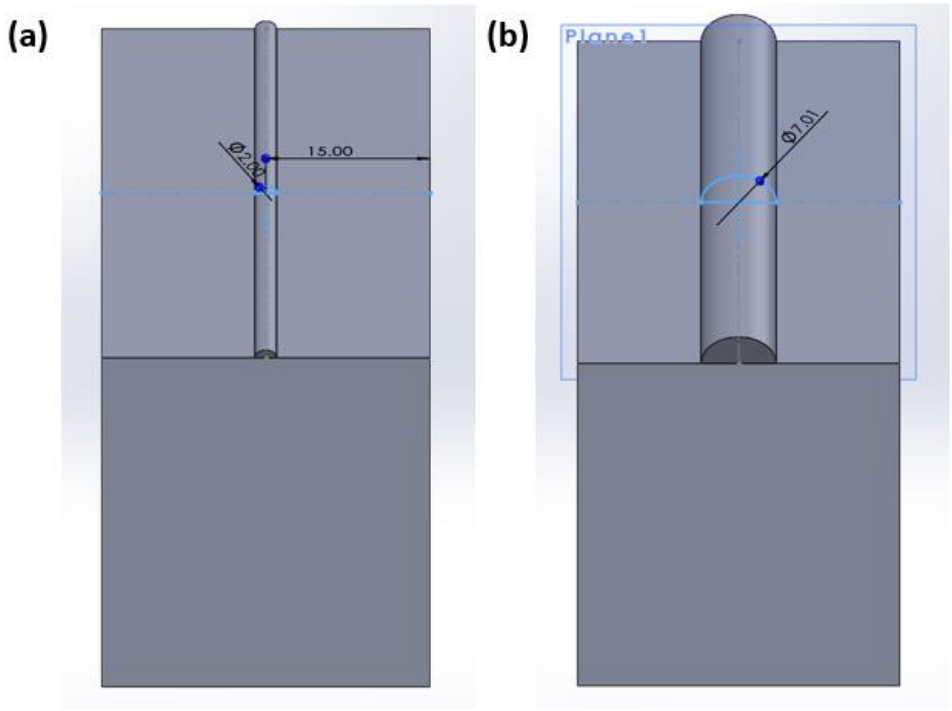

Figure S17. A semi-circular pattern model. (a) Same base length and (b) same contact area to the other patterns in Figures S16(d-f).

Rectangular surface unevenness designs of the same area but different widths were also considered: two designs were proposed, one narrower and deeper (Figure S18a), the other wider and shallower (Figure S18b).

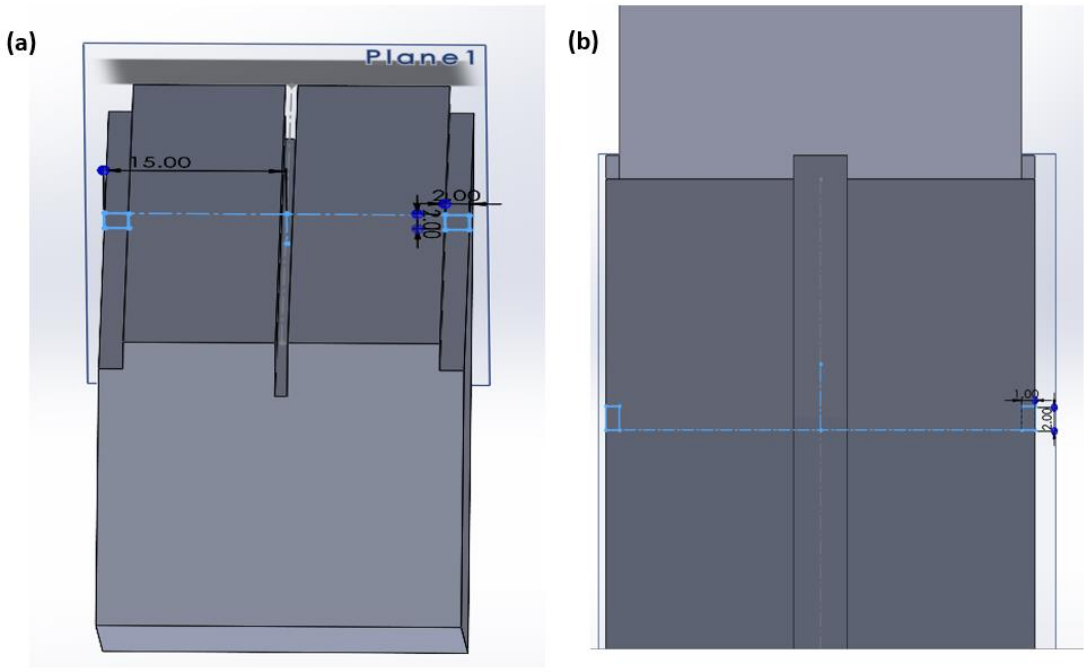

Figure S18. Simple rectangular models: (a) narrower and deeper (b) wider and shallower model.

From the FE simulation using single pattern CAD models as mentioned above, the semi-elliptical pattern model possesses the highest energy dissipation as well as peak force, like Figure S19. For the model with a flat contact surface, the energy dissipation was measured to be the lowest, around 116 mJ, with slight variations in energy dissipation depending on the shape of the pair of convex-concave patterns added to the contact surface.

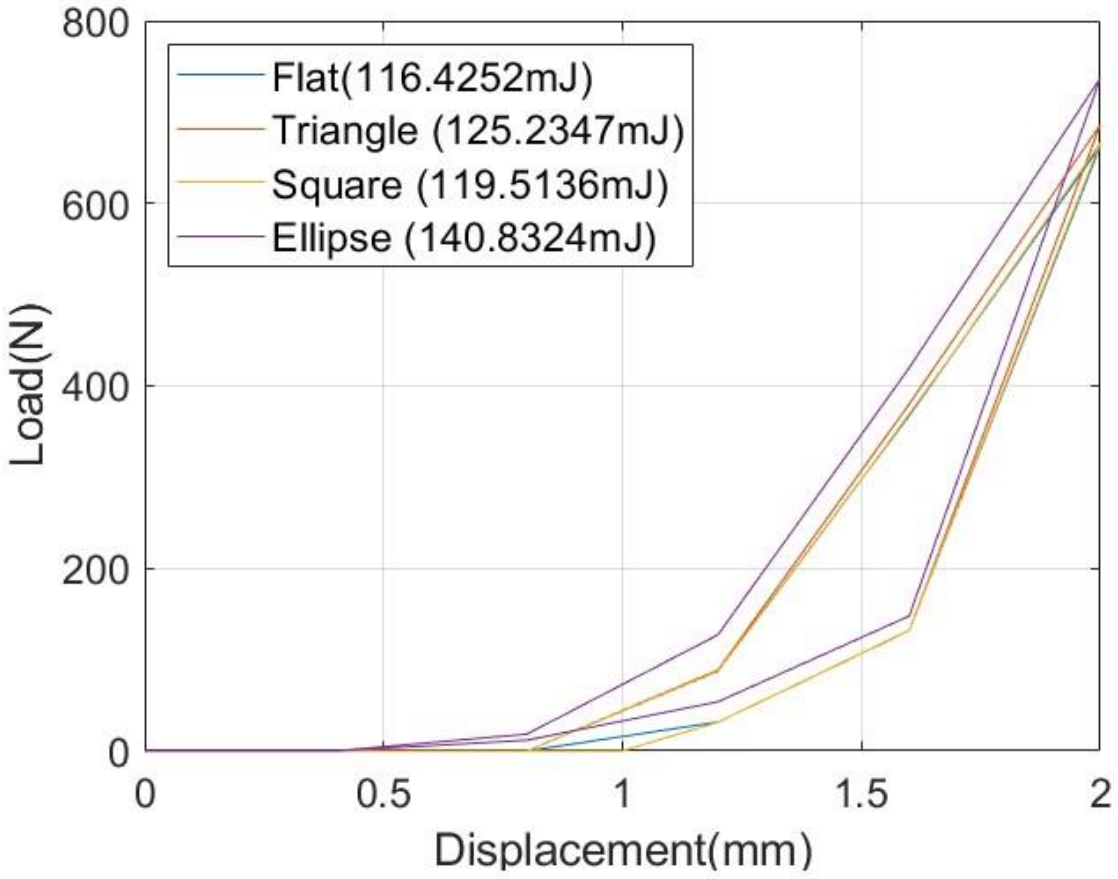

Figure S19. FE simulation results of flat, triangle, square, and half-ellipse models which introduced in Figures S16(a-f).

In the case of semi-circular models in Figure S17, 2 mm diameter model displays 121.07 mJ as energy dissipation and 670.46 N peak force while 7.008 mm diameter model exhibits energy dissipation value of 124.3047 mJ and 681.95 N peak force as listed in Table S6. These results demonstrate that the semicircular design model has higher energy dissipation compared to flat surfaces or models with triangular irregularities and is comparable to the energy dissipation performance of square surfaces, but has relatively low dissipation compared to elliptical models. In terms of maximised energy dissipation, these performances are lower than that of half-elliptical pattern. Likewise, both wide and narrow rectangular models in Figure S18 possess inferior energy dissipation performance as listed in Table S7.

Table S6. Energy dissipation quantities of both types of semi-circular pattern models from Figures S17a and S17b.

	Energy dissipation (mJ)	Peak Force (N)
2 mm Diameter model	121.07	670.46
7.008 mm Diameter model	124.3047	681.95

Table S7. Energy dissipation quantities of both types of rectangle pattern models from Figures S18a and S18b.

	Energy dissipation (mJ)	Peak Force (N)
Narrow rectangle model	119.6896	675.5
Wide rectangle model	120.3498	666.6

Appendix N. Global mesh convergence study

We examined the mesh sensitivity around the contact interfaces by using various contact surface resolution settings in our previous work in Appendix B. For the study reported in this manuscript, global mesh convergence was evaluated by varying the Element Size (ES) parameter in ANSYS for the case where a 7 mm displacement was applied to the re-entrant RVE cell and the peak force and energy dissipation results are summarised in Table S8 and Figure S20 below. In the first column of Table S8, element size factor 1 means the default size used in previous work in Appendix B and a factor value of 0.5 means that the element size is set to half the default value for the entire model mesh. This element size factor was systematically adjusted from 1 down to 0.5 in 0.25 intervals.

As the element size was reduced, the hysteresis area slightly increased by 1 - 2 % at each step and the peak force increased by 1 – 2.5%. These results indicate that doubling the number of elements produced a change of less than 4%, and the default element size was judged to provide an acceptable balance between accuracy and computational cost.

Table S8. Variation in peak force, energy dissipation and number of elements from finite element simulations with different Element Size (ES) factor values.

Elements Size (ES) factor	Peak force (N)	Energy dissipation (mJ)	Number of elements
0.5	188.12	595.85	20289
0.75	183.65	583.20	17031
1	181.27	575.53	15357

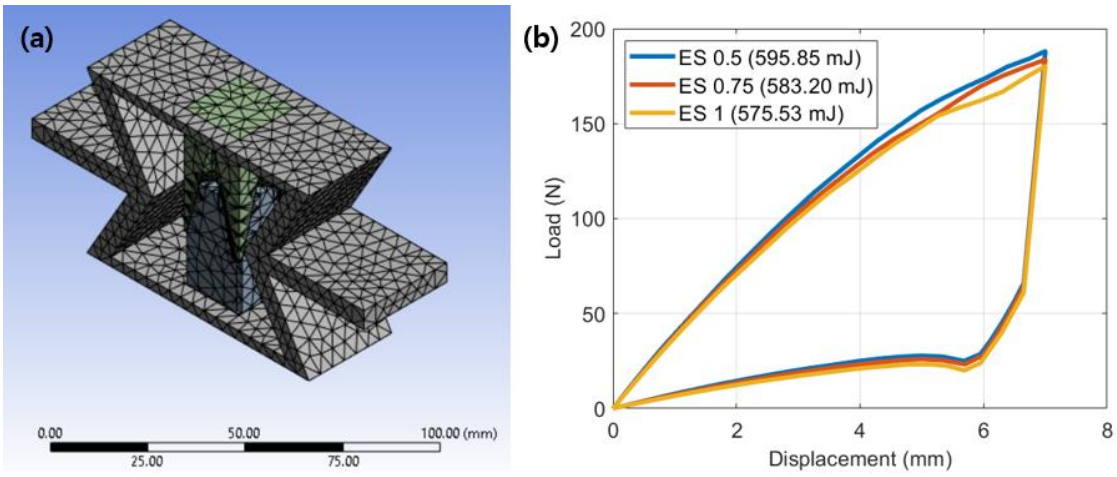

Figure S20. (a) Mesh generation on the CAD model. (b) Plots formed from each of the different elements size settings.